DOKUZ EYLÜL UNIVERSITY

GRADUATE SCHOOL OF NATURAL AND APPLIED SCIENCES

DEVELOPMENT OF SILICA BASED PHOTONIC CRYSTALS DOPED BY RARE-EARTH ELEMENTS

by

Ramazan DALMIŞ

September, 2020

İZMİR

DEVELOPMENT OF SILICA BASED PHOTONIC CRYSTALS DOPED BY RARE-EARTH ELEMENTS

A Thesis Submitted to the
Graduate School of Natural and Applied Sciences of Dokuz Eylül University
In Partial Fulfillment of the Requirements for the Degree of Doctor of Philosophy in Metallurgical and Materials Engineering

Ramazan DALMIŞ

September, 2020
İZMİR

Ph.D. THESIS EXAMINATION RESULT FORM

We have read the thesis entitled **"DEVELOPMENT OF SILICA BASED PHOTONIC CRYSTALS DOPED BY RARE-EARTH ELEMENTS"** completed by **RAMAZAN DALMIŞ** under supervision of **ASSIST. PROF. DR. IŞIL BİRLİK** and we certify that in our opinion it is fully adequate, in scope and in quality, as a thesis for the degree of Doctor of Philosophy.

Assist. Prof. Dr. Işıl BİRLİK

Supervisor

Prof. Dr. Kadriye ERTEKİN

Thesis Committee Member

Assoc. Prof. Dr. N. Funda AK AZEM

Thesis Committee Member

Assoc. Prof. Dr. Osman ÇULHA

Examining Committee Member

Assoc. Prof. Dr. Emre YALAMAÇ

Examining Committee Member

Prof. Dr. Özgür ÖZÇELİK

Director

Graduate School of Natural and Applied Sciences

ACKNOWLEDGMENT

Firstly, I would like to express my deepest gratitude to my advisor, Assist. Prof. Dr. Işıl BİRLİK, for her supervision, guidance, support, understanding and encouragement during my thesis. I would like to express my special appreciation to Prof. Dr. Erdal ÇELİK for his invaluable advice, guidance and support. I also wish to thank to my thesis committee members Prof. Dr. Kadriye ERTEKİN and Assoc. Prof. Dr. Necmiye Funda AK AZEM for her fruitful discussions, reviewing my work and offering valuable suggestions.

I would like to thank Assoc. Prof. Dr. Aylin ZİYLAN, Assoc. Prof. Dr. Mustafa EROL, Assoc. Prof. Dr. Yasemin SEKİ, Dr. Kadir Cihan TEKİN, Dr. Oylum ÇOLPANKAN GÜNEŞ, Serhan KÖKTAŞ, Ozan YILMAZ, Özgür Yasin KESKİN, Tülay KOÇ DELİCE and Recep ERYILMAZ for their invaluable support and kind friendship.

I would like to appreciate Dr. Haydar KAHRAMAN for his encouragement, help and the moments that we shared together.

Finally, a special thank goes to my wife Elif DALMIŞ for her incredible patience, selfless love and support during this thesis. I am grateful for her invaluable love and understanding for all my life. And also I would like to express my special thanks to my family; to my brother İsmail DALMIŞ, my mother Zehra DALMIŞ and my father Ferhat DALMIŞ for providing me with inspiration and constant encouragement during all my life.

Ramazan DALMIŞ

DEVELOPMENT OF SILICA BASED PHOTONIC CRYSTALS DOPED BY RARE-EARTH ELEMENTS

ABSTRACT

Photonic crystal technology has become very popular today with its increasing application areas. Photonic crystal materials, which consist of regular units arranged in nanoscale, can give highly advanced properties to the structure. The aim of this thesis is to develop silica based photonic crystal structures doped by rare-earth elements.

Firstly, the production of polymethylmethacrylate (PMMA) based opal photonic crystals with the three-dimensional regular array was carried out. These structures, which also exhibit photonic crystal properties itself, also serve as templates for inverse opal photonic crystal production. For opal photonic crystal structure, PMMA colloids were produced from methyl methacrylate. Produced colloids were arranged by the fast-sedimentation deposition method. The effects of the production conditions and deposition media on the PMMA based opal photonic crystal coatings were investigated.

PMMA opal photonic crystal template produced under the determined optimum conditions was used to produce silica-based inverse opal photonic crystal coatings. The sol-gel infiltration method was applied in order to produce silica based inverse opal photonic crystal structures. Rare earth elements such as Cerium (Ce), Europium (Eu), Samarium (Sm) and Terbium (Tb) were doped into silica-based inverse opal photonic crystal structures. The effect of doping types in the range of 0.5%-2% (in mole) on inverse opal photonic crystal structures was investigated.

As a result of these studies, structural colored three dimensional opal and inverse opal photonic crystal coatings were produced successfully. Structural colors of the opal photonic crystal coatings can be controlled by the PMMA colloid size change, while

structural colors of silica inverse opal photonic crystal coatings can be controlled by rare earth element doping.

Keywords: Opal photonic crystal, inverse opal photonic crystal, rare-earth element dopant, structural color, silica

SİLİKA ESASLI NADİR TOPRAK ELEMENTLERİ KATKILI FOTONİK KRİSTALLERİN GELİŞTİRİLMESİ

ÖZ

Fotonik kristal teknolojisi, gittikçe artan kullanım alanları ile günümüzde oldukça popüler bir hale gelmiştir. Nano boyutlarda düzenli dizilmiş birimlerden oluşan fotonik kristal malzemeler, yapıya oldukça yüksek gelişmiş özellikler kazandırabilmektedir. Bu tezin amacı silika esaslı, nadir toprak elementi katkılı fotonik kristallerin geliştirilmesidir.

Öncelikle, polimetilmetakrilat (PMMA) esaslı, üç boyutlu düzenli dizilime sahip opal fotonik kristallerin üretimi üzerine çalışmalar yapıldı. Kendileri de fotonik kristal özellik sergileyen bu yapılar ayrıca ters opal fotonik kristal üretimi için şablon görevi gördü. Opal fotonik kristal yapı için, metilmetakrilattan PMMA kolloidleri üretildi. Üretilen kolloidler hızlı sedimentasyon biriktirme yöntemi kullanılarak düzenli dizilim sağlandı. PMMA üretim şartları ve biriktirme ortamları değiştirilerek elde edilen opal fotonik kristal kaplamalar üzerine etkileri incelendi.

Belirlenen optimum şartlarda üretilen PMMA opal fotonik kristal yapısı, silika esaslı ters opal fotonik kristal kaplamaların üretilmesi için kullanıldı. Ters opal yapının üretilmesinde sol-jel infiltrasyon yöntemi kullanıldı. Silika esaslı ters opal fotonik kristal yapılara Seryum (Ce), Evropiyum (Eu), Samaryum (Sm) ve Terbiyum (Tb) gibi nadir toprak elementleri ile katkılandırıldı. Molce %0,5 ile %2 aralığında yapılan katkılandırmanın (doplamaların), ters opal fotonik kristal yapılara etkisi araştırıldı.

Çalışmalar sonucunda, yapısal renkli üç boyutlu opal ve ters opal fotonik kristal kaplamlar başarılı bir şekilde üretilmiştir. Opal fotonik kristal kapalamaların yapısal renkleri, PMMA kolloid boyut değişimi ile kontrol edilebilirken, silika ters opal fotonik kristal kaplamaların yapısal renklerinin nadir toprak element katkılanması ile kontrol edilebildiği görülmüştür.

Anahtar kelimeler: Opal fotonik kristal, ters opal fotonik kristal, nadir toprak elementi katkısı, yapısal renk, silika

CONTENTS

Page

Ph.D. THESIS EXAMINATION RESULT FORM ii

ACKNOWLEDGMENT iii

ABSTRACT iv

ÖZ vi

LIST OF FIGURES xii

LIST OF TABLES xvi

CHAPTER ONE - INTRODUCTION 1

1.1 Background 1

1.2 Organization of the Thesis 2

CHAPTER TWO - TEORICAL BACKGROUND 4

2.1 Photonic Crystals 4

2.1.1 Material 5

2.1.2 Refractive Index 5

2.1.3 Light Absorption 6

2.1.4 Single Light Scattering 6

2.1.5 Bragg-Snell's Law 7

2.2 Photonic Band Gap 10

2.2.1 Pseudo and Complete Photonic Band Gaps 12

2.3 Important Properties and Parameters of Photonic Crystals 14
2.4 Types of Photonic Crystals 17
2.4.1 One-dimensional Photonic Crystals 19
2.4.2 Two-dimensional Photonic Crystals 21
2.4.3 Three-dimensional Photonic Crystals 22
2.5 Opal Photonic Crystals 23
2.5.1 Colloidal Particles (Colloids) 24
2.5.2 Self-Assembly of Colloidal Particles 26
2.5.2.1 Sedimentation 26
2.5.2.2 Vertical Deposition 26
2.5.2.3 Spin Coating 30
2.5.2.4 Langmuir-Blodgett Method 31
2.6 Inverse Opal Photonic Crystals 32
2.6.1 Optics of inverse opals 36
2.6.2 Production of Inverse Opal Photonic Crystals 37
2.6.3 Infiltration Methods 38
2.6.3.1 Electrodeposition 38
2.6.3.2 Sol-Gel 38
2.6.3.3 Chemical Polymerization 42
2.6.3.4 Chemical Vapor Deposition 42
2.6.4 Sintering 43
2.7 Applications 43
2.7.1 Photonic 44
2.7.2 Magnetic 44

2.7.3 Separation 44
2.7.4 Structural colors 45
2.7.5 Optical application 47
2.7.6 Wetting and fluidic applications 47
2.7.7 Sensing 48
2.7.8 Catalysis 49
2.7.9 Electrodes 50

CHAPTER THREE - EXPERIMENTAL PROCEDURE 51

3.1 Literature Review 51
3.2 Materials 54
3.3 Production Steps 55
3.3.1 Synthesis of PMMA Colloids 55
3.3.2 Preparation of PMMA Colloidal Crystal Templates 58
3.3.3 Sol-gel Infiltration 59
3.3.4 Heat Treatment 60
3.4 Characterizations 62
3.4.1 Fourier Transform Infrared Spectrometer 62
3.4.2 Particle Size Distribution 63
3.4.3 Differential Thermal and Thermogravimetric Analysis 64
3.4.4 X-Ray Diffraction 65
3.4.5 X-Ray Photoelectron Spectroscopy 66
3.4.6 Scanning Electron Microscopy 67
3.4.7 Optical Characterization 69

CHAPTER FOUR - RESULTS AND DISCUSSIONS 71

4.1 Opal Photonic Crystal Coatings 71

4.1.1 Effects of Sedimentation Process Parameters on Opal PC Coatings 71

4.1.2 Effect of the Synthesis Parameters on Opal PMMA PC Coatings ... 75

4.1.2.1 Results of Particle Size 75

4.1.2.2 FTIR Results 75

4.1.2.3 Morphological Characterization 75

4.1.2.4 Optical Characterization 81

4.2 Effect of Ce or Eu dopants on properties of SiO_2 Inverse Opal Photonic Crystal Coatings 84

4.2.1 Thermal and Structural Characterizations 84

4.2.2 Morphological Characterization 92

4.2.3 Optical Characterizations 95

4.3 Results of the Sm or Tb doped SiO_2 Inverse Opal Photonic Crystal Coatings 100

4.3.1 Thermal and Structural Characterizations 100

4.3.2 Morphological Characterization 108

4.3.3 Optical Characterizations 111

CHAPTER FIVE - CONCLUSIONS 117

REFERENCES 120

LIST OF FIGURES

Page

Figure 2.1 Illustrations of the (a) Snell's law and (b) Bragg's law 7
Figure 2.2 The illustration of the Bragg-Snell law 9
Figure 2.3 Presentation of the (a) light diffraction between two media according to the Snell law, and (b) anomalous reflection between a homogeneous media and PC structure. 10
Figure 2.4 The photonic band structures of (a) Yablonovite and (b) woodpile form 3-dimentional photonic crystals..... 12
Figure 2.5 The band structure in the ΓX direction and theoretically calculated transmission (located left and right respectively) for a PC structure in a square lattice form of cylinders with a refractive index contrast value of 1.5. 13
Figure 2.6 Theoretical band structures of square lattice cylinder PC for different dielectric contrast values (a) 1.5, (b) 2.0, (c) 4.0 and (d) 6.0 13
Figure 2.7 Simple illustrations of the lattice symmetries such as (a) simple cubic, (b) simple hexagonal, (c) body centered cubic, (d) face centered cubic (e) hexagonal close packed and (f) diamond lattice 15
Figure 2.8 (a) Isolated opal structure, (b) interpenetrated opal structure , (c) isolated inverse opal structure and (d) interpenetrated inverse opal topologies of the FCC lattice..... 15
Figure 2.9 Schematic illustrations of (a) one-dimensional (1-D), (b) two-dimensional (2-D) and (c) three-dimensional (3-D) photonic crystals and (d-f) related SEM examples respectively 18
Figure 2.10 Schematical illustration of 1-D PCs with (a) reflected waves in phase (b) not in phase..... 20
Figure 2.11 1-D PC structure and its calculated photonic band structures 20
Figure 2.12 Schematic presentation opal and voids of FCC opal PC structure 24
Figure 2.13 The list of some colloidal systems according to the their dimensions ... 25
Figure 2.14 Illustration of self-assembly of colloids by sedimentation method..... 29
Figure 2.15 The schematic figure of the vertical deposition method..... 30

Figure 2.16 The schematic draw of the spin coating method 31
Figure 2.17 (a) The schematic drawing of the Langmuir- Blodgett method and (b)SEM image of an monolayered colloidal crystal structure 32
Figure 2.18 Dispersion diagrams with schematically presentations of (a) opal and (b) inverse opal silica PCs..... 34
Figure 2.19 Schematic illustration of inverse opal structure from (a) top and (b) side view 34
Figure 2.20 Inverse opal application areas with synthetic strategies 35
Figure 2.21 Schematic representation of the sol-gel process for varied nanomaterials 40
Figure 2.22 Front and oblique views of the Morpho didius wings in (a-b) air and (b-c) ethanol media respectively; (e) perpendicular and (f) the parallel view of Morpho cypris wings..... 46
Figure 2.23 (a) Sensing parameters of inverse opal based PCs and (b) their response mechanisms for color changes 48
Figure 3.1 Schematic of Nelson's GaAs based inverse opal PC with an InGaAs..... 52
Figure 3.2 Zhao's visual multi-triggered sensor based on inverse opal hydrogel which responses to pH, temperature and light. 54
Figure 3.3 Flowchart of production and characterization steps 57
Figure 3.4 Experimental setup of the free radical induced polymerization of PMMA colloids 57
Figure 3.5 Schematic representation of modified fast-sedimentation processes for PMMA colloidal template..... 58
Figure 3.6 Schematically presentation of the inverse opal PCs by the sol-gel infiltration method..... 59
Figure 3.7 Heat treatment steps of the silica based coatings..... 61
Figure 3.8 Image of the used FTIR device having ATR apparatus 63
Figure 3.9 Malvern Zetasizer Nano ZS model device 64
Figure 3.10 Perkin Elmer STA 8000 TG/DTA device 65
Figure 3.11 X-Ray Diffractometer, Rigaku, D/Max-2200/PC..... 66

Figure 3.12 Thermo Scientific K-Alpha XPS device..... 67
Figure 3.13 JEOL JSM-6060 model SEM device..... 69
Figure 3.14 (a) Thermo Scientific Evolation 600 UV–VIS spectrophotometer device and (b) Nikon Eclipse ME600 model optical microscope 70
Figure 4.1 SEM images of the (a-b) F-30, (c-d) F-40, (e-f) F-50, (g-h) O-30, (i-j) O-40 and (k-l) O-50 PMMA opal coatings at 2500x and 30000x magnifications, respectively..... 73
Figure 4.2 FTIR spectra of PMMA photonic crystal coatings..... 77
Figure 4.3 SEM surface morphologies of the (a-b) PMMA1, (c-d) PMMA 2, (e-f) PMMA 3 (g-h) PMMA4, (i-j) PMMA 5 and (k-l) PMMA 6 opal PC coating samples 79
Figure 4.4 Reflectance spectra of the PMMA opal photonic crystal coatings..... 81
Figure 4.5 Surface images of the (a) PMMA1, (b) PMMA 2, (c) PMMA 3, (d) PMMA 4, (e) PMMA 5, (f) PMMA 6 opal PC coatings taken from optical microscope 82
Figure 4.6 (a) DTA and (b) TGA diagrams of the un-doped and Ce doped silica inverse opal PC coatings, respectively 86
Figure 4.7 (a) DTA and (b) TGA diagrams corresponding to un-doped and Eu doped silica inverse opal PC coatings, respectively 87
Figure 4.8 XRD patterns of the un-doped and Ce or Eu doped inverse opal SiO_2 PC coatings..... 89
Figure 4.9 (a) General XPS results of the inverse opal PC coatings. High-resolution XPS scans of Ce or Eu doped PC coatings over (b-c) Si 2p and (d-e) O 1s. XPS scans over (f) Ce 3d and (g) Eu 3d dopant peaks of PC-C200 and PC-E200 samples..... 90
Figure 4.10 SEM images of the (a) un-doped, (b) 0.25%, (c) 0.50 %, (d) 1%, (e) 2% Ce doped; (f) 0.25%, (g) 0.50 %, (h) 1% and (i) 2% Eu doped SiO_2 based coating samples in the thin film (TF) and PC forms..... 93
Figure 4.11 UV-Vis reflectance spectra of the (a) Ce and (b) Eu doped thin film and PC coatings..... 96

Figure 4.12 Optical images of the (a) un-doped, (b) 0.25%, (c) 0.50 %, (d) 1%, (e) 2% Ce doped; (f) 0.25%, (g) 0.50 %, (h) 1% and (i) 2% Eu doped SiO_2 based coating samples in the thin film and PC forms 97
Figure 4.13 (a) DTA and (b) TGA diagrams of the un-doped and Sm doped silica inverse opal PC coatings 102
Figure 4.14 (a) DTA and (b) TGA diagrams of the un-doped and Tb doped silica inverse opal PC coatings 103
Figure 4.15 XRD patterns of the un-doped, Sm or Tb doped SiO_2 based inverse opal PC coatings..... 104
Figure 4.16 a) General XPS results of the inverse opal PC coatings. High-resolution XPS scans of Sm or Tb doped PC coatings over (b-c) Si 2p and (d-e) O 1s respectively. XPS scans over (f) Sm 3d and (g) Tb 4d peaks of PC-S200 and PC-T200 PC coating samples, respectively..... 106
Figure 4.17 SEM images of the (a) un-doped, (b) 0.25%, (c) 0.50 %, (d) 1%, (e) 2% Sm doped; (f) 0.25%, (g) 0.50 %, (h) 1% and (i) 2% Tb doped SiO_2 based samples in the thin film and PC forms 109
Figure 4.18 UV-Vis reflectance spectra of the (a) Sm or (b) Tb doped coating samples 113
Figure 4.19 Optical images of the (a) un-doped, (b) 0.25%, (c) 0.50 %, (d) 1%, (e) 2% Sm doped; (f) 0.25%, (g) 0.50 %, (h) 1% and (i) 2% Tb doped SiO_2 based coating samples in the thin film and PC forms 114

LIST OF TABLES

Page

Table 3.1 Sample abbreviations according to production conditions of the PMMA colloids..... 57

Table 3.2 Abbreviations of PC and thin-film coatings according to the coating type, dopant species and dopant ratio..... 61

Table 4.1 Particle size and polydispersity results of the PMMA samples..... 76

CHAPTER ONE
INTRODUCTION

1.1 Background

Throughout the history of humanity, nature has always been a priceless inspiration for the development of technology (Turduev, 2015). The structural color that was observed firstly from peacock feathers and butterfly wings has been attracting attention from 19th to 20th century (Kinoshita et al., 2002). Once these natural structures were investigated, it was observed that the reason for the coloration was regularly arranged distinct dielectric zones. Thus, photonic crystal (PC) technology took the stage. The following explanations can be announced if the words that make up the PC term are examined one by one. It is called “crystal” because it consists of periodically arranged dielectric building blocks similar like atoms forming in the crystal lattice. As PC materials are used to control and manipulate the flow of light, "photonic" term is entitled (Santamaría, 2003).

Apart from its visual effects, photonic crystals can lead to today's technology with its unique features. The most remarkable claim of PC is that its structure affects the photons as do semiconductor materials affect electrons (Rahman, 2017). For instance, the miniaturization and acceleration of electronic devices can be made possible by PC materials, where electrons are replaced with much faster photons. In addition, since there is no interaction of photons with particles unlike electrons, it will be an energy-enhancing factor for energy consuming systems (Turduev, 2015). PC materials with many unique features like these are one of the important titles worth to research.

The first appearance of the PCs on the stage of history was the study of electromagnetic wave propagation in a periodic medium related to the one-dimensional PC by Lord Rayleigh in 1887 (Rayleigh, 1887). In this study, it was proposed that photonic bandgap could be obtained by one-dimensional periodic structures. However, Yablonovitch and John who are known as the real inventors of photonic crystals introduced the idea of PC, in the early 1987s (after 100 years) (John,

1987; Yablonovitch, 1987). Their ideas can be regarded as the seeds of the PC concept. Yablonovitch concentrated on controlling the spontaneous emission using periodic dielectric mediums with various photonic density (Yablonovitch, 1987). John's perspective was to understand if photon localization could be affected by random refractive-index variations (John, 1987). Both researchers agreed that the photons interacting with different dielectric environments would influence the electromagnetic spectra and gain unique properties (Turduev, 2015). This can only be achieved by a geometric design with an appropriate wavelength scale with a high contrast refractive index variation. Such electromagnetic bandgap materials were later called as "photonic crystals". The potential of PC materials emerges when the potential of electrons in a crystal lattice system transferred from the atomic dimension to the macroscopic dimensions. If the dielectric contrast between the layers is sufficiently high enough, light absorption becomes minimal, and many photons can be scattered at identical frequencies from the regularly arranged interfaces. Therefore, the photonic crystal materials with low energy loss could perform optical control and manipulation (Kurt, 2006; Turduev, 2015). The first successful experimental PC was obtained with a diamond-like structure produced by drilling holes in a bulk dielectric material in 1991 (Yablonovitch, et al., 1991).

1.2 Organization of the Thesis

In this thesis, PMMA based opal photonic crystal coatings and; Cerium, Europium, Samarium or Terbium rare-earth element doped photonic crystal coatings were produced by the sol-gel infiltration method. The main purpose of the thesis is optimization of the opal PC production and to determine the effect of rare-earth dopants on structural, morphological and optical properties of silica based inverse opal photonic crystal coatings.

Thus, Chapter 1 presents an introduction to the thesis. A short explanation and historical development of photonic crystal are given. Also, here we present the organization of the thesis.

In Chapter 2, the theoretical background of photonic crystal technology is explained. Detailed information about the photonic crystals such as photonic band gap, important parameters, basic forms, and application areas are given in this chapter. Chapter 2 is completed with a literature review part.

The experimental part of the thesis is clarified in Chapter 3. The synthesis and characterization methods of the photonic crystal coatings are given in detail. Information about the used chemicals at the production steps are listed. The first stage of inverse opal photonic crystals is preparing the ordered opal template. The production of this PMMA based opal template by fast-sedimentation technique is explained. Then, sol-gel infiltration method for inverse opal photonic crystal production is clarified. Chapter 3 ends up with the presentation of characterization instruments, which are used in thesis studies. Thermal, structural and optical properties were characterized via Thermo-gravimetric analysis (TGA), Differential thermal analysis (DTA), Fourier Transform Infrared Spectroscopy (FT-IR), Particle Size Distribution, X-Ray Diffractometer (XRD), X-ray photoelectron spectroscopy (XPS), Scanning Electron Microscope (SEM), UV Spectrophotometer (UV-Vis) and Optical Microscope (OM).

Chapter 4 covers all characterization results of the PMMA-based opal and silica-based photonic crystal coatings. The effect of PMMA synthesis and sedimentation parameters on PMMA opal coatings are investigated while rare earth dopants on the structural, morphological and optical properties of inverse opal photonic PCs are revealed. Inferences such as what is the reason for these results were discussed scientifically in detail. Some results were examined using graphs in order to make better comparisons. Finally, general conclusions of the study and future plans are presented in Chapter 5

CHAPTER TWO
TEORICAL BACKGROUND

2.1 Photonic Crystals

PCs are defined as materials that exhibit a periodic refractive index variation in one, two or three dimensions. The length and distance of the refractive variation are related to the wavelength range at which the material is designed. In order to manipulate the properties of PC materials, especially the spectral properties, it is necessary to take under control parameters such as the effective refractive index contrast, symmetry, lattice parameter, dimensionality, and the topology. By adjusting these parameters, PC materials interact with light, similar to the interaction of electrons in semiconductor materials. In other words, energy gaps occur in the structure that does not contain some energy levels. In PC materials, the refractive index plays a similar role to the periodic atomic potential of electrons in semiconductors (Espinha, 2015).

The principles of solid-state physics and Maxwell's equations of the electromagnetic field are essential for PC structures to understand the interaction of light with periodic dielectric structures (Aryal, 2007). PC materials also can be considered as periodic structures with interface transitions that will cause coherent reflection of a particular wavelength. In such structures, interactions occur within the Bragg reflection. If the incident light with a given wavelength reflected coherently waves with each other after interacting with the material, the whole wave energy can be reflected. If the reflected waves are not in the same phase, the total wave travels through the structure instead of reflecting (Phillips, 2016).

In a semiconductor material, atomic lattice provides a periodic potential to allow the movement of electrons through the electronic lattice. This potential creates an energy gap in which electrons cannot move in any direction within a certain energy range. The refractive index variation of PC materials likewise leads to the formation of a photonic bandgap (PBG). All of the light is reflected by preventing the propagation and movement of light in the complete PBG similar to the electronic band

gap. With the discovery of the PBG technology, many applications such as trapping of photons, zero-threshold lasing and spontaneous emission have been emerged (Rahman, 2017).

2.1.1 Material

In order to obtain high dielectric contrast in photonic crystal systems, low dielectric air or water and high dielectric metal oxide materials are generally preferred. In spite of the fact that dielectric materials cannot conduct electricity, they can be polarized under an electric field. Due to fact that metal oxides are derived by the oxidation of a metal, they are very plenty on the earth. The most important thing that provides this semi-conductivity is the electronic band gap (EBG). The EBG consists of the gap between a valence band and a conduction band. The valence band is located under the gap forms the possible and filled states for the electrons while and a conduction band located above the gap forms the possible and unfilled states. This EBG can be considered as an obstacle of the material for electrical conductivity. Yet, if they are excited the material can be made conductive by eliminating the obstacle. Electron needs to absorb energy equal or higher to EBG energy in order to heighten an electron to an empty state. The general EBG values between 1eV and 5eV corresponds to around 1240-250 nm wavelength range for metal oxide materials. Thus, depending on the size of their EBG values metal oxides can absorb near-ultraviolet, visible and infrared light (Lebrun, 2014).

2.1.2 Refractive Index

The refractive index of a material (n) can be termed as dimensionless reflection quantity of the light speed within the material. The characteristic behavior of the waves at the boundaries of the two materials is determined by the refractive indexes of the materials. The speed of light ($c = 2.997 \times 10^8\ m/s$) is the constant in a vacuum medium as nothing block the light propagation. Light speed in the material is compared to light speed in the vacuum in order to determine the behavior of light waves in a

material. Light gets slower and more reflected in the higher refractive index medium compared to the low refractive index medium (Lebrun, 2014).

2.1.3 Light Absorption

Photon absorption could be diversified according to the material, light wavelength, and polarization. The absorption of a photon is a transition of an electron or phonon to a higher energy level. It occurs local and very fast (femtosecond domain) (Phillips, 2016). Because of the momentum of a photon much lower than an electron, if an electron absorbs light the small momentum of photons refers that no change of momentum occurs. Electrons are used this extra energy for rising to an excited state. Some events can occur after the absorption of light by an electron. One option is the creation of an electron-hole pair and its separation. Another option is the formation of an electron-hole pair and its recombination or last option is trapping of the electron in an intermediate state. The recombination rate would be high for the direct band-gap materials whilst the creation of an electron-hole pair would be low for indirect band-gap material depending on the material. A hole that can be considered as a particle is likely a positive version of an electron and moves in the valence band. Thus, metal oxides can conduct electricity by the mobility of both electrons and holes. Excess photon energy would be released after the recombination of an electron and a hole. Adding dopant elements causes the creation of a secondary possible state within the electronic band-gap. Therefore, metal oxide semiconductors could be excited by absorbing smaller energies (Lebrun, 2014).

2.1.4 Single Light Scattering

Light spread out along straight lines from the luminous light source and those lines scatter (bend or break) when passing out between the mediums. Light scattering is a basic fact for light transport as Newton stated. In addition, it is practically not possible to observe the light directly from its source. Due to the scattering, most of the emitted light reaches our eyes in an indirect way. In-homogeneities or light speed variations can destroy the straight propagation of light. The speed of light in a medium can be

characterized by the refractive index n, which was defined above as the ratio of light speed in the vacuum and in the medium. The interface between media causes a deviation in the light propagation direction due to the refractive index contrast between the media. Scattering is an in-homogeneous phenomenon in an all-homogeneous medium (Fernandez, 2008).

2.1.5 Bragg-Snell's Law

The Bragg-Snell's law (2.3) that was put forward could be used in order to determine the photonic band-gap (PBG) position of the PC materials to some extent. It was derived from the Snell's law (2.1) and the Bragg's law (2.2) combination. The most important requirements are the ordered structure and refractive index contrast between the media. The representation of Snell's law is given in Figure 1 (a). Snell's law can be used to characterize the simple geometric interface between two different materials or media and explain the effect of the boundary (Lebrun, 2014).

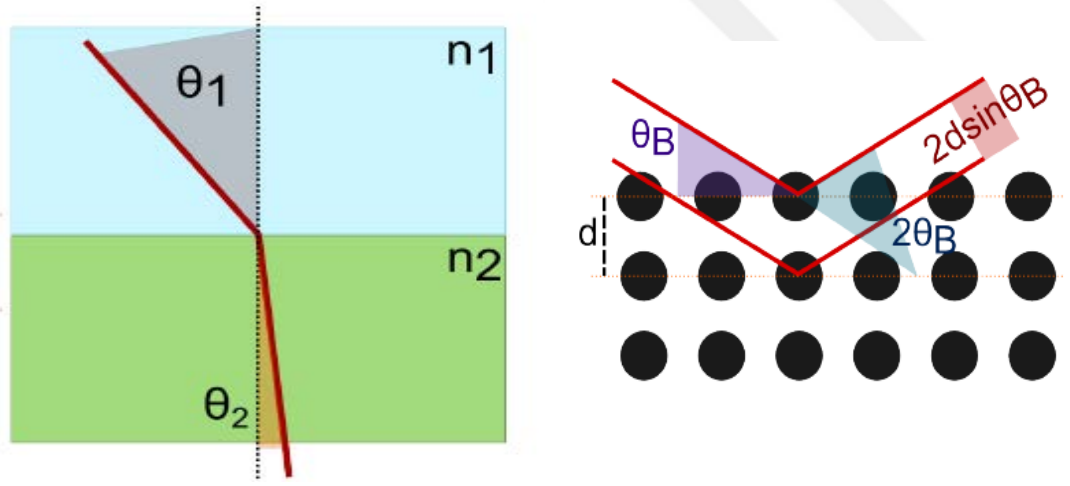

(a) (b)

Figure 2.1 Illustrations of the (a) Snell's law and (b) Bragg's law (Lebrun, 2014)

Snell's law can be given as;

$$\frac{\sin\theta_1}{\sin\theta_2} = \frac{n_2}{n_1} \tag{2.1}$$

where n_1 and n_2 are refractive indexes of the two media, θ_1 and θ_2 are the angles of the light between normal line.

Bragg's law describes the interaction between a wave and a crystalline object. It is generally applied for determining crystalline structures of the materials with the X-ray diffraction patterns. An illustration of Bragg's law that is represented in Figure 2.1 (b), determines constructive interferences of the diffracted waves.

$$2d \sin \theta_B = n\lambda \tag{2.2}$$

in which d the distance between planes, θ_B represents the Bragg angle, n the exact order number (n=1,2,3...), λ is the related wavelength. The Bragg-Snell law deals with refractive indices and incidence angles determining the reflected wavelength by ignoring absorption effects (Lebrun, 2014).

$$\lambda = 2d_{hkl}\sqrt{n_{eff}^2 - sin^2\theta} \tag{2.3}$$

If the close-packed (111) planes are geometrically parallel to the top surface:

$$d_{111} = D\sqrt{\frac{2}{3}} \tag{2.4}$$

where D is the distance of the periodicity or lattice constant, d_{hkl} is the space between planes, n_{eff} is the average refractive index of the PC structure and θ is the incident angle between the normal axis of the material. For a better understanding of the terms, the visualization of the Bragg-Snell law is given in Figure 2.2. Light is refracted from the material surface and diffracted into the material. The real refractive index, n_{eff} can be found easily for two materials. Yet, it is very difficult for multi-layered materials or complex structures with high absorption (Lebrun, 2014).

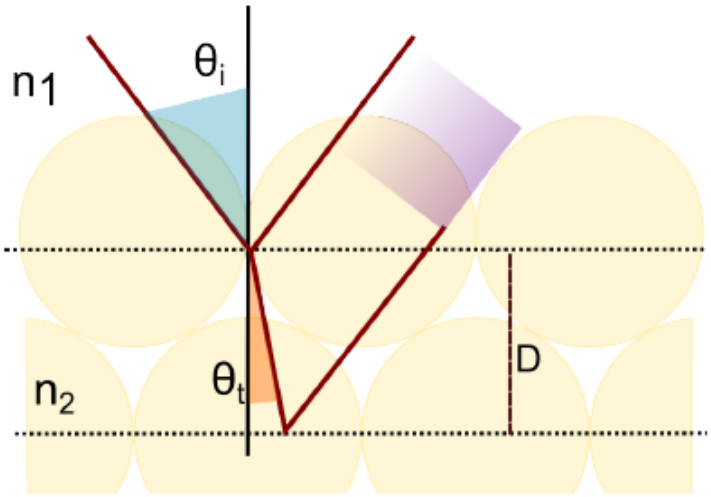

Figure 2.2 The illustration of the Bragg-Snell law (Lebrun, 2014)

Even though Bragg's law is basically used for characterization of the specific lattices and the material phases, it can be also used to get information of all states of matter similar to the distance between the related atomic, molecular or dielectric layer structures using diffractions of any beam, e.g., ions, electrons, neutrons, protons, and photons, with a wavelength (Aryal, 2007). Multilayer PCs in one or two or three-dimensional form diffracts photons just like diffracting X-rays from a crystal. Due to alternating high and low refractive indexed layers, Snell law comes into play similar to the crystalline atomic planes. If the phases of the reflected waves are coherent, the multilayer PC gets maximum reflectivity. Some frequency regions are diffracted from PC structure due to the dielectric media according to Bragg-Snell law (Aryal, 2007).

Snell law is a more simple kind of light reflection. The light that travels between the mediums with different refractive indexes is exposed to a shift in the propagation direction. The parallel pieces and energy of the wave-vector should be preserved in the reciprocal space. Keeping the light wave vector (k) components parallel to the interface of the mediums and dispersion surface energies in both media according to energy conservation could be used in order to adjust light reflection (Fernandez, 2008).

The schematic draw of the light refraction occurred between two homogeneous media with a different refractive index is given in Figure 2.3 (a). Light refraction acts

more complex in a photonic crystal structure. In these materials, dispersion surfaces can adapt to very complicated patterns with the complicated dispersion relation. A similar example is given in Figure 2.3 (b) where the complicated refraction is observed from a homogeneous medium into a PC structure with a dedicated dispersion interface. The related phenomenon is called anomalous refraction (Notomi, 2000). The wave-vector inside the PC structure (the second medium, k_2) is determined by keeping its components parallel to the interface just like in the homogeneous medium matter. Yet, the wave-vector is not parallel to the energy propagation direction is given by the group velocity in a PC structure as well as in a homogenous medium (Fernandez, 2008).

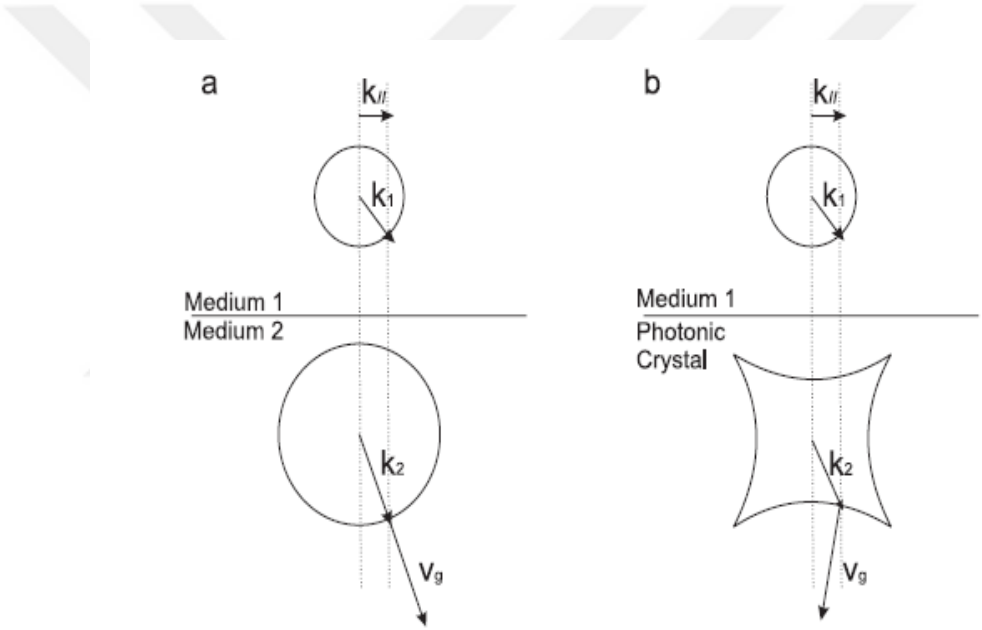

Figure 2.3 Presentation of the (a) light diffraction between two media according to the Snell law and (b) anomalous reflection between a homogeneous media and PC structure (Fernandez, 2008)

2.2 Photonic Band Gap

If the subject is a band gap, the first thing that comes to mind is generally electronic band-gap found in semiconductors or insulators. EBG symbolize an energy range forbidden to all electrons in the crystal. Also, EBG can be taught as a block between the valence band and the conduction band (Fernandez, 2008). It is a high possibility that local band gaps that not extend in all directions could be observed. Once photonic

crystal technology replaces semiconductor technology, it is a photonic band gap instead of an electronic band gap. The PBG appears as an absence of bands in a photonic band structure. Yet, the related energy gap of a wavelength does not mean to occupied or un occupied energy states unlike to the EBG. The most meaningful explanation for PBG is that photons charged by energy equal to the related PBG cannot penetrate inside the PC material (Lebrun, 2014).

Another important point is that the PBG consists of just structural, contrary to an EBG. Allowed and forbidden bands can be created by only the periodicity of the structure near to the desired light wavelength. Some local and complete gaps at different wavelengths could be observed. The PC structure reflects all light located in the forbidden band gap, so the related light cannot pass through the structure. If there is not any absorption phenomenon, all light in the PBG is reflected. The group velocity of light comes to near zero at the edges of the PBG (Chen et al., 2008).

This phenomenon can be referred to as slow down of light. This has paved the way for further studies on slow light (Chen et al., 2008; Lebrun, 2014). PC materials are potential candidates for tuning light properties not only as they have PBG but also as they have the ability to control light group velocity. The group velocity can be thought of the speed at which the wave energy spread out within the structure. An example illustration is given in Figure 2.4 where the photonic band structures of (a) Yablonovite and (b) woodpile form 3-dimentional photonic crystals are shown.

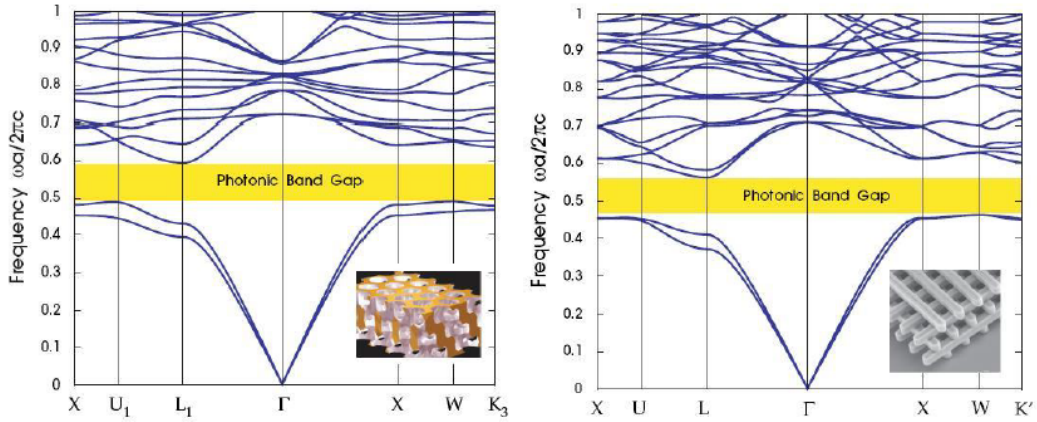

(a) (b)

Figure 2.4 The photonic band structures of (a) Yablonovite and (b) woodpile form 3-dimentional photonic crystals (Joannopoulos et al., 1997)

2.2.1 Pseudo and Complete Photonic Band Gaps

Light is scattered from the interface of the different dielectric regions after it penetrates into a PC structure. Scattered waves can become coherent for certain directions and frequencies owing to the dielectric periodicity. Consequently, some propagation directions with certain energies are forbidden. The photonic band gap can be described as an energy range not covered by any band in the related direction, in the photonic band structure diagram.

If the PC structure has almost no refractive index contrast between different dielectric media, the scattering effect is very low and PBG does not observe. Nevertheless, if the refractive index contrast is high enough, photonic gaps begin to form in the PC structure. The theoretical transmission spectrum and band structure for the ΓX direction for the PC structure with a refractive index contrast of 1.5 are given in Figure 2.5. The energy region where no bands are available can be observed in the band structure between the first and second band (black and red plates). Herewith, the transmission goes to zero at those frequencies because photons with these energies cannot propagate through the structure (Santamaría, 2003).

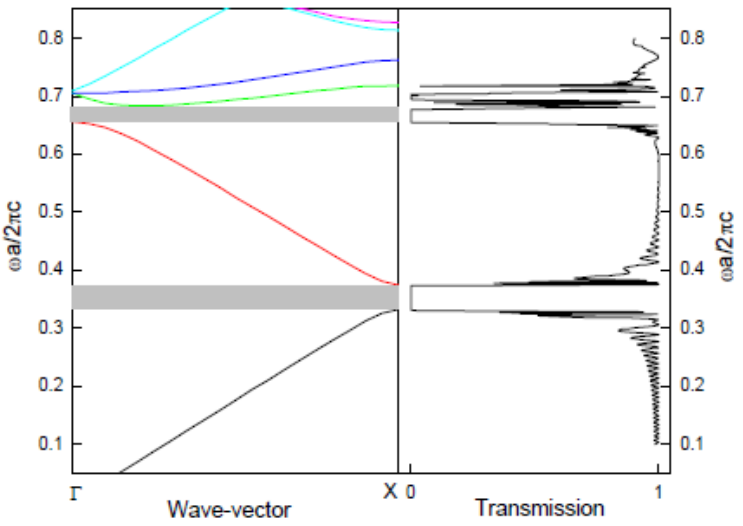

Figure 2.5 The band structure in the ΓX direction and theoretically calculated transmission (located left and right respectively) for a PC structure in a square lattice form of cylinders with a refractive index contrast value of 1.5 (Santamaría, 2003)

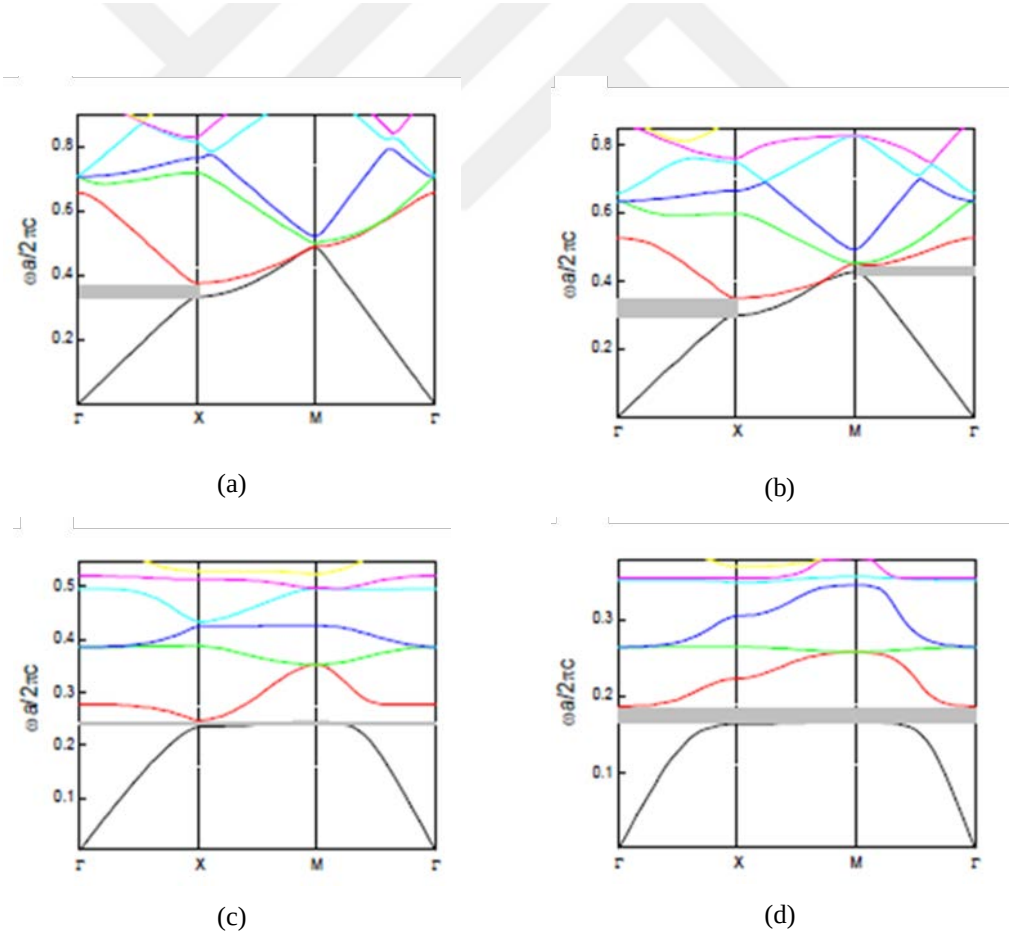

Figure 2.6 Theoretical band structures of square lattice cylinder PC for different dielectric contrast values (a) 1.5, (b) 2.0, (c) 4.0 and (d) 6.0 (Santamaría, 2003)

If a certain wavelength is prohibited for some directions in the PC material, it is called as pseudo photonic band gap (pPBG) while inhibited for all directions; it is called the complete photonic band gap (cPBG). Creating a cPBG is extremely depends on forming a structure with a high dielectric contrast. An important example is given in Figure 2.6 where theoretical band structures are drawn according to the dielectric contrast values for square lattice cylinder PCs. As can be seen from Figure 2.6, cPBG can be only observed at higher dielectric contrast than the value of 4, for square lattice cylinder PC materials. The pPBG structures can be observed in Figure 2.6 (a) and (b) where dielectric contrast is lower. It should be noted that the generation of cPBG is not only depended on refractive index contrasts but also, proper symmetry and topology play a very important role as well (Santamaría, 2003).

The pseudo gaps for all propagation directions have to be overlapped in order to get a cPBG. High dielectric contrast generally encourages this overlapping by widening of gaps. Yet, when the pseudo gaps open at very dissimilar energies for different directions, the overlapping possibility is reduced. Gaps can be observed at the wave-vectors that lay on the Brillouin zone boundary according to the solid state physic. Therefore, PC structures with circular Brillouin zone have a high advantage to obtain a cPBG (Santamaría, 2003).

2.3 Important Properties and Parameters of Photonic Crystals

Properties of PC materials depend on some parameters. In order to obtain desired property such as cPBG or a specific band, the effects of these parameters should be investigated.

- *Refractive index contrast:* It is one of the most important PC parameters. The refractive index contrast refers to the scattering power level of a two-component photonic crystal. This parameter can be calculated using dielectric values of the high dielectric media and

low dielectric media, as ratio of n_{high}/n_{low}. The higher this ratio, the more likely obtain a cPBG (Santamaría, 2003).

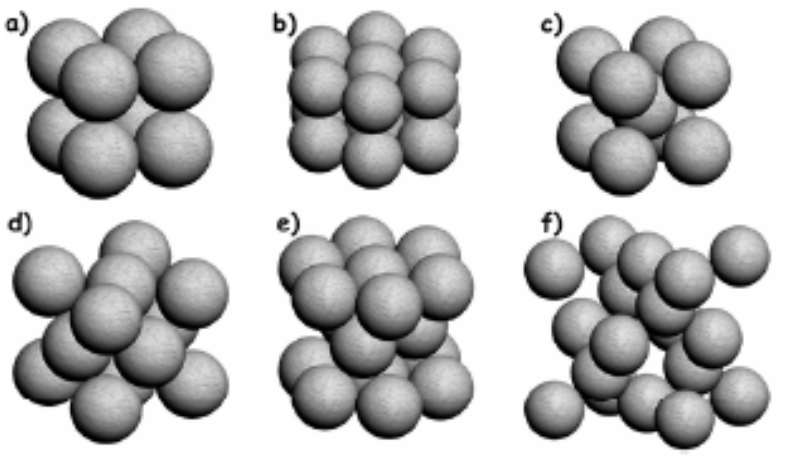

Figure 2.7 Simple illustrations of the lattice symmetries such as (a) simple cubic, (b) simple hexagonal, (c) body centered cubic, (d) face centered cubic (e) hexagonal close packed and (f) diamond lattice (Santamaría, 2003)

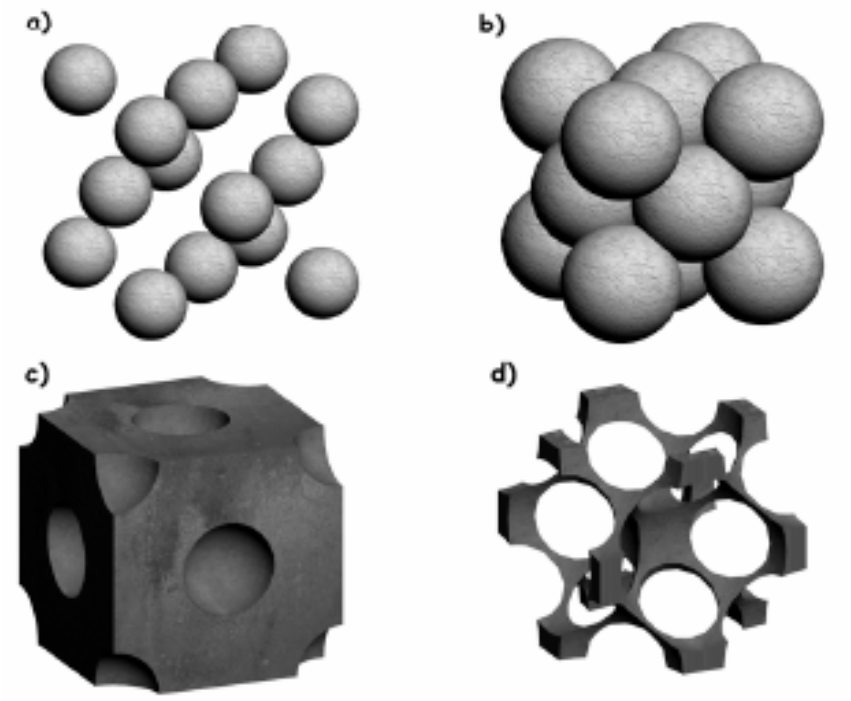

Figure 2.8 (a) Isolated opal structure, (b) interpenetrated opal structure (c) isolated inverse opal structure and (d) interpenetrated inverse opal topologies of the FCC lattice (Santamaría, 2003)

- *Dimensionality:* The dimensionality of the PC is determined according to the periodicity of the refractive index. PC materials are divided into three basic groups according to the dimensionality such as one-dimensional (1-D), two-dimensional (2-D) or three-dimensional (3-D) PCs. It is determined according to the numbers of the spatial planes where dielectric variations are observed (Santamaría, 2003).

- *Filling fraction and effective refractive index:* Filling fraction is the relative quantity of material that generates the scattering building block. In order to express the filling fraction, the volumes of the components forming the photonic crystal structure are taken into consideration. The effective refractive index (n_{eff}) of the PC body can be found as the square root of the average dielectric constant. The effective refractive index is another important parameter that determines the optical spectrum wavelength range of PC like dielectric contrast (Santamaría, 2003).

- *Symmetry:* The sequence of the PC building blocks assigns the symmetry of the body. A wide variety of symmetries is available, notably for three-dimensional photonic crystals. Simple hexagonal, simple cubic, face-centered cubic and body centered cubic structures are some examples of several three-dimensional symmetries similar to found in Bravais lattices. Adding extra atoms within the Bravais lattices, a new PC lattice symmetry can be obtained such as hexagonal close-packed and diamond structures. Simple illustrations of these lattice symmetries are given in Figure 2.7 (Santamaría, 2003).

- *Topology:* The photonic band structure can be strongly affected topology variations of the lattice with a given symmetry. The topology of the PC structures is diversified by interpenetrating the building blocks such as network topology or exclude them such as cermet

topology. One symmetry can contain any kind of topology. As an example, different topology illustrations of the FCC lattice are given in Figure 2.8 (Santamaría, 2003).

- *Lattice parameter:* Lattice parameter is determined according to the separation distance between the scattering building blocks. For instance, it is generally taken as the side of the cube for cubic lattices. Lattice parameter is another important point that determines the working wavelengths range of the optical spectrum of PC material (Santamaría, 2003).

- *Scalability:* As can be noticed there is not any variable about length scales or dielectric constant value in PC equations. But yet, obtained result from theory is fully scalable. The result that was concluded from a single length scale is valid for all other length scales. The filling factor and refractive index contrast are directly proportional to the lattice parameter and all of these parameters determines the PC working spectrum region. The desired frequency is generally normalized by the lattice parameter as if the rest of the features kept unchanged. Consequently, if the mode frequency divided by two, the lattice parameter will be doubled (Santamaría, 2003).

2.4 Types of Photonic Crystals

PC materials are divided into three basic groups according to the numbers of the spatial planes where dielectric variations are observed such as one-dimensional (1-D), two-dimensional (2-D) or three-dimensional (3-D) PCs. If the periodic media with dielectric contrast is located in only one spatial variable such as z and does not depend on x and y, PC material is called as one-dimensional (1-D). The light can travel through periodic modulation of permittivity only in one direction. Bragg mirrors that are

generally used in vertical-cavity surface-emitting lasers are one example of 1-D PC materials (Koyama, 2006).

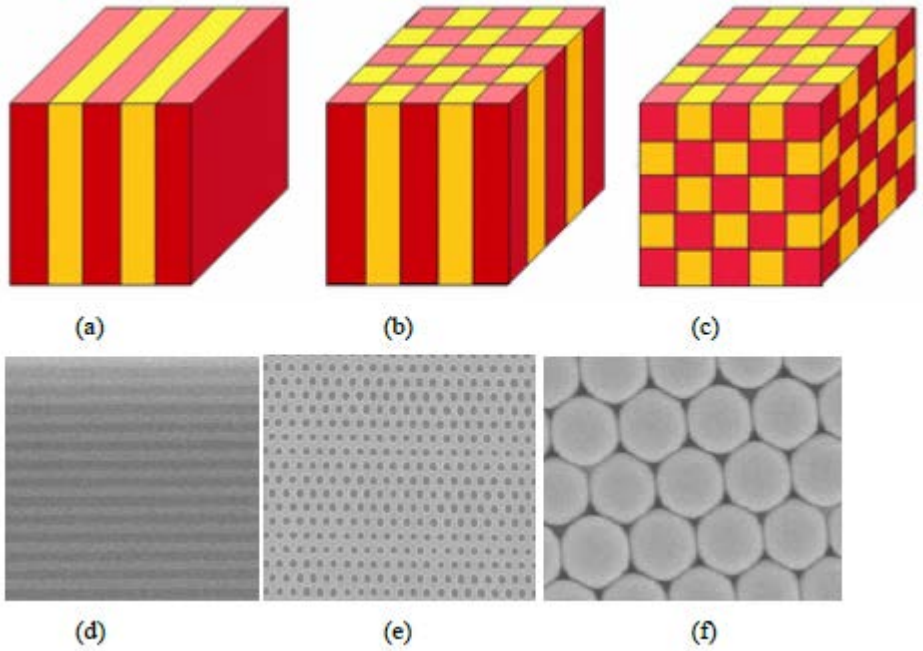

Figure 2.9 Schematic illustrations of (a) one-dimensional (1-D), (b) two-dimensional (2-D) and (c) three-dimensional (3-D) photonic crystals and (d-f) related SEM examples respectively (Rahman, 2017)

If the periodic media with dielectric contrast is located in two spatial variables, x, and y, not on the third, z; it is called as two-dimensional (2-D). The periodicity of the permittivity along two directions is uniform in 2-D PC materials (Rahman, 2017). The order of the body does not change on two linearly independent vectors in the x and y plane.

The ordered dielectric media located for all three linearly independent vectors in x, y, and z planes is called a three-dimensional (3-D) PCs. The permittivity modulation is equal for all three directions in 3-D PC structure. Yablonovich and John are the pioneer researchers who were proposed 3-D PCs with cPBG property (Rahman, 2017). Some examples of these periodic structures can be observed in nature such as frustules of some unicellular algae or on the butterfly wing surfaces (Contu, 2011; Wickham et al., 2006). Schematic illustrations and related SEM examples of photonic crystals

according to the dimension number such as one-dimensional (1-D), two-dimensional (2-D) and three-dimensional (3-D) photonic crystals are given in Figure 2.9 (Córcoles, 2010).

2.4.1 One-dimensional Photonic *Crystals*

In spite of the fact that 1-D PCs are very simple systems, they show most of the physical properties of the more complex 2-D and 3-D PCs. Therefore, in order to obtain an intuitive understanding of photonic band structures and the origin of PBGs, it is considered the case of 1-D PCs in more detail (Aryal, 2007). Two distinct approaches would be stated such as: the first one based on the evolution of the photonic band structure, the second one on Bragg's law. Both approaches are complementary to explain the origin of PBGs.

Figure 2.10 depicts a multilayer building of a 1-D PC with lattice constant "a". It is periodic in the z-direction and homogeneous throughout the other two directions. Here, it is assumed that light is propagating along the z direction. The wave-vector k can only assume discrete values along z since the structure is periodic along that direction. Optical properties of the Bragg mirrors are well known. Because the index variation is only along one direction, the PBGs are limited to light propagating along that direction. The light reflection from the Bragg mirror is owing to the 1-D band gap present in it. Nonetheless, this traditional and simple structure shows most of the physical properties of the more complicated 2-D and 3-D PCs (Aryal, 2007).

Photonic band structure is calculated for 1-D PC plotted in the Figure 2.11. The most important property in band diagram is the existence of frequencies where no modes are available in the direction of periodicity. As mentioned before such areas are called as photonic band gaps and represent the main property of PCs. For these frequencies contained in this spectral range, light propagation within the sample is not allowed. Depending on if the gap takes place for every direction in reciprocal space or just for some of them, one obtains respectively a full PBG or a pPBG (Blanco et al., 2000; Garcia, 2011; Yablonovitch, Gmitter, & Leung, 1991).

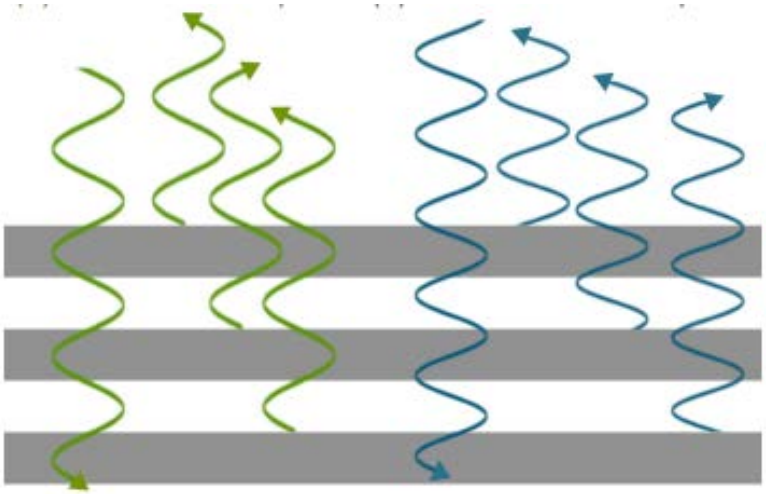

(a) (b)

Figure 2.10 Schematical illustration of 1-D PCs with (a) reflected waves in phase (b) not in phase (Phillips, 2016)

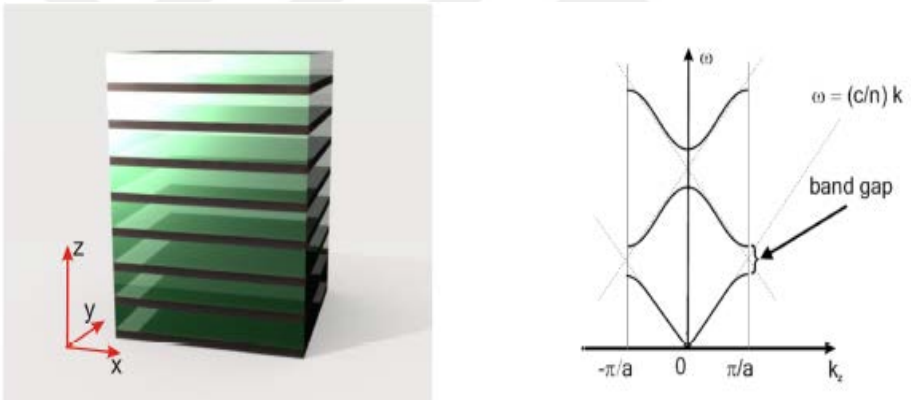

Figure 2.11 1-D PC structure and its calculated photonic band structures (Garcia, 2011)

Particular case of the 1-D periodicity also known as Bragg stack it shows the simplest PC and hence the one to be modeled in the most accurate manner. The dispersion relation light propagating along the direction of periodicity will encounter an energy gap whose spectral position and width depends on the refractive indices of n_1 and n_2 and the periodicity of the modulation. Distributed Bragg reflectors are 1-D PC structure consists of dielectric multilayers benefits from the multiple interferences that formed when a light beam is reflected from different dielectric layers. Based on the number of layers, their refraction index and size for a specific range of wavelengths, the structure offers a high reflectivity. The most common applications of

the distributed Bragg reflectors are sensors of the light polarization, filtering, micro cavities and waveguides (Córcoles, 2010).

The main reasons behind the use of this system are relatively simple modelling and the existence of well-developed fabrication process to study basic concepts of both experimental and theoretical. They have also been utilized in many applications as for such as solar cells, sensors and hollow optical fibres. Nonetheless, related to the confinement of light, 1-D PCs are not a suitable structure given that they behave as a homogenous medium for light propagation in the other two directions perpendicular to the periodicity (Garcia, 2011). Various attributes of the structure can lead to changes in the reflection peak. When standard Bragg equation is applied to PCs rather than a generic periodic structure (such as atomic crystals), then Snell's law must be taken into account.

The quantitative changes described by the Bragg-Snell equation can be understood qualitatively. If the periodicity of the 1-D PC structure is decreased, the reflected light blue-shifts as coherent scattering occurs for shorter wavelengths. A high refractive index material causes a red shift at the reflection peak by slowing down the light, effectively lengthening the wavelength. The incident light angle correlative to the periodic structure also plays a role in establishing the reflection peak. Instinctively, it could be thought that the reflected wavelength will red shift for oblique incidence angles as the length of the optical path in the first layer increases. However, theoretically the reflected peak, in fact, blue shifts, inasmuch as the relative distance that the wave travels decreases according to the Snell-Bragg law (Phillips, 2016).

2.4.2 Two-dimensional Photonic Crystals

As mentioned just before, two-dimensional (2-D) PCs have periodic media with dielectric contrast in two spatial variables. The PBG can be acquired in most of the 2-D PC materials when the structure has sufficiently high refractive index contrast. 2-D PBG which located propagation in the periodicity perpendicular plane to the rod axis can occur if the refractive index contrast between the cylinders (rods) and the background (which is generally air) is sufficiently large (Weisbuch et al., 2000).

Generally speaking, it is possible to encounter two kinds of 2-D PC materials. The first one consists of air holes in a dielectric region (low dielectric rods in a connected higher dielectric lattice) while the second one consists of dielectric rods in air host (high dielectric pillars embedded in a low dielectric medium). The 2-D PC structures can be divided into four basic categories according to their value of vertical index contrast. They can be listed as membrane holes, membrane pillars, deeply etched holes and deeply etched pillars (Weisbuch et al., 2000).

2.4.3 Three-dimensional Photonic Crystals

In spite of the fact that 1-D photonic crystals have been well studied for decades in the form of highly reflecting dielectric Bragg mirrors, the idea of constructing 2-D or 3-D PCs is no more than around two decades old. Three-dimensional PCs have attracted enormous attention from scientists due to the prediction of highly unusual properties, such as complete 3-D PBGs, and various applications. Some of the stated three-dimensional PC structures are the silicon woodpile structure (Staude et al., 2010), the layer-by-layer structure (Li et al., 2003), Yablonovite structure (Chelnokov et al. 2000), opal (Dalmis et al., 2019a) and finally inverse opal (Wang & Caruso, 2001).

Opal based PCs are the most extensively studied ones among the 3-D photonic crystals, due to the fact that they can be synthesized relatively with ease by colloidal self-assembly method (Aryal, 2007; Schroden et al., 2002; Wijnhoven & Vos, 1998). Opal structures have been used as three dimensional photonic crystals for core-shell structures, photonic pigments with iridescence, elements of composites for tuning colors under different stimuli, and templates for inverse structures, although they do not have a complete PBG (Velez, 2010). Though, 2-D photonic crystals have many of the features that 3-D photonic crystals have they cannot confine light in the third direction. Control of photons in three-dimension can be obtained by a 3-D periodic dielectric structure i.e., three-dimensional photonic crystals.

Synthetic opals or colloidal photonic crystals consist of ordered spheres whose diameter sizes are comparable to the visible light wavelength, produced by a colloidal self-assembly process. The high monodispersity of the spheres allows the formation of the face-centered-cubic structure by the minimum free energy configuration. Bright visible iridescence color observed from the microsphere arrays due to Bragg reflections of the crystallographic planes of the structure (Velez, 2010).

2.5 Opal Photonic Crystals

The opal term comes from the opal gem, which consists of regularly arrayed silica spheres in microscale. Thus, whatever it is produced, the structure consisting of regularly arranged spheres is called the opal structure. The first opal concept as photonic crystal was proposed in 1995 when Astratov et al. reported the use of silica opals. After this effort, other materials such as PS, PMMA and titania (TiO_2) have been studied as opal PC materials. Although other polymers, polymer composites and several oxide opals have been reported; PS, PMMA and SiO_2 materials are used commonly (Velez, 2010).

Broadly speaking, opals have a cubic structure with a face-centered cubic (FCC) lattice. Thanks to a slight difference in the energy of the colloidal spheres stacking in the FCC and hexagonal close-packed (HCP) structure, the FCC structure has a faint superiority over the HCP structure according to the Woodcock's calculations (Woodcock, 1997a, 1997b; L. Xu, 2004). However, other periodicities can be forced offering more possibilities if the growth process is directed with patterned substrates (Garcia, 2011; Khanh & Yoon, 2009; Sun et al., 2008; vanBlaaderen et al. 1997). The stacking order of the spheres is ABCABC for the FCC opal structure while ABABAB for the HCP opal structure (Fewster, 2016; Tauson et al., 1984). Yet, the volume fraction of both FCC and HCP structures is 74.05% (Whitworth, 1989). Moreover, it should be accounted that the filling fraction of spheres could slightly increase as the opals undergo a thermal treatment after assembly, which leads to the formation of small necks between the spheres. There are two type voids between the spheres in the

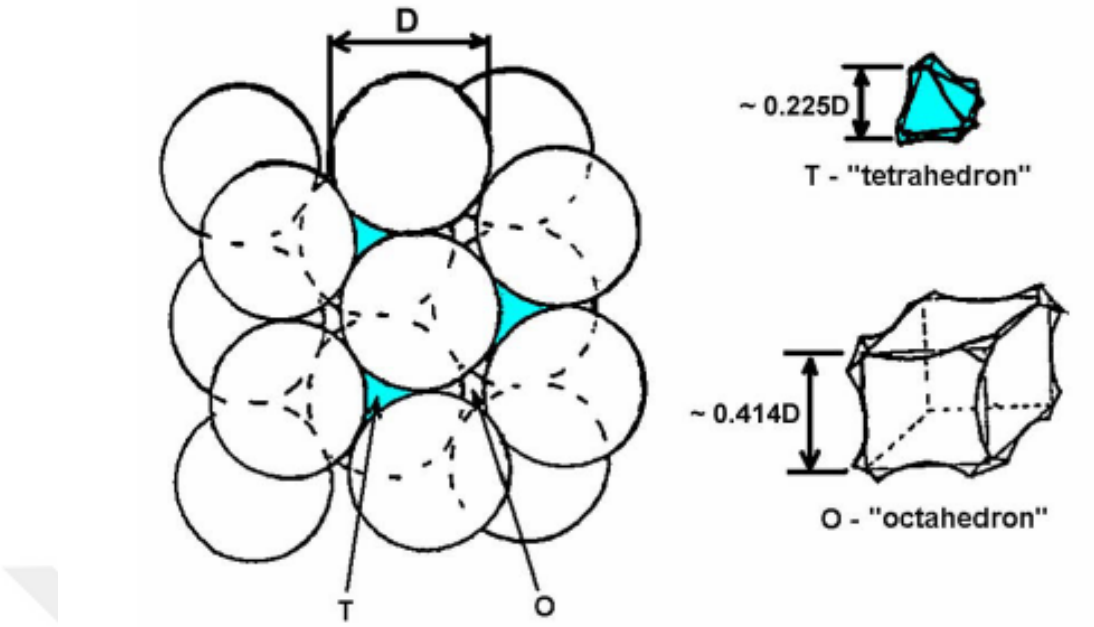

Figure 2.12 Schematic presentation opal and voids of FCC opal PC structure (Xu, 2004)

FCC opal structure namely octahedral void and tetrahedral void (Fewster, 2016; Tauson et al., 1984). These opal and void morphologies are given in Figure 2.12. The dimensions of the tetrahedral and octahedral interstices are about 0.225D and 0.414D in diameter respectively if the sphere diameter is "D". In addition, the dimension of the triangular void between three spheres contacted to each other is about 0.155D in the same conditions (Fewster, 2016; Xu, 2004).

Monodisperse polymeric or silica spherical building blocks can be synthesized by Stöber processes (Hartlen et al., 2008), dispersion polymerization (Tseng et al., 1986) and surfactant-free emulsion polymerization (Egen & Zentel, 2004). Any of these colloidal particles can be used to template inverse opal PCs. Among these technics, surfactant-free emulsion polymerization takes attention with simplicity (Phillips, 2016).

2.5.1 Colloidal Particles (Colloids)

Natural opals are valuable gems composed of a cubic close-packed arrangement of amorphous silica spheres and formed in a volcanic or a sedimentary environment. The

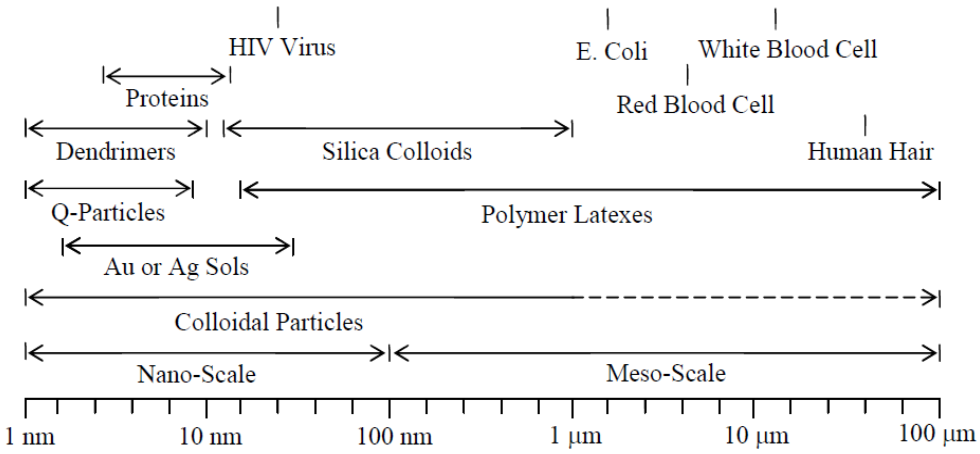

Figure 2.13 The list of some colloidal systems according to the their dimensions (Xu, 2004)

size range of these silica spheres are between 100-1000 nm and they also spheres have a narrow size distribution around 5%. The opal PC structures are formed from monodisperse colloids through one of the assembly methods. The presentation of the colloidal systems with a list of some structures according to the dimensions is given comparatively in Figure 2.13 (Xu, 2004)

Owing to the applicability of opal PCs in sensing or photonic band-gap materials, the study on the self-assembly of colloidal particles has been gathered great attention by many scientists. The phase (such as amorphous or crystalline solid) of the colloids can be influenced by slight modifications at the parameters of system pressure and temperature. Applications of the colloid particles are not only limited by scientific aims such as biological and chemical sensing (Horsch et al., 2006; van Kats et al., 2004); they are also used in our daily life interactions such as food, cosmetic products and household goods (Dinsmore et al., 2002; Hong et al., 2006). It is very important to figure out the properties of these particles and their applications because we have been interacting so much with these colloidal systems (Kim, 2011).

Colloidal photonic crystals are periodic structures, which reflect certain wavelength ranges and transmit others. That kind of structure exhibit coloration owing to the interference and diffraction of light. The color based on optical phenomena without

pigments is called structural color. Butterflies and other animals show a brilliant color by the same mechanism. A mixture of colloidal photonic crystals (synthetic opals) with polymer and carbon that are unusual materials for the pigment industry can be used for the structural colorization (novel pigment). Colloidal PCs can be considered as a pigment option complementing traditional organic and inorganic pigments due to easy fabrication although this colored powder does not show iridescent color (Velez, 2010).

Some toxic inorganic and organic unstable pigments (under UV radiation) have already used extensively. Therefore, the concept of stable structural color pigments without iridescence and toxicity sound great. Although opal structures and their optical properties have been studied intensively in order to fabricate new photonic materials, new application opportunities open for developing (Velez, 2010).

2.5.2 Self-Assembly of Colloidal Particles

The self-assembly method is one of the most popular approaches for the fabrication of 3-D photonic crystals, especially opal PCs. The natural tendency of monodisperse colloidal particles to self-assemble into ordered arrays is used in this technique (Sanders, 1985). Soon after the acknowledgment of artificial opals as photonic crystals for the first time in 1987 (Yablonovitch, 1987), the first opal PCs were characterized optically in terms of photonic band gaps (Astratov et al., 1995; López, 2005). This kind of structures have experimentally been shown a 3D PBG (Blanco et al., 2000). During the last years they have shown to be a good playground to understand light propagation in 3D PCs but also useful for specific applications as, for example, biomedical applications (Alexeev et al., 2004), solar cells (Guldin et al., 2010) and light emitting devices (LEDs) (Arsenault et al., 2007).

Self-assembly methods take superiority of the natural tendency of monodisperse colloidal particles for the production of ordered opal arrays under suitable conditions. Due to the fact that they were firstly studied as 3D PC in the middle of 1990 (Astratov et al., 1995), self-assembled 3D opal PCs have become one of the most widespread PC structures. The resulting structures are known as artificial opal (PCs) and consist of

mainly FCC arrays of polymeric or inorganic spheres. In addition, these artificial opal structures can be used for production of inverse opal structures obtained by infiltration with different materials within the lattice and subsequent removing of the original spheres. The obtained porous body makes them an appropriate structure to control their optical properties (Garcia, 2011).

Opal template production methods can be listed as sedimentation (Jin et al., 2016), vertical deposition (Fortes et al., 2011), centrifugation (Ma et al., 2013), dip-coating (Deleuze et al., 2011), spin-coating (Nandiyanto et al., 2011) and Langmuir-Blodgett (Reculusa & Ravaine, 2003).

2.5.2.1 Sedimentation

Self-assembly of colloidal particles is very popular nowadays owing to the high application potential such as sensing and photonic band-gap (Hosein & Liddell, 2007; Ngo et al., 2006). The action of colloidal particles could be inherently controlled by self-assembly. The action of the particles depends on the surrounding environment. Self-assembly of colloids is performed by the influence of gravity at the sedimentation method as denoted in Figure 2.14. The colloidal spheres in a dilute suspension are left to settle for long times, at a specific sedimentation rate. The rate of the sedimentation process is defined by the density difference between the solvent and the particles. The degree of the sedimentation rate defines how fast the particles will settle. Sedimentation can be seen as crystallization of colloidal particles in a wide array similar to arranging atoms in the angstrom scale (Leunissen et al., 2008; Shereda et al., 2008; Vermolen et al., 2009).

High-quality colloidal crystals could be obtained by this sedimentation technique according to the related studies (Deleuze et al., 2011; Ding et al., 2014). The sedimentation generally takes on the order of days to weeks to achieve long-range ordered colloidal crystalline structures that is a big problem for applicability. This limitation makes the sedimentation method disadvantageous for large-scale productions where the mass production is tight (Kim, 2011). Gravity sedimentation is

the simplest method and frequently preferred for colloidal assembly (Blanco et al., 2001; Mayoral et al., 1997). A dilute suspension (about 1 wt. %) containing colloids having a dispersion smaller than 5% is suitable for sedimentation driven by gravity as drawn in Figure 2.14. Thick opal structures can be produced with this sedimentation method. The thickness and order of the colloidal crystal can be adjusted by the several parameters such as the size and density of the colloidal spheres, as well as the rate of sedimentation.

If the size and density of these spheres are sufficiently high, the colloidal spheres can always settle completely to the bottom of the container. When both the deposition rate and the sphere size is too small, no sedimentation occurs in a reasonable time. However, if he sedimentation rate is too fast and the spheres are too large bad-quality assembly could be obtained (Xu, 2004).

On account of the high density of amorphous silica, monodisperse silica colloids are preferred most commonly for sedimentation. A main disadvantage of the sedimentation method is that it has very little control on the top surface morphology and the layer numbers of the three-dimensional crystalline arrays. Inasmuch as sedimentation by gravity is a very slow process, typically requiring sedimentation time expended from the weeks to the months, notably if sphere diameters are smaller than 300 nm (Xu, 2004).

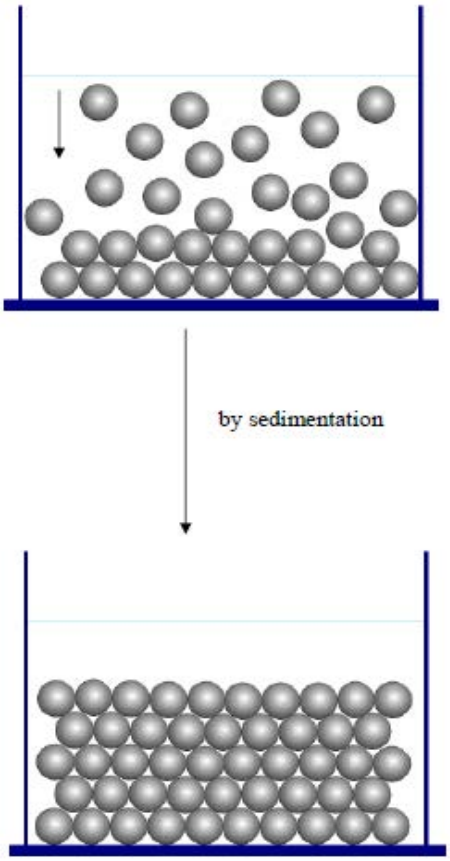

Figure 2.14 Illustration of self-assembly of colloids by sedimentation method (Xu, 2004)

2.5.2.2 Vertical Deposition

The vertical deposition has become one of the most popular methods for self-assembling opal photonic crystal production. Particularly if a thick sample such as opal structures is aimed, the vertical deposition method is highly suitable. This method has been extended for three-dimensional opal based PCs after first development for monolayers by Nagayama et al. (Garcia, 2011; Jiang et al., 1999).

The schematic diagram of the vertical deposition setup is illustrated in Figure 2.15. Owing to its simplicity, vertical deposition method has earned high interest. Vertical deposition conditions that will give good optical quality has been investigated for a long time by the researchers. Deposition on a tilted substrate with high crystalline quality has been obtained by oscillatory motion in the meniscus, high substrate

wettability low solvent surface tension and low ionic strength according to the related studies (Cademartiri et al., 2003; Cortalezzi et al., 2005; Kim, 2011; Teh et al., 2005).

Shorter process time is the main advantage of the vertical deposition comparing with the sedimentation method. The self-assembly at the air-liquid interface is a hydrodynamic phenomenon, and then a greater flow of solvent through the forming crystals may generate better crystal quality (Norris et al., 2004). The only limitation of vertical deposition method is that accessible structure options are limited (Kim, 2011).

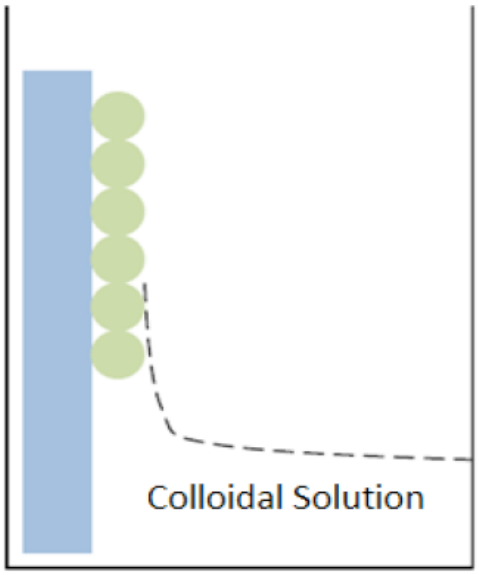

Figure 2.15 The schematic figure of the vertical deposition method

2.5.2.3 Spin Coating

Spin coating is a very convenient technique for the laboratory scale production of coatings because a very small volume of solution is used and an accurate control of the thickness can be achieved by controlling the precursor viscosity, spinning rate and time (Schwartz et al., 2004).

Quick speed-up is produced to obtain centrifugal forces after a colloidal solution is dispersed onto a substrate over a spin coating device. This acceleration causes ejection

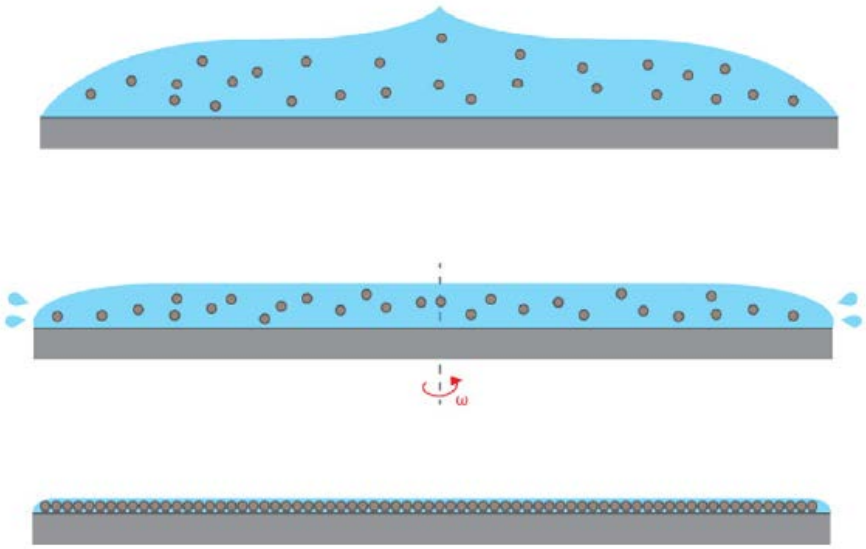

Figure 2.16 The schematic draw of the spin coating method (Dommelen et al., 2018)

the excess mass and ensures the thinning of the liquid film. The balance between adhesive and shear forces determines the minimum thickness of this continuing process. Depending on the used colloidal solution, ultra-thin films with the several tens of nanometers can be obtained (Dommelen et al., 2018; Hall et al., 1998). A schematic draw of the spin coating process is presented in Figure 2.16. Although spin coating is a promising technique for colloidal crystal formation, it has limitations with defect formations. These defects can be controlled by properly tuning parameters, such as rate, spinning speed and time (Dommelen et al., 2018).

2.5.2.4 Langmuir-Blodgett Method

Because of the simple synthetization by the Langmuir- Blodgett device, the formation of ordered monolayers has long been well understood (Tredgold, 1991). The working principle of the Langmuir- Blodgett method based on obtaining straight forward colloids on the surface with the help of surfactants, such as oil. The basic schematic view of the method and possible colloidal crystal morphology are given in Figure 2.17 (a) and (b) respectively. Yet, as long as they allow the formation of a monolayer at an interface, it can be applied to colloidal materials as well. The colloid spheres in the suspension form a spaced monolayer on the surface by spreading as far

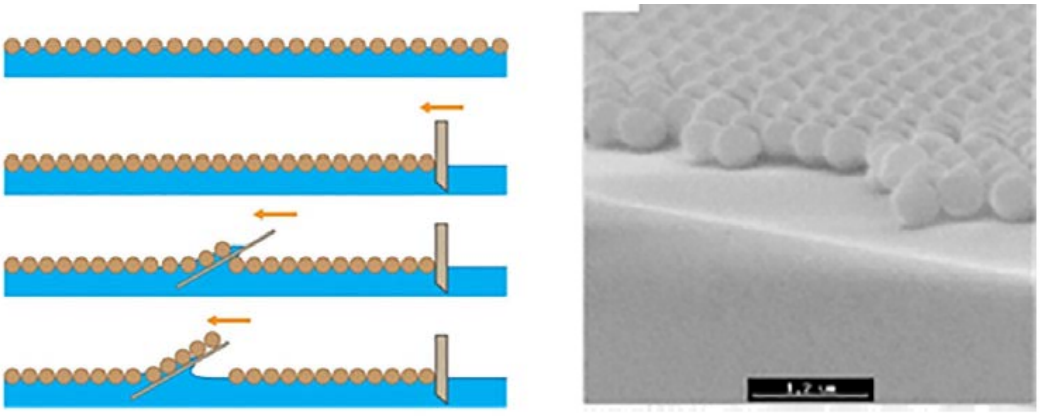

(a) (b)

Figure 2.17 (a) The schematic drawing of the Langmuir- Blodgett method and (b) SEM image of an monolayered colloidal crystal structure (Reculusa & Ravaine, 2003)

as possible when a colloidal suspension is dispersed onto a surface. Then the existing surface area is reduced by compressing through a barrier results in increased surface tension. Surface tension provided by the substrate is decreased during the extraction of the substrate from this compressed film and that causes transfer colloids to the interface (Dommelen et al., 2018).

Due to the nature of this event, hydrophilicity of the substrate is a very critical parameter for self-assembly with the Langmuir-Blodgett method. This method has some limitations in terms of functionalization and the particle size of the colloids. Furthermore, it is possible for Langmuir based processes that some crystal defects can be observed due to capillary forces. Scooping the substrate or evaporating the water result in particles adhering to the walls, which give rise to the formation of stresses in the colloidal crystal.

2.6 Inverse Opal Photonic Crystals

Inverse opals originate with spherical colloidal particle building blocks that are generally produced in the scale of 100 nm to several microns. The hexagonal or cubic close-packed hydrated form of silica is called as "opal". Simple materials that do not have any special properties can be used for this sacrifice opal structure. Opal PC

structures could be reproduce easily to opals with nano-beads of polymethylmethacrylate (PMMA), polystyrene (PS) or even silica by self-assembly method (Subramanian et al., 1999). Self-assembly can be basically used owing to the energetically favored face centered cubic (FCC) close-packing form of spheres. Therefore, the voids between the spheres can be filled easily by a metal oxide and removed these sacrificial sphere beads. The inverse opal PCs are obtained by removing the original beads from the composite structure (Lebrun, 2014).

Inverse opal structures consist of regularly spaced walls of metal oxide between adjacent pockets of air or water similar to a honeycomb morphology. Air has a very low refractive index value of 1 while water has 1.33. In order to accomplish a complete PBG, it is important to use a metal oxide material characteristically with a refractive index higher than 2 (Lebrun, 2014). If the refractive index of the spheres relatively low the optical performances of artificial opals is limited owing to the ratio of the refractive index value of available sphere materials. Because of the fact that the refractive index of the microsphere material should be at least 2 or higher to have a cPBG, it is not possible to reach a cPBG in FCC arrays at opal PCs (Busch & John, 1998). This PBG differences for opal and inverse opal structures are indicated in Figure 2.18. As can be seen it is high possibility to obtain cPBG at the inverse opal PC structure rather that opal PC structure due to high refractive index possibility.

Inverse opal PC structures have many distinctive properties. Especially, their high degree of order makes them enable for optical applications, high surface area and their interconnected porosity are necessary for enabling fluidic applications. Inverse opal PCs have bright, iridescent color that comes from their structure due to periodicity on the scale of the visible light wavelength (von Freymann et al., 2013). Inverse opal PC materials can be used for improved control over the light flow in addition to the color formation. Porous materials such as inverse opal PC materials show attractive transport phenomena owing to the restricted motion of fluids within micro- to nanoscale pores, with the size, shape, and connectivity of the pores playing a large role in the overall wetting pattern. Regular and interconnected pore structure could be used in many applications as itself. And also they can be used as a model system for studying the

behavior of fluids within confinement (Cherdhirankorn et al., 2010; Raccis et al., 2011).

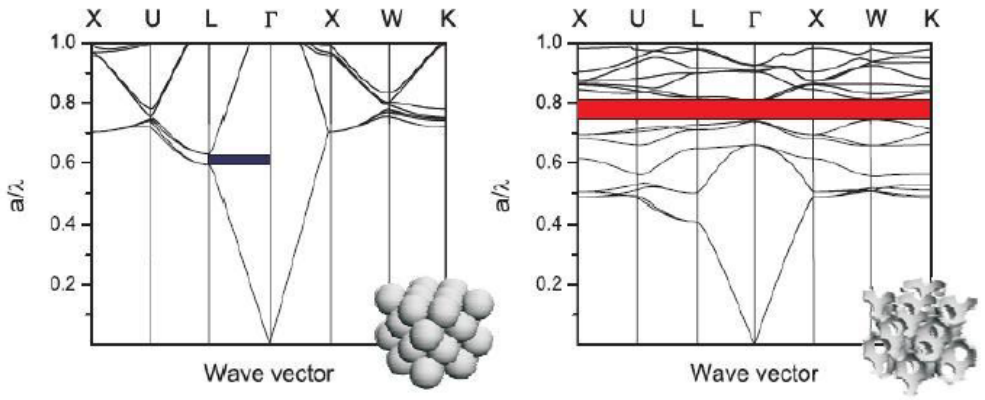

(a) (b)

Figure 2.18 Dispersion diagrams with schematically presentations of (a) opal and (b) inverse opal silica PCs (Velez, 2010)

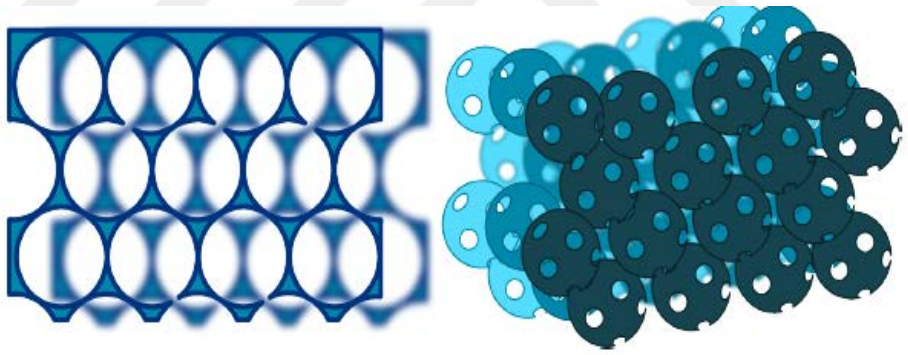

(a) (b)

Figure 2.19 Schematic illustration of inverse opal structure from (a) top and (b) side view (Lebrun, 2014)

Chemical functionality can be adjusted in the ordered structure by changing the composition into inverse opal structures can be used in catalysis, sensing and electrode applications (Phillips, 2016; Phillips et al., 2016). One can control the optical and wetting properties of inverse opal PCs by controlling their morphology, structure, and composition. Highly uniform structures are needed for consistent properties. In fact, crack-free ordered porous structures are intended to obtain while they can be a

necessity to attain certain features. Inverse opal PC materials could be used for many different applications by controlling their properties such as composition and shape (Phillips, 2016).

Inverse opal PCs are artificial structures that are fabricated usually by self-assembly or mechanically, depending on the size of their periodicity (Lopez, 2003). A schematic draw of an inverse opal structure is given in Figure 2.19. Inverse opal PC structures are important due to high possibility of achieving cPBG. Three factors define the PBG of a photonic crystal; first one is the crystal symmetry, second is the lattice constant (spatial period of the modulation) and the last one is the refractive index contrast between diffracting elements and its surroundings (Velez, 2010).

The porous and ordered structure gives to the inverse opal PC many properties. Thus, the properties of the inverse opal PC can be controlled by controlling the underlying structure that is critical for using inverse opals in most application areas. The illustration of some inverse opal application areas such as optic, wetting and sensing are given in Figure 2.20. Although inverse opals are well-suited for many times, different applications have different structural and material requirements, of them (Phillips, 2016).

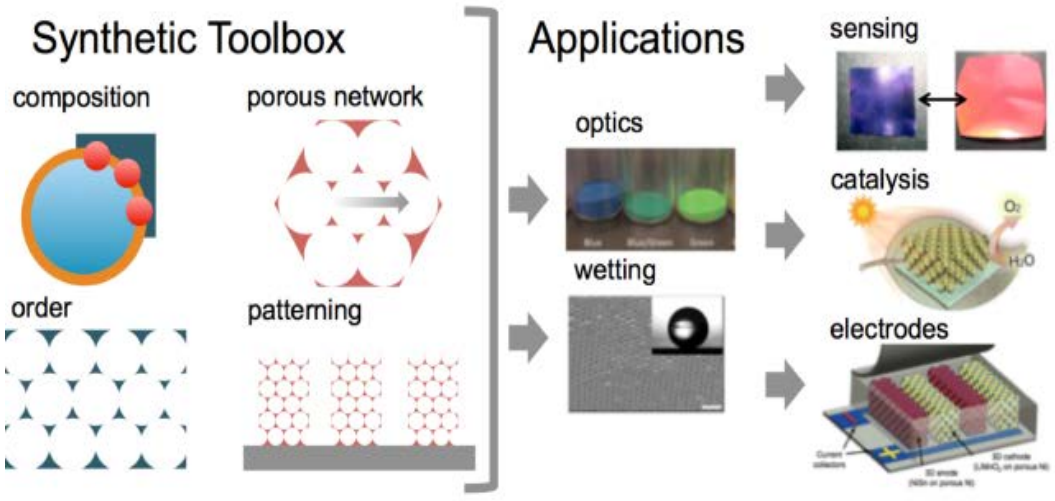

Figure 2.20 Inverse opal application areas with synthetic strategies (Phillips, 2016)

In order to obtain three-dimensional structures for photonic purposes bottom-up (chemical approaches) have been used generally. One of the most important architectures of 3-D PCs is based on natural opal gemstones. Colloidal assembly is the easiest one among the different methods for fabricating 3-D photonic crystal materials. Accessibility for any chemistry laboratory is one of the great advantages of synthetic opal structures. Colloidal techniques for photonic crystals require two steps. Firstly, synthesis of spheres should be carried out and then the mechanism of assembling or crystallization should be done (Velez, 2010). The structure of the opal PCs can be inverted. A high refractive indexed material can fill the void volume over opal spheres and the opal structure and could be then removed by etching or burning processes. The obtained negative of the opal structure is the inverse opal PC (Couturier, 2016).

Inverse opals behave as PCs and have their optical properties as long as the morphology and a sufficient refractive index contrast between the filled and the void volume. Moreover, inverse opals can be seen as porous membrane materials due to connected voids morphology. In this respect, the optical properties of PCs and the high specific surface are combined in the inverse opal PC structure that endorses infiltration and diffusion of the medium such as gas or liquid through the PC porous body (Couturier, 2016).

2.6.1 Optics of inverse opals

Due to the fact that inverse opal PCs have three-dimensional periodicity, coherent reflections can occur in any direction. As described before, the primary color of an inverse opal originates from Bragg reflection. The location of the Bragg peak can be calculated from a variation of the standard Bragg-Snell equation (3), considering the inverse opal geometry. It is provided here for a 3-D inverse opal PC structure comprised of a close-packed (111) lattice:

$$n\lambda = \sqrt{\frac{8}{3}} d \sqrt{n_{eff}^2 - sin^2\theta} \tag{2.5}$$

where n is an integer (n=1,2,3...), d the distance between planes, n_{eff} is the average refractive index of the PC structure and θ is the incident angle between the normal axis of the material. Thus, these parameters can be adjusted to control the location of the Bragg peak, and they provide synthetic handles that can be used to tune the optical properties of inverse opals. The qualitative effect of changes to d, n, and θ are the same as those described above for 1-D photonic crystals (Phillips, 2016).

The Bragg peak is often called a photonic bandgap in analogy to electronic bandgaps in semiconductors; yet, it is not typically a true band gap. With better order over long ranges and higher RI materials, a full photonic band gap is possible (Ding et al., 2014). Wavelengths near even a partial stop band will still interact strongly with the structure. Indeed, wavelengths at the band edge experience the "slow photon effect," where their group velocity is decreased within the structure (Johnson et al., 2001). This effect can have implications in a number of areas, as these wavelengths have longer lifetimes within the structure, which can lead to enhanced absorption (Phillips, 2016).

2.6.2 Production of Inverse Opal Photonic Crystals

Inverse opals are generally produced by firstly assembling the colloids into an ordered, namely direct opal template, then backfilling this template with the desired material before removing the sacrificial template. Even though the colloidal sphere identity is not critical, they must be monodispersed. Generally, the colloids assemble by a convective assembly process in which the colloidal particles are deposited from an aqueous dispersion via a receding meniscus as discussed in detail above (Dimitrov & Nagayama, 1996; Malaquin et al., 2007; Phillips, 2016).

Generating crack-free, homogenous inverse opal PCs improves their applicability. Cracks can lead to non-uniformities in the pore structure that can disrupt the optical signal due to scattering off the crack or local variations in the periodicity. Moreover, they can affect the porosity due to the crack itself or the distortion of the pores near the crack. With a uniform, crack-free structure, inverse opals have a consistent optical

signal, potentially enabling additional photonic and lasing applications. High-quality structures can also be used as a model to better study how these macro-pores affect the performance of filters, catalysts and electrodes. In addition, a uniform pore structure makes enable sharp transitions for liquid sensors (Phillips, 2016). In order to adjust their properties and tune their spectral features, a number of parameters can be acted such as the symmetry, the dimensionality, the topology, the effective refractive index and the lattice parameter (Espinha, 2015).

The pre-formed colloidal crystal template can then be back filled by sol-gel precursors, inorganic complexes or nanoparticles, usually either by infiltration, drop casting, dip-coating, spin coating, atomic layer deposition (ALD), or electrodeposition (von Freymann et al., 2013). Backfilling allows for a variety of compositions to be made relatively easily. However, the structure is limited to domains of less than 10-100 μm (Phillips et al., 2016).

2.6.3 Infiltration Methods

Three-dimensional nanoscale mesh or inverse opal porous structure can be fabricated by infiltrating materials into the voids between the colloidal spheres in opal template. Later, the opal template is extracted from the body by HF solution for silica-based opals, or organic solvents such as dichloromethane, toluene, and acetone and calcination for polymer-based opals. A range of methods has been used to produce inverse opals since the late 1990s. Sol-gel hydrolysis, electrodeposition, chemical polymerization, atomic layer deposition (ALD), and chemical vapor deposition (CVD) techniques are the most popular ones (Xu, 2004).

Dielectric materials such as silicon, germanium, zinc oxide, titania, and even diamond can be infiltrated into colloidal crystal spheres successfully by the CVD and ALD approaches (Juarez et al., 2005; King et al., 2005; Vlasov et al., 2001; Zakhidov et al., 1998). But, the material does not completely fill the whole voids in the opal structure owing to the conformal growth pattern. In addition to dielectric materials, metals also can be produced by the infilling sol-gel method (Denny et al., 2007; Zhang

et al., 2002). Yet, the shrinkage phenomenon should be under considering during the drying process or heat treatment in the sol-gel methods (Kim, 2011).

2.6.3.1 Electrodeposition

In order to prepare working opal template electrodes, firstly, a layer of metal like copper is deposited on one-side of opal pieces or opals are deposited on conducting substrates like ITO (indium tin oxide) glass. Then, the obtained opal template electrodes are placed in plating solutions versus a counter electrode like Platinum (Pt) wire, and materials grow inside voids of opals potentiostatically or galvanostatically. A variety of inverse opal PC structures based on metal, semiconductor, and conductive polymer have been produced by electrodeposition method (Braun & Wiltzius, 1999; Cassagneau & Caruso, 2002; Wijnhoven et al., 2000). Electrodeposition is an effective method for producing the inverse opals, due to the nearly complete filling of the channels of opal templates and easy control of the extent of materials growth (Xu et al., 2003; Xu, 2004).

2.6.3.2 Sol-Gel

The sol-gel method that is a wet chemical technique uses either a chemical solution or colloidal particle for producing integrated network (gel). The sol is a distribution of colloidal particles in a liquid medium while a gel is an interconnected, rigid network with pores of sub-micrometer dimensions and polymeric chains whose average length is greater than a micrometer (Hench & West, 1990). Schematic representation of the sol-gel process is presented in Figure 2.21. Typical precursors are metal alkoxides, metal chlorides and metal nitrates for sol-gel process. General steps of the sol-gel process can be listed as hydrolysis and condensation of precursors, followed by gelation, drying and sintering. Sol-gel precursors react chemically with the surrounding area where solvents and other agents present (Pierre, 2013).

The hydrolysis phenomenon happens with the deprotonation of a dissolved metal (M) cation. Water molecules around M lead a loss of proton during this process

$$M(OR)_4 + H_2O \rightarrow HO{-}M(OR)_3 + ROH \quad (2.6)$$

In this step, the observed ROH is an alcohol group. As can be seen below, the hydrolysis reaction is completed and all OR groups are converted to OH groups, depending on the amount of water and catalyst:

$$M(OR)_4 + 4H_2O \rightarrow HO{-}M(OH)_4 + 4ROH \quad (2.7)$$

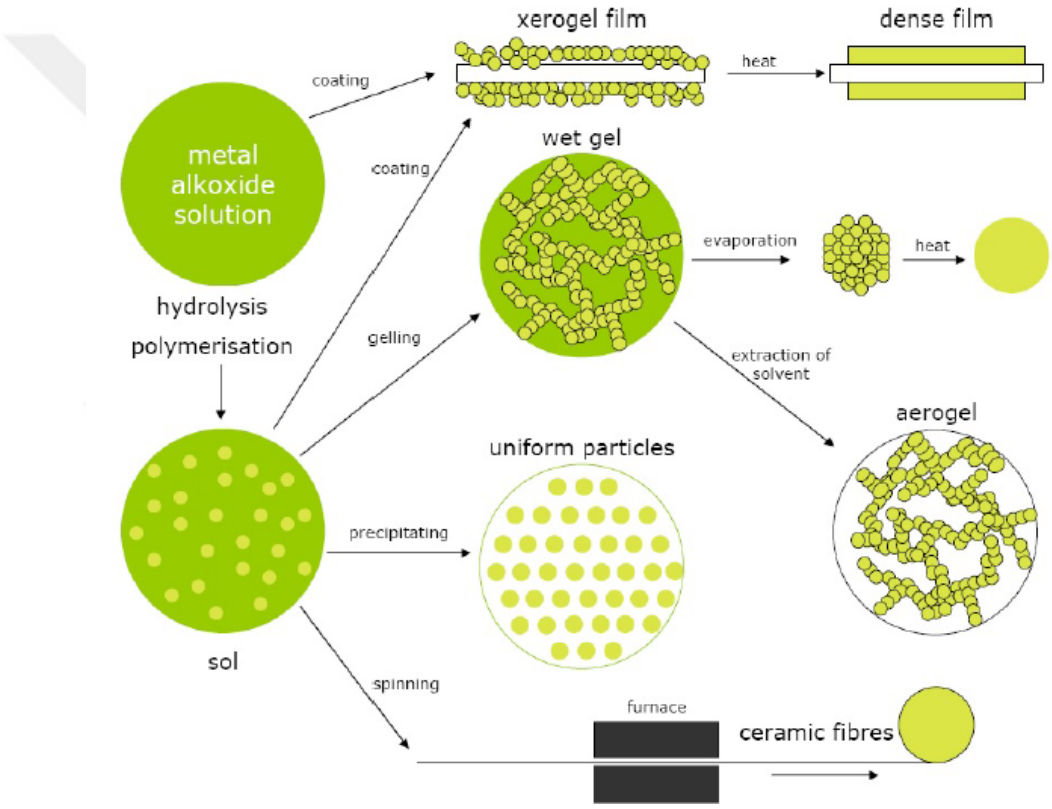

Figure 2.21 Schematic representation of the sol-gel process for varied nanomaterials (Pierre, 2013)

Condensation reactions take place after the hydrolysis reactions in order to form the olynuclear complex between the two metal atoms. Either olation or oxolation reactions take place during the condensation in aqueous solutions. The reaction rates should be controlled according to the available oxygen amount. Sometimes an argon atmosphere can be preferred for this aim (Pierre, 2013). In the olation process, transfer of the H to an OR ligand performed according to the reaction below:

$$2M(OR)_{x-1}(OH)\ M_2O(OR)_{2X-3}OH + ROH \quad (2.8)$$

In the oxolation case, transfer of the H to an OH group;

$$2M(OR)_{x-1}(OH)\ M_2O(OR)_{2X-3}+H_2O\ \text{(Condensation)} \quad (2.9)$$

A three-dimensional network structure takes place after the hydrolysis and condensation reactions. Afterwards a solid phase is obtained. The reaction rates increase with temperature. In addition, the hydrolysis and condensation reactions are affected strongly by pH value. Thus, various structures of a material could be produced (Pierre, 2013).

The transformation of a solution or sol into a gel is termed as gelation. Many links form between the sol particles or solution molecules in the gelation step, in order to form a 3-dimensional solid network. Clusters grow to bound together in order to form a gel after the hydrolysis and condensation reactions.

The sintering step is actually a thermal treatment where the densification occurs. Atomic mobility increases with increasing heat, thus accelerating diffusion. With the increasing heat, the physical and chemical water in the structure moves away from the body. This removal causes the formation of pores in the structure. In the sintering process, these pores are closed and the body becomes bulk. Furthermore, one of the most important results of sintering process is that the desired phase is obtained (Yıldırım, 2017).

Sol-gel solutions containing alkoxide precursors are infiltrated into the voids of the opal structure. The precursors related to aimed material are penetrated into the voids of colloidal spheres by the capillary force. Then the obtained composite structures including opals and alkoxide precursors left for hydrolysis reactions and then drying. In order to provide the voids of opals be sufficiently filled by the material, the steps of the penetration, hydrolysis reaction and drying process can be repeated for many times. A wide range of inverse opal PCs have been produced successfully as metal oxides

such as SiO_2, ZrO_2, GeO_2, Al_2O_3, TiO_2, SnO_2, Eu_2O_3, Nd_2O_3, and Sm_2O_3; binary oxides such as $BaTiO_3$ and $PbTiO_3$; and multinary oxides such as $(Pb,La)(Zr,Ti)O_3$ by the sol-gel production method (Xu, 2004).

2.6.3.3 Chemical Polymerization

After opal structures are filled with a liquid monomer containing a small amount of initiator polymerization is carried out by ultraviolet (UV) illumination or heating. This method is suitable polymer-based materials. Polyurethane, polydivinylbenzene (PDVB), polyethylene glycol di-methacrylate (PEDMA), polyacrylate methacrylate (PAM), poly-methyl methacrylate (PMMA), polystyrene (PS), poly p-phenylenevinylene (PPV), and epoxy resin based high-quality polymer inverse opal PCs can be produced by the chemical polymerization method (Gates et al., 1999; Johnson et al., 1999; Palacios-Lidon et al., 2002; Park & Xia, 1998; Xu et al., 2003; Xu, 2004).

2.6.3.4 Chemical Vapor Deposition

Opals are filled by the gaseous precursors and then deposition is applied by thermal treatment. Dense inverse opal structures can be produced by this technique by penetrating the pore network of colloidal crystals due to the penetration ability of gaseous precursor. The chemical vapor deposition method has been used productions of carbon, SnS_2, Pt, Pt-Pd alloy moreover Si and Ge inverse opal PCs which are technologically important (Xu, 2004). Other inverse opal approaches can be listed as electroless deposition (metals), salt-precipitation and chemical conversion (metal oxides and Sb_2S_3), nanoparticle infiltration (metals, CdS, SiO_2 and TiO_2), melt infiltration (low melting-point metals, semi-metals, and alloys), polymerization and pyrolysis (carbon), oxidation or reduction (NiO, metals, alloys and Ge), electrophoresis (SiO_2 and TiO_2), spraying (metals and Si),adsorption and chemical conversion (metals, $Sr_{0.5}Sm_{0.5}CoO_3$), solvo-thermal synthesis (CdS) (Xu, 2004).

2.6.4 Sintering

The sintering process is an important step that endorses the opals to have mechanical stability and connects every colloid with its neighbors. This final stage provides connectivity between particles allow formation of inverse opal structure. If the opal template consists of polymer-based materials, it burns off from the structure and only inverse opal morphology is maintained. Sintering time and temperature determines the pore size and maximum gap with of the inverse opal (Kim, 2011).

2.7 Applications

Inverse opal PCs can be used in a variety of applications with their unique properties. Especially, inverse opal PCs can be designed for interacting strongly with visible light, due to adjustable periodicity in the length scale of the visible light wavelength. So they can be used at optical applications such as light-emitting diodes, solar cells and structural color-based coatings. Moreover, interconnected porosity and high surface area properties of inverse opal structure allow them used wetting and fluidic applications such as scaffolds for tissue engineering, sensors of liquid media, materials for studying confined diffusion processes and substrates for omniphobic surfaces. Their optical and wetting properties can be combined with chemical functionality to create catalysts, sensors, and electrodes.

Inverse opal PCs are functional materials that have a very narrow distribution of pore sizes, present a high degree of interconnected porosity. For that reason, they have impact on areas as distinct as tissue engineering where they can play the role of scaffolds for cell growth, sensing for pH measurement or chemical species detection, catalysis where the presence of photonic bandgaps may enhance photocatalytic activity, energy for the fabrication of electrodes with application in lithium ion batteries and, certainly, in photonics (Espinha, 2015).

Applications of inverse opal PCs can be listed for further explanations such as photonic, magnetic, separation, catalysis, structural color, optical applications, wetting

and fluidics, sensing, electrode. Some information about these applications will be given below.

2.7.1 Photonic

Si and Ge based materials, whose refractive index are 3.8 and 4.1 respectively, can be produced as inverse opal PCs in order to obtain high dielectric contrast. That kind of inverse opal materials has been produced successfully with the property of complete photonic bandgap in near-IR region. Thus, inverse opal PC materials can be applied in the photonic field as micro cavity lasers, waveguides, optical chips and dielectric mirrors etc. (Xu, 2004).

2.7.2 Magnetic

Colloidal template synthesis provides a low-cost procedure to obtain patterned magnetic media in nanoscale. Because of their periodic nanoscale, structures three-dimensional magnetic metal based such as Fe, Co, Ni, Ni50Fe50 alloy opal or inverse opal PCs have significantly enhanced coercively comparing to the related bulk materials. In addition, because of the exchange coupling of ferromagnetic and antiferromagnetic films across their common interface, it is found that Co-CoO inverse opals indicate exciting exchanging bias phenomena, such as the shift of the ferromagnetic hysteresis loop along the field axis (Xu, 2004).

2.7.3 Separation

Based on the original opal templates, the inverse opal PCs have a range of pore sizes from a few nanometer to a micrometer scale. Because of the homogeneity and connection of the close-packed pores, inverse opal PC structures can be used in filtration immobilization, and separation applications. The adjustability of the pore diameters of inverse opals increases their usage in separation processes (Xu, 2004).

2.7.4 Structural colors

The color is a result of pigmentation in natural or man-made materials. This means that, in general, colored media absorb and therefore subtract, some regions of the white light spectrum shining upon them. Even so, this is not the only known color mechanism. Interestingly, some butterfly wings or bird feathers, which are consist of non-absorbing materials like chitin or keratin, exhibit brilliant colors that are instead owing to their nano and microstructures. This mechanism is named as structural color and has been extensively studied in the last decades and reported in a wide list of new artificially produced materials. Structured non-absorbing dielectric materials have been explored for fabricating optical components able to confine, reflect or guide light in novel ways (Espinha, 2015).

Once the incident light interacts with physical structures in spatial variations with a comparable to the wavelength of light structural colors are observed by the selective reflection of the incident light. Structural color can be observed at diffraction gratings similar to a CD surface, multiple interferences in multilayer dielectric filters, polarization inside birefringent materials such as calcite, thin-film interference like in soap bubbles and of course, photonic crystals (Velez, 2010).

Iridescence itself has been applied to the pigments. The effect is achieved by tiny flakes of mica and alumina, which interfere with an incident white light that produces colorful sparks with this kind of pigment. Several arrays can be used to create different pigments with this effect. The refractive index contrast of the media is the key to the relationship between color and optical effects. For instance, white color is the result of scattering elements inside other media; chromatic dispersion is an effect of refractive index as a function of wavelength and wavelength filters use a stack of dielectrics in order to reject certain colors.

Structural color interest has arisen by scientists for centuries. Such a coloration involves selective reflectance of incident light provoked by the structure of a particular object in contrast to classical pigment or dye-based colors. Dye-based colors benefit

from the energetically consumption of selective wavelengths. Examples of structural color have been present in the nature since long, resulting from millions of years of evolution (Galisteo-Lopez et al., 2011; Phillips, 2016). Probably the most beautiful application example of structural color is in biological systems. The active mechanism is generally multiple layered structures (1-D PC structures) consist of chitin, keratin, and calcium carbonate and so on. Usually, a dark layer of melanin is located to the back sheets, intensifies the color by absorbing the non-reflected light. Colors in several living creatures such as fishes, beetles, butterflies, birds, moths, peacocks shells, even in some plants have been intensely studied (Velez, 2010). Iridescence phenomena exemplified by the dorsal wings of Morpho butterfly given in Figure 2.22. It is revealed to be one of his characteristics to survive to predator birds, to mark is a territory or even to arise the attention of the other sex (Couturier, 2016; Kinoshita et al., 2008).

Their lamellar architecture produces periodic domains with distinct dielectric constants, which create the Bragg diffracted wavelength. The periodical refractive index contrast between the lamellar material and the surrounding media (here: air) leads to interferences that provoke the disappearance of the non-coherent wavelengths and the reflection of the coherent color. The observed reflected color depends on the lamellar structure and the refractive index contrast (Couturier, 2016).

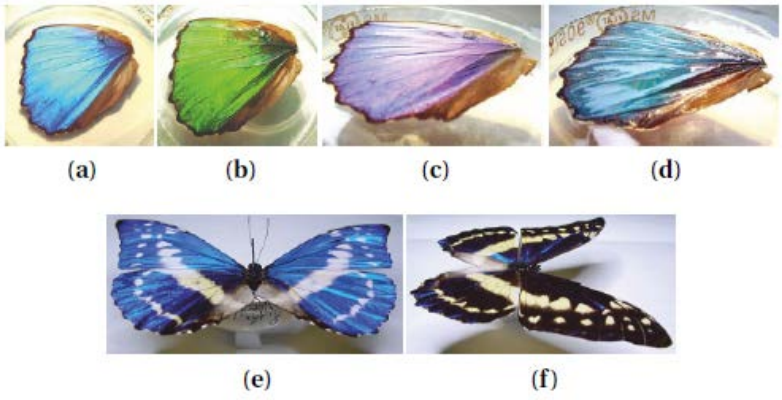

Figure 2.22 Front and oblique views of the Morpho didius wings in (a-b) air and (b-c) ethanol media respectively; (e) perpendicular and (f) the parallel view of Morpho cypris wings (Kinoshita et al., 2008)

2.7.5 Optical application

The structure of inverse opals makes them suitable for optics, where exact control over periodicity is critical to function and performance. In addition, real-world optical applications of inverse opal PCs include color elements for display technologies or decoration, lasers, anti-reflective coatings as well as optical fibers. These applications require precise control over the optical properties, and therefore of the structure. Actually, inverse opal PCs are used in this area definitely, because the modular fabrication process provides fine control over the optical properties (Phillips, 2016).

2.7.6 Wetting and fluidic applications

Controlling gas and liquid flow through inverse opal pores is important for controlling transport and diffusion for cell culture, drug delivery, membrane, and filter applications. Similarly, diffusion over all the pores of the inverse opal structure is obligatory for electrode and catalytic applications. Inverse opals have been used for fundamental studies of diffusion in confinement even when not used directly in the application. Liquid filling of the inverse opal pores themselves has been studied in addition to gas flow within the structure.

Due to the re-entrant geometry at the necks connecting inverse opal pores, liquids can be pinned without entering an adjacent pore. The inverse opals obtained from the co-assemble method, the long-range order provides a uniform pore structure across through the sample. This uniform pore structure has allow interesting liquid sensing applications, where liquid filling of the pores results in a color change. The underlying uniformity enables a sharp cutoff for if liquids fill the pores or not (Phillips, 2016).

2.7.7 Sensing

The periodicity and porosity of inverse opals are both utilized in sensing applications. The request for inexpensive, simple and reliable sensors comes from the necessity of monitor and record a broad range of conditions and analyses such as pressure, pH, temperature, humidity, and light intensity. In addition, there is a big demand for measuring the presence of various chemicals and microorganisms in vivo, water, and food. A number of studies on inverse opal PC sensors are concentrated on diverse aspects such as specific application areas, degree of order, fabrication, and materials (Phillips, 2016).

As given in Figure 2.23, dynamic variation of the lattice constants, the refractive index of constituent materials, and the spectral characteristics of additional incorporated components can result in a distinct optical response. When the lattice constant is increased, a redshift is observed in the stopband (Figure 2.23 (b)-i), while if the refractive index contrast is decreased a decrease in the intensity of the reflectance and a red shift in the peak is observed (Figure 2.23 (b)-ii). Furthermore, the saturation of the observed color could be improved by the incorporation of the absorbing material (Figure 2.23 (b)-iii) (Phillips, 2016).

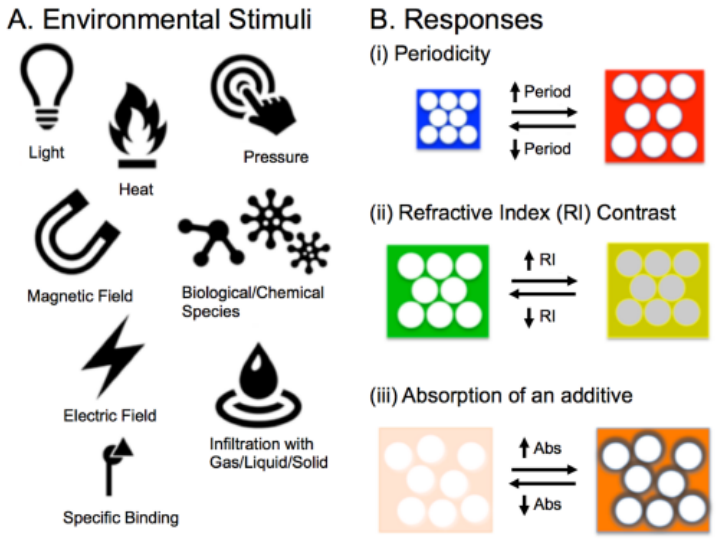

Figure 2.23 (a) Sensing parameters of inverse opal based PCs and (b) their response mechanisms for color changes (Phillips, 2016)

The controlling ability of these various responses by structural hierarchy, composition, and surface chemistry makes inverse opal PC materials beneficial for sensing applications. Due to their flexibility and modularity of design, inverse opal sensors have a very special advantage that allows combinations of various architectures, the degrees of order, surface chemistries, and structural materials with suitable fabrication methods (Phillips, 2016).

2.7.8 Catalysis

Inverse opal PC materials take advantage of the high surface areas open porous structures and material composition control in the field of catalysis applications. Catalytic activity is improved by the high surface area while the large enough pores give rise to rapid mass transport. Modification of the surfaces of the pore walls, doping and the produce of silica inverse opal structures with zeolitic micro or mesoporous frameworks are the promising possibilities to increase catalytic efficiency (L. Xu, 2004). Additionally, activity, selectivity, and stability of the resulting catalyst can be improved by adjusting the composition and combine functional materials with inverse opals which are generally called three-dimensionally ordered macro-pores in this field.

The scientists have spent much effort on inverse opal PC structures for high catalytic performance, during the last decade. Inverse opal PC catalysts have been applied for eco-friendly applications such as elimination and degradation of volatile organic compounds emitted from industrial activities and transportation, carbon monoxide, and un-combusted hydrocarbons. Further, catalytic and photocatalytic processes that have been investigated including reduction or oxidation of automotive and industrial harmful products, synthesis of chemical fuels (e.g. by the water splitting), and lastly upgrading of biomass. Some modified metals and metal oxides have been applied for this catalytic reaction (Phillips, 2016).

Additionally, owing to their photonic nature inverse opal PCs are used for photocatalysis. Photonic properties can lead to enhanced light absorption, which inverse opals combine with the benefits of their porosity. Hence, many studies have

been carried out on the photocatalysis of inverse opals in the past few years. Highly efficient and more purpose-designed catalysts could be obtained from inverse opal structures by controlling the composition and morphology. The crack-free morphology and ordered domains over notable large areas are very crucial for photocatalytic applications while long-range order is less important for high catalytic performance, for some catalytic applications (unlike optical applications) (Phillips, 2016).

2.7.9 Electrodes

Electrochemical processes are important for energy storage and conversion, for example solar cells, batteries, fuel cells, and capacitors. The geometry of an electrode has a high effect on capacities and rates because the electrochemical reactions take place at the interface of an electrolyte and an electrode. The composition and geometry of inverse opal PCs can be controlled through multiple length scales, and thus this makes inverse opal materials a powerful candidate for various electrode applications. The existence of macrospores is beneficial for faster diffusion; with inverse opals, both length scales can be precisely tailored while the morphology of the inverse opal structures could be controlled on the 10 nm scale (Phillips, 2016).

The interconnected porosity, visible light control and high surface area are the important advantages of inverse opal PCs for the electrode applications. It is possible that, short charge transport distances and high charging rates can maintained in capacitors by high surface area. The surface area of the inverse opal structures can be further increased with mesoporous morphology by using block copolymers. Inverse opal structure with ordered spherical porosity ensures fully interconnected ion diffusion and diffusion controllability and a good model system to study.

CHAPTER THREE
EXPERIMENTAL PROCEDURE

3.1 Literature Review

So many studies on inverse opal and inverse opal PC materials have been carried out since its discovery. The excess of the predicted contributions to technology has made inverse opal studies very popular. Examples of studies about the related subject can be summarized as follows.

Up-conversion luminescence is a potential application where photonic crystals are studied intensively (Chai et al., 2018; Yang et al., 2013; Zhang et al., 2018; Zhu et al., 2018). Yang et. al studied infrared to visible up conversion luminescence of Er^{3+}/Yb^{3+} co-doped CeO_2 inverse opal with verified microsphere sizes of the opal template (Yang et al., 2013). They expressed that the red and green up converted emissions were obtained in both the reference sample and inverse opal samples under a 980 nm diode laser excitation. Due to the photonic band gap effect, the red up converted emission intensity decreased in the spectral regions of the photonic band gap (Yang et al., 2013). In addition, Niu et al. obtained more than 30-fold increase in luminescent emission via coupling a 3D opal PC with fluoride up conversion nanoparticles. They thought that this improvement is about the high absorption and extraction, obtained by the 3D PC structure (Niu et al., 2014).

Due to the increased surface areas macro porosity and shortening diffusion length, the inverse opal PC materials can be used in battery applications as anode materials (Armstrong & O'Dwyer, 2015). Lee et al. claim that they obtained a significant improvement over carbon inverse opal materials using a PMMA sphere template and resorcinol formaldehyde (RF) polymer precursor (Lee et al., 2005). Most recently, because of their ability to piece together electrolytes and reduce diffusion limitations, PCs have earned great consideration as Li-ion battery electrodes (Armstrong & O'Dwyer, 2015). To illustrate this, Doherty et al. studied different pore size and calcination temperature effects on the performance of $LiFePO_4$ inverse opal batteries.

They found that higher pore size provided consistently higher discharge capacities than samples consist of smaller pore diameters (Doherty et al., 2009).

It was mentioned that because of the reduced total internal reflection of the diode surface PCs have a considerable effect on enhanced light extraction efficiency of LEDs (light-emitting diodes) (Suslik et al., 2017). As an example, Nelson et al. produced a new generation led material using a group of III–V semiconductor materials in 3-D inverse opal PC nanostructures. A 3-D PC LED (illustrated in Figure 3.1) was fabricated by incorporating an InGaAs based passivation layer between C doped and Si-doped GaAs inverse opal cladding layer by the group. They claimed that this hetero-structured PC LED showed electrically driven emission at increased drive currents (Nelson et al., 2011).

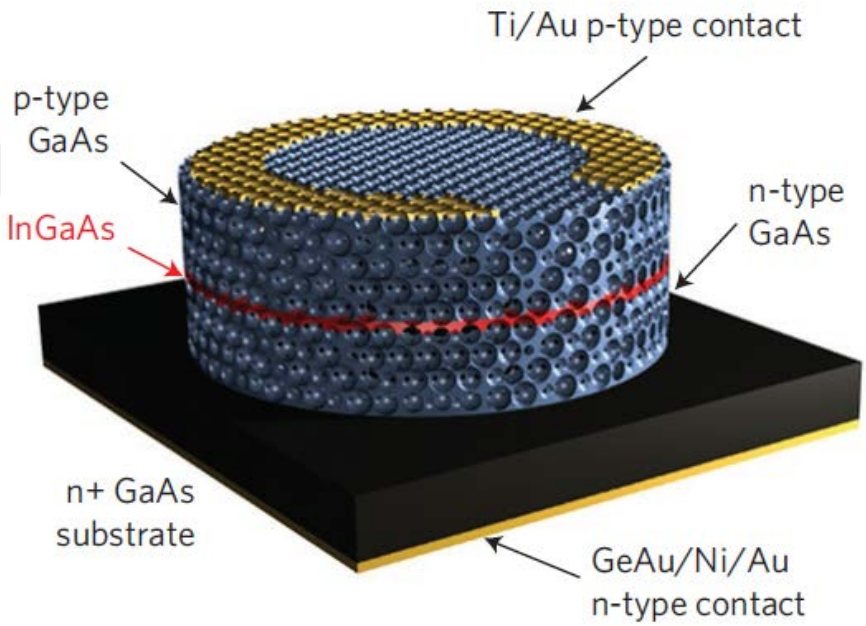

Figure 3.1 Schematic of Nelson's GaAs based inverse opal PC with an InGaAs (Nelson et al., 2011)

Owing to the interconnected macro-pores, relatively large surface areas, low tortuosity, and large voidage benefits, inverse opal PC structures with ordered macro-porous are attractive materials for various applications in electrochemical devices. Kim et. al. studied on the inverse opal platinum electrode for enhanced mass transfer in fuel cells. They have demonstrated a route for the direct and facile application of

the inverse opal Pt electrode in a practical membrane electrode device (Kim et al., 2013).

The structural color one of the application areas of inverse opal photonic crystals that could be applied in a short period (Aguirre et al., 2013; Wang et al., 2019). For example Schroden et. al. produced colorful PC powders from silica, titania, and zirconia. The powders with stop bands indicated brightly color and optical filtering behavior. They found that the wavelengths of the colorful reflections proportional to the pore size and to change according to the refractive index of the fluid filling the pores (Schroden et al., 2002). In addition, opal PC structures are directly used for structural color formation. For example, Viel et. al. produced synthetic opals from polymeric core-shell by a fast melt-flow technique that permits the large-scale production (Viel et al., 2007). Because of the elastomeric shell (core of the beads was rigid) polymeric films could be strained considerably. They observed strong blue shift of the reflected color by the deformation. They suggested that these PC materials could be used as deformation sensors with this sensitivity (Viel et al., 2007).

PC colorimetric sensors can reply to various stimuli including, humidity, magnetic field, electric field, temperature, pH, ions, DNA molecules, and deformation mechanism by tuning the lattice parameter or effective refractive index of PC (Hou et al., 2018). As an example, Zhao et. al. produced a visual inverse opal hydrogel sensor that can be triggered by pH, temperature, and light is represented in Figure 3.2 (Zhao et al., 2018). They mentioned that, the structural color of the sensor turned from blue to orange-red by decreasing pH and reversibly recovered by increasing pH. In addition, the green color of the inverse opal sensor changed to violet by applying a temperature field according to the study (Zhao et al., 2018).

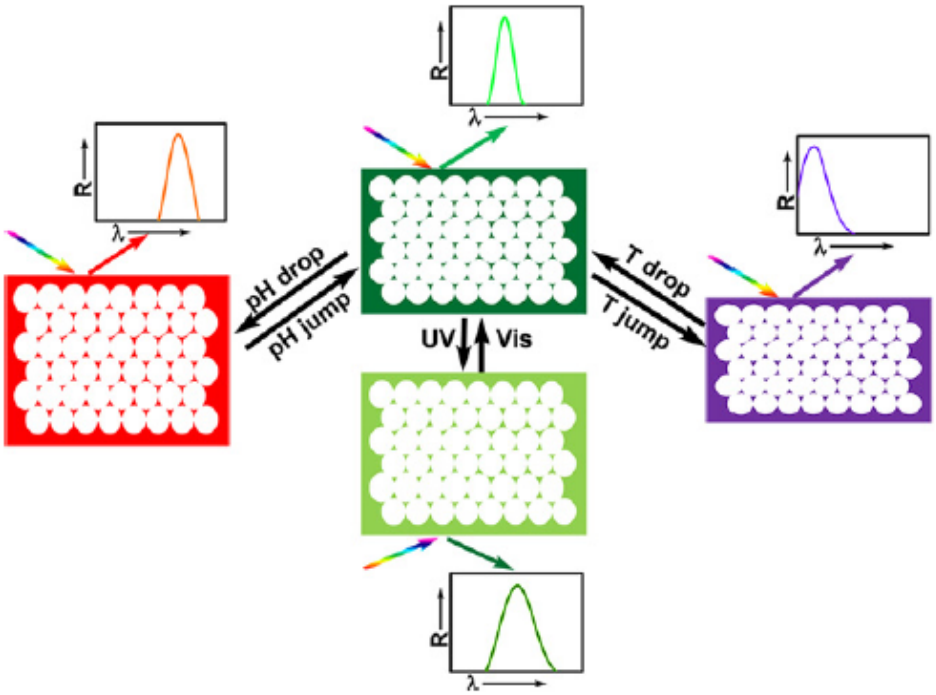

Figure 3.2 Zhao's visual multi-triggered sensor based on inverse opal hydrogel which responses to pH, temperature and light (Zhao et al., 2018)

It was not difficult to find the application area for structural colors. One of the first attempts was to apply structural color to textile surfaces. As an example, Li et. al. studied self-assembly composite photonic crystals on fabric substrates (Li et al., 2018). They assembled SiO_2/P(MMA-BA) composite PCs on fabric substrates via a co-assembly of small-sized P(MMA-BA) copolymer and large-sized SiO_2 microspheres. They found the obtained structural colors of photonic crystals is strongly affected by the size and volume ratios of the two components. Especially, it is an important result that, the smaller size ratio improves the brightness of the structural colors of the PC fabrics (Li et al., 2018).

3.2 Materials

Methyl methacrylate (MMA, 99%) and potassium persulfate (99%) used for PMMA colloidal crystal production they are supplied from Alfa Aesar and Sigma Aldrich, respectively.

Chemicals for productions of un-doped and doped SiO_2 inverse opal PC coatings such as tetraethyl orthosilicate (TEOS ≥ 99%), cerium (III) chloride ($CeCl_3$ ≥ 99.9%), and samarium (III) oxide (99.9%), europium (III) chloride hexahydrate (99.99%), terbium (III) nitrate hydrate (99.99%), hydrochloric acid (99.999%) and absolute ethanol were supplied from Sigma Aldrich Corporation.

3.3 Production Steps

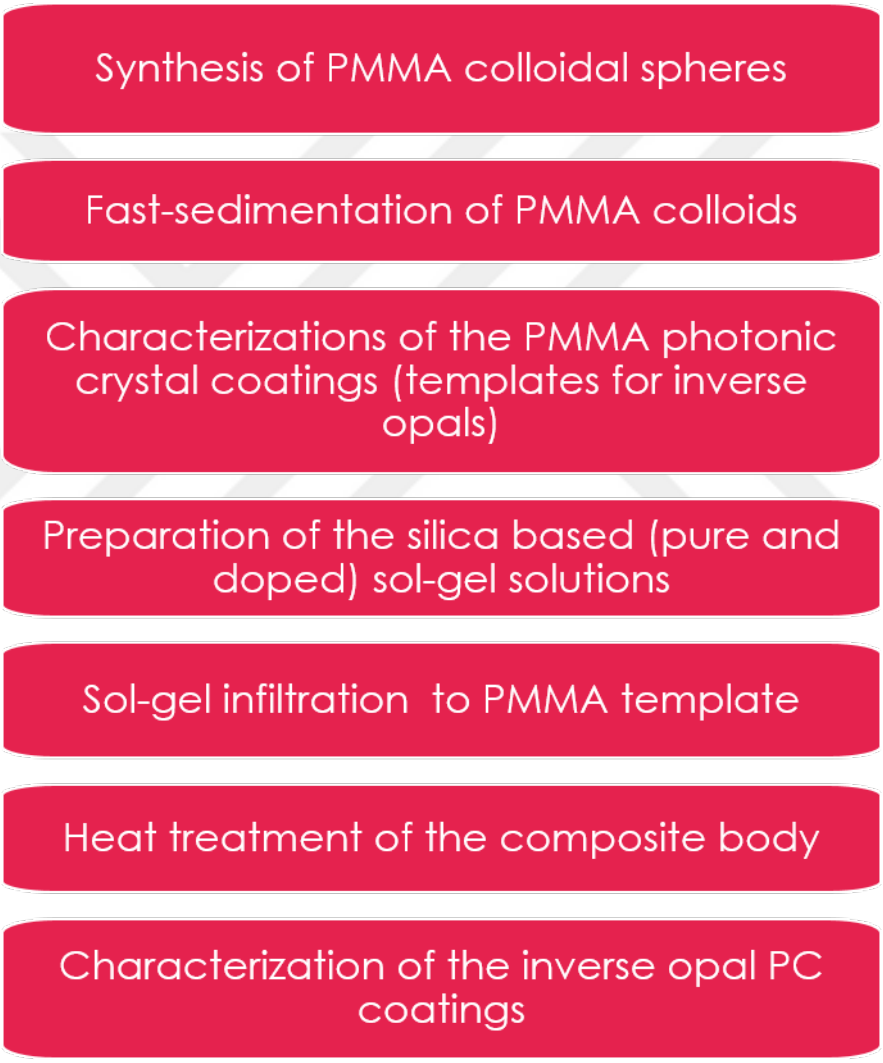

Figure 3.3 Flowchart of production and characterization steps

Flowchart of production and characterization steps is given in Figure 3.3. Production and characterization processes will be presented in detail in subtitles.

3.3.1 Synthesis of PMMA Colloids

The PMMA colloidal spheres were synthesized by the free radical induced polymerization of methyl methacrylate (MMA) in water. The experimental setup of the free radical induced polymerization of PMMA colloids is presented in Figure 3.4. As clearly can be seen from Figure 3.4, the production process was carried out in a round-bottom flask with MMA/pure water (in volume ratio) is adjusted as 1/8. The potassium persulfate ($K_2S_2O_8$) was used as an initiator and the reaction is continued for two hours under nitrogen atmosphere by stirring. Potassium persulfate was added at the amounts of 0.35 millimolar (mM), 0.70 mM and 1.05 mM and the reaction temperature range was adjusted between 75 and 90 ^oC. Sample abbreviations of PMMA colloidal crystals according to the synthesis parameters of initiator amount and reaction temperature are given in Table 3.1.

Firstly, MMA and adequate amounts of water were poured into the round-bottom flask over Heidolph MR Hei-Tec model magnetic stirrer and heater, with a water-cooled condenser. The mixture was stirred at 350 rpm during the entire production period. Nitrogen was bubbled slowly for 30 minutes in order to obtain an inert atmosphere. The temperature was raised to 75-90 °C with 5 °C intervals, and stabilized at the planned synthesis temperature. Later, potassium persulfate was added at the different amounts in order to determine the optimum initiator concentration. The synthesis of PMMA colloidal spheres was completed after a 2 hours reaction time. This reaction time was determined according to a similar literature study (Waterhouse & Waterland, 2007). Finally, the large agglomerates were separated by filtering the obtained PMMA colloidal suspension. PMMA 5 with the 0.7 mM of Potassium persulfate and reaction temperature of 85 °C has been chosen for opal template productions of inverse opal PC coatings due to the best opal morphology.

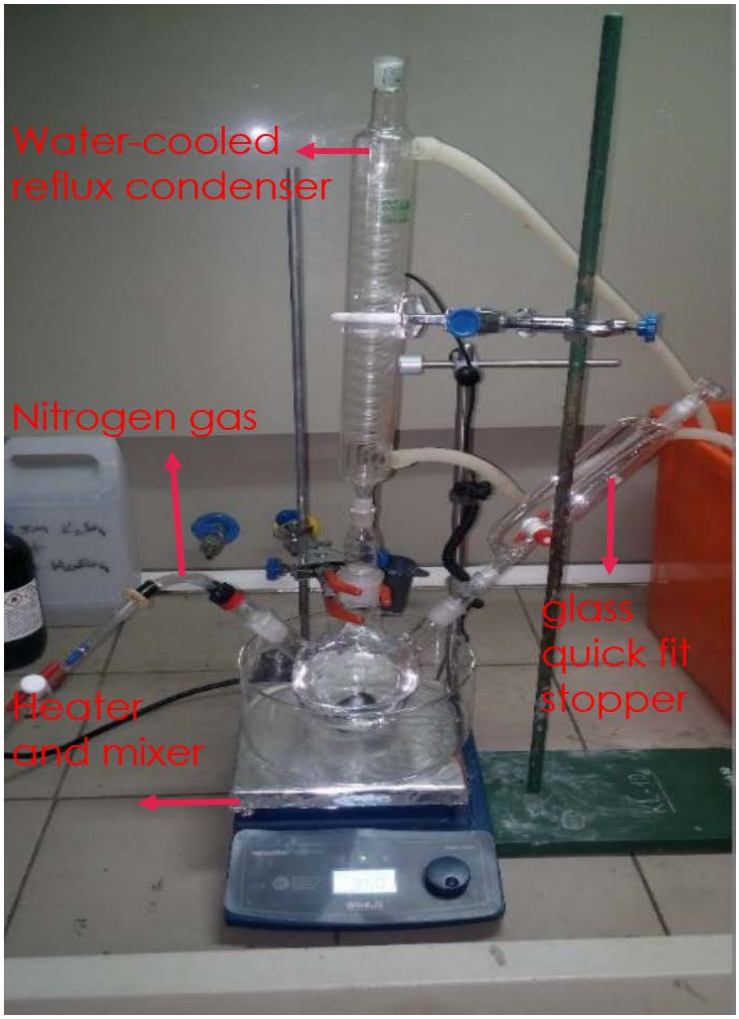

Figure 3.4 Experimental setup of the free radical induced polymerization of PMMA colloids (Personal archive, 2019)

Table 3.1 Sample abbreviations according to production conditions of the PMMA colloids

Sample Name	Temperature (°C)	$K_2S_2O_8$ (mM)
PMMA1	80	0.35
PMMA2	80	0.70
PMMA3	80	1.05
PMMA4	75	0.70
PMMA5	85	0.70
PMMA6	90	0.70

3.3.2 Preparation of PMMA Colloidal Crystal Templates

Borosilicate glass was used as a substrate material in the dimensions of 15x15x2 mm. A cleaning procedure was applied to the substrate glass by holding in a piranha solution (sulfuric acid (H_2SO_4)/hydrogen peroxide (H_2O_2) ratio= 3:1) for 24 h after pre-cleaning with acetone and distilled water.

The sedimentation method is one of the most popular techniques for preparation of colloidal crystal. The sphere size and their size distribution, the evaporation time and drying temperature are the basic parameters that determine the opal quality. Two different experimental designs were made for the PMMA colloidal crystal part. One of them is focused on fast-sedimentation parameters, the other is focused on synthesis parameters of PMMA spheres. Heat triggered sedimentation technique used to depose the PMMA suspension on the glass substrates.

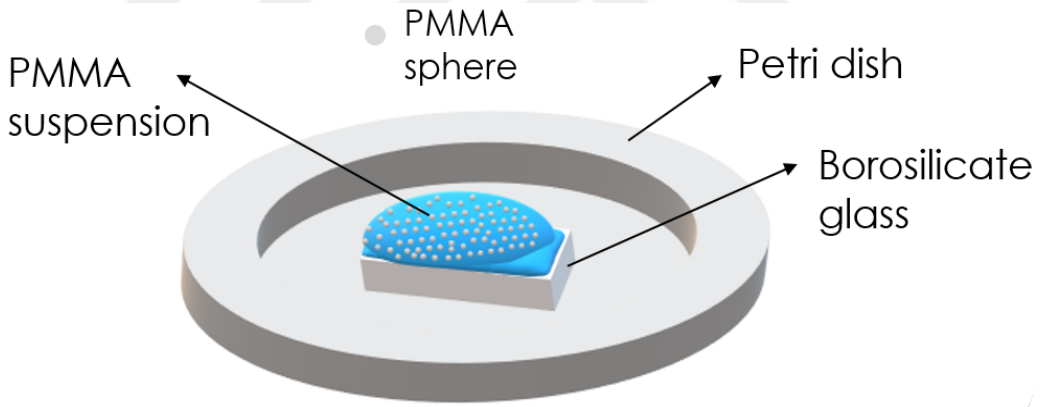

Figure 3.5 Schematic representation of modified fast-sedimentation processes for PMMA colloid template

The fast-sedimentation method, which is developed for this thesis is schematically presented in Figure 3.5. Firstly, 300 µl PMMA colloidal suspension is poured on the surface of the prepared glasses placed in the related drying atmosphere. In order to evaporate the water from the PMMA suspension, two distinct drying systems were established.

Evaporating process in the furnace at 30 and 40 ^{o}C is the first method while evaporating in an oil bath at 30, 40 and 50 ^{o}C is the second method and all methods

are performed for 24 hours. O-30, O-40, and O-50 express sedimentation in the oil bath at 30, 40 and 50 ºC while, F-30, and F-40 mean sedimentation in the furnace at 30 and 40 ºC for PMMA colloidal crystal samples, respectively.

As can be seen from Figure 3.5, PMMA suspension applied substrate is placed in a Petri dish over an oil bath for inverse opal productions. The samples are kept at 30 ºC for 24h in order to obtain ordered PMMA crystal template that is O-30 PMMA sample conditions.

3.3.3 Sol-gel Infiltration

The sol-gel infiltration method for inverse opal production is presented schematically in Figure 3.6. The requirement for inverse opal photonic crystal production is a template consists of regularly arranged colloidal crystals. The cavities of this PMMA template are filled by the sol-gel solution of the desired material. The inverse opal PC morphology is obtained when the PMMA template is removed from the composite structure by the heating process.

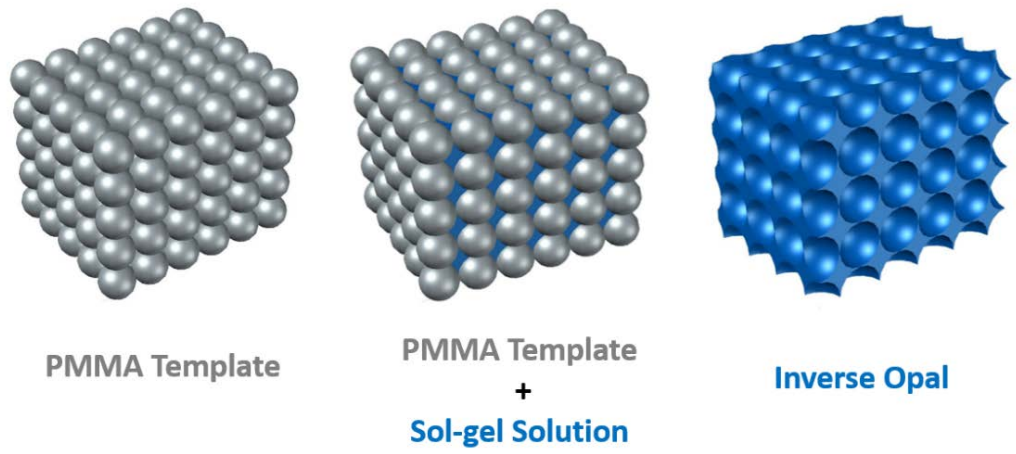

Figure 3.6 Schematically presentation of the inverse opal PCs by the sol-gel infiltration method

The sol-gel solutions of undoped and doped samples were prepared for both coatings which are in the forms of thin-film and PC. 0.257-mole anhydrous ethanol and 0.8723% mole TEOS were mixed for 1h. Later, 1.78% mole HCl acid was added

into solution as a chelating agent. The doping process is carried out with mixing the related dopant precursors with the solutions. Cerium (III) chloride, samarium (III) oxide, europium (III) chloride hexahydrate and terbium (III) nitrate hydrate amounts were determined according to the molar ratios of 0.25%, 0.50%, 0.1%, 0.2% for all Ce/Si , Sm/Si, Eu/Si and Tb/Si solutions. The aging process of the prepared solutions was completed after keeping at room temperature for 24 h.

The infiltration of the prepared sol-gel solutions was conducted by the spin coating method. Borosilicate glass substrates were directly used for thin film coatings while borosilicate glass substrates coated by PMMA colloidal crystals were used for inverse opal PC coatings. Spin coating parameters are adjusted as coating speed: 500 rpm and coating time: 30 seconds. In this way, infiltration of the sol-gel solutions into the cavities of the PMMA template is completed for inverse opal PC coatings.

3.3.4 Heat Treatment

The heat treatments of the silica-based coatings were carried out gradually in order to prevent crack formations. The schematically graphic of the heat treatment steps of the silica-based coatings is given in Figure 3.7. The heating rate was set as 2 °C/min until 300 °C, for higher temperatures it turns to 5 °C/min. Holding at 100°C, 300°C, and 550 °C continued for 60 minutes for each steps. The drying process is carried out at 100 ^{o}C, removing the PMMA spheres from the composite structure is ensured at 300 ^{o}C and finally, calcination was completed at 550 °C. In this way, the productions of the thin-film and PC coatings are completed. Abbreviations of the silica-based coatings according to the coating form, dopant kind and ratio were given in Table 3.2.

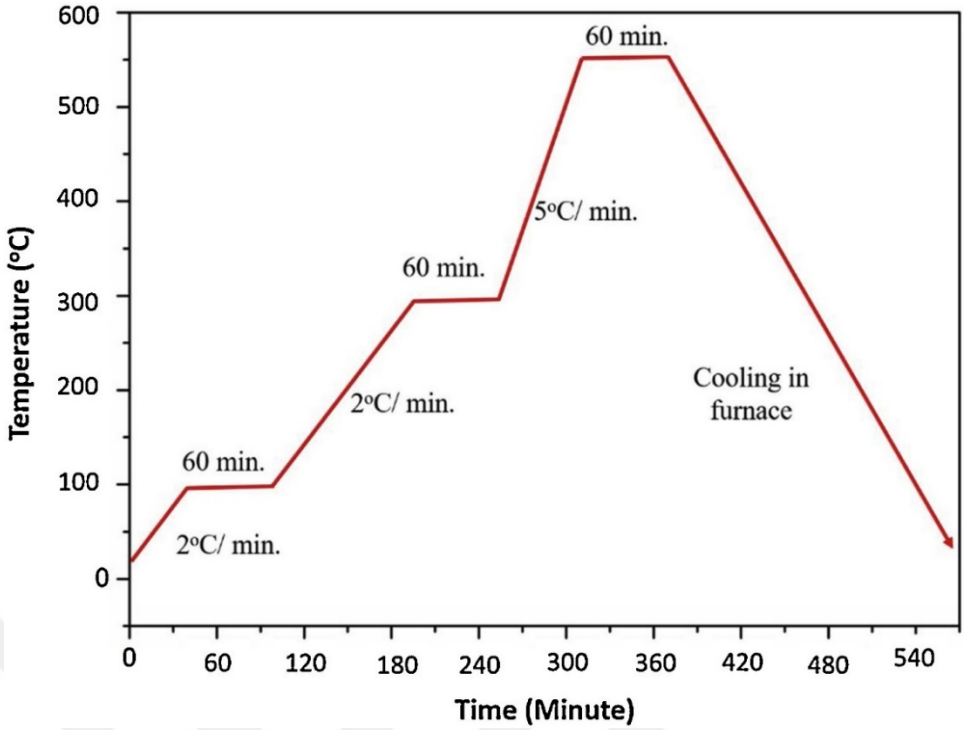

Figure 3.7 Heat treatment steps of the silica based coatings

Table 3.2 Abbreviations of PC and thin-film coatings according to the coating type, dopant species and dopant ratio

Sample Codes		**Dopant Ratio (%)**			
PC Form	**Thin-Film Form**	**Ce**	**Eu**	**Sm**	**Tb**
PC-SiO_2	TF-SiO_2	-	-	-	-
PC-C25	TF-C25	0.25	-	-	-
PC-C50	TF-C50	0.50	-	-	-
PC-C100	TF-C100	1	-	-	-
PC-C200	TF-C200	2	-	-	-
PC-E25	TF-E25	-	0.25	-	-
PC-E50	TF-E50	-	0.50	-	-
PC-E100	TF-E100	-	1	-	-
PC-E200	TF-E200	-	2	-	-
PC-S25	TF-S25	-	-	0.25	-
PC-S50	TF-S50	-	-	0.50	-
PC-S100	TF-S100	-	-	1	-
PC-S200	TF-S200	-	-	2	-
PC-T25	TF-T25	-	-	-	0.25
PC-T50	TF-T50	-	-	-	0.50
PC-T100	TF-T100	-	-	-	1
PC-T200	TF-T200	-	-	-	2

3.4 Characterizations

3.4.1 Fourier Transform Infrared Spectrometer

Fourier Transform Infrared Spectroscopy (FT-IR) can be thought of as fingerprint of the molecules of a material. It is an effective instrument for identifying types of chemical bonds in a molecule by producing an infrared absorption spectrum. Two different compounds never exhibit the complete same infrared spectrum as each material has a unique atom combination. Although FTIR analysis can be used for the characterization of all material groups, it is preferred especially for the organic materials. The chemical bonds in a molecule of material can be detected by evaluating the infrared absorption spectrum, which is obtained with FTIR analysis.

Depending on the type of bonds and elements, molecular bonds vibrate at various frequencies according to the principle. A bond can vibrate at some specific frequencies. The lowest frequency generally corresponds to the ground state while higher frequencies correspond to the excited states considering the quantum mechanics. Absorbing light energy excites the bond and increases the frequency of molecular vibration. The energy difference between two states is equal to the light energy, which is determined by the wavelength value. These energy differences belong to the molecular vibrational states is about 1-10 kilocalories/mole which related to the infrared part of the electromagnetic spectrum. The FTIR results are usually given with a graph plotted as a function of absorbance (or transmittance) versus wavelength (Birlik, 2011).

Perkin Elmer Spectrum BX model FTIR device illustrated in Figure 3.8 was used in the aim of characterizing functional groups of the PMMA samples within the range of 4000-600 cm^{-1} and a resolution of 2 cm^{-1}. The obtained FTIR absorbance spectrums as a function of wavelength were repeated 25 times for one sample.

Figure 3.8 Image of the used FTIR device having ATR apparatus (Personal archive, 2019)

3.4.2 Particle Size Distribution

The Malvern Zetasizer Nano ZS model device using dynamic light scattering principle as illustrated in Figure 3.9 characterized the particle size distribution of the PMMA spheres in water. Additionally, particle sizes of the PMMA spheres were found by the means of SEM images to eliminate the shrinkage effect of the drying process. In this way, LUCIA image analysis software was used in order to determine average PMMA particle size values and their standard deviations.

The polydispersity indexes (PDI) and the polydispersity (PD) values of the samples were calculated using formulas of (1) and (2) given below.

$$\text{PDI}=\frac{\sigma^2}{Z^2} \tag{3.1}$$

$$\%\text{PD}=\sqrt{PDI}\times 100 \tag{3.2}$$

in which Z and σ expresses mean particle size and standard deviation values (Dalmis et al., 2019a).

Figure 3.9 Malvern Zetasizer Nano ZS model device (Personal archive, 2019)

3.4.3 Differential Thermal and Thermogravimetric Analysis

Thermal characterization methods benefit from the dynamic relationship between temperature and mass/heat absorption or emitting from it. The most important thermal methods used in the characterization of materials are the Thermogravimetry (TG) and Differential Thermal Analysis (DTA).

TG analysis is based on the measuring weight variation of the sample as its temperature changes. Another hand, DTA analysis is based on heat-absorbing or emitting status that can be determined by measuring the temperature difference between an inert reference material (generally alumina powder) and the sample while the temperature of the system is increased with a constant rate (Birlik, 2011).

A Perkin Elmer STA 8000 TG/DTA device (presented in Figure 3.10) was used for Differential thermal analysis (DTA) and Thermogravimetric analysis (TGA) of the dried silica-based gels. The analysis range was between room temperature and 900 °C while the heating rate was kept constant at 5 °C/min during heating. The rare-earth dopant effects on the thermal characteristics were investigated.

Figure 3.10 Perkin Elmer STA 8000 TG/DTA device (Personal archive, 2019)

3.4.4 X-Ray Diffraction

X-ray diffraction (XRD) analysis is a very effective technique especially for determining the crystalline phases of the powders or films. Additionally, it is used to analyze crystalline grain size, stress, phase composition, and crystal orientation of the materials. Generally speaking, it is possible to obtain a diffraction pattern that emerges that is characteristic of a sample by varying the angle of incidence. The obtained pattern identified by matching with an internationally recognized database powder diffraction (ICDD) file reference patterns that is called the "search-match" process (Birlik, 2011).

Rigaku D/Max-2200/PC X-ray diffractometer device, whose image is given in Figure 3.11, was used in order to determine crystal structures of the silica-based coatings. Analyses were carried out in the 2θ range of 3–90º. CuK_{α} radiation (λ=1.5405 Å) was used as the radiation source at 40 kV and 36 mA.

Figure 3.11 X-Ray Diffractometer, Rigaku, D/Max-2200/PC (Personal archive, 2019)

3.4.5 X-Ray Photoelectron Spectroscopy

The elemental composition, chemical state, empirical formula and electronic state of the elements of a material is determined quantitatively by X-ray photoelectron spectroscopy (XPS). X-ray beams are irradiated to the material surface and simultaneously the kinetic energy and number of electrons that left from the top 1 to 10 nm of analyzing material are measured at XPS analysis. An ultra-high vacuum (UHV) condition is necessitated for XPS analysis.

It can be used to analyze the surface chemistry of the received material. Besides, it can be used to characterize the effects of the fracturing, cutting or scraping process or effects of ion beam etching, heating reactive gases, solutions, beam implant and ultraviolet light. All elements which have equal or higher atomic number of 3 (lithium) could be detected by the XPS analysis. Due to very low diameter of orbitals, hydrogen and helium cannot be detected with XPS by reducing the catching probability. Thermo

Scientific K-Alpha device with a monochromatic Al-K_α (1486.7 eV) X-ray source was used for XPS analysis. The device used in XPS analysis is given in the Figure 3.12. The aim of the XPS was characterization the elemental composition and surface properties of the silica based inverse opal PC coatings. The beam size was 400 nm diameter and the pressure of the system was kept at below 5×10^{-10} mbar (Erol, 2013).

Figure 3.12 Thermo Scientific K-Alpha XPS device (Personal archive, 2020)

3.4.6 Scanning Electron Microscopy

Scanning electron microscopy (SEM) is an analytical method generally used in order to examine the surface morphology of the solid-state specimens. A tiny, high-energy electron beam scans the surface of the sample in SEM analysis. The interaction between the electron beam and the sample produces a series of radiations (Ebeoglugil, 2011).

Different kinds of electrons can be detected after interacting electron with the surface. The secondary electrons (SEM), backscattered electrons (BSE) and characteristic X-rays are the basic types of signals produced in the SEM system. Secondary electron signals consist of the interaction of an electron with atoms on the surface of the sample. Secondary electron signals (SEI) consist of the interaction of an

electron with atoms on the surface of the sample. High-resolution images of a sample surface can be obtained by the secondary electron imaging for morphological characterization. SEM images have a large depth of field endorse a characteristic three-dimensional appearance due to the very narrow electron beam. Theoretically, high magnifications could be obtained such as 300000 times magnification (Birlik, 2011).

The electron beams that are reflected from the sample surfaces by elastic scattering are called as Back-scattered electrons (BSE). BSE images are used for characterization of the distribution of different elements in the screen as the BSE signal intensities are strongly related to the atomic number of the elements. Therefore, BSE results should be interpreted with the characteristic X-ray results (Birlik, 2011).

When primer electron hits the characterized material, the electron beam can remove an electron of material from the inner shell. It causes emitting a characteristic X-ray beam whose energy is equal to the energy difference between the removed and replaced electron orbits. An energy spectrum is obtained by these characteristic X-ray measurements to identify the composition and measure the amount rates of elements in the sample (Birlik, 2011). JEOL JSM-6060 model SEM device, as depicted in Figure 3.13, was used for morphological characterizations of the PMMA opal and silica-based inverse opal PC coatings. Additionally, it was utilized for particle size measurements of PMMA colloidal spheres.

Figure 3.13 JEOL JSM-6060 model SEM device (Personal archive, 2019)

3.4.7 Optical Characterization

Optical characterizations of the opal and inverse opal photonic crystal coatings are carried out by the UV-VIS spectrophotometer and optical microscope. The UV-VIS spectrophotometer is used to determine reflectance, absorbance or transmittance properties according to the wavelength especially in UV and visible region range. Thermo Scientific Evolation 600 UV-VIS spectrophotometer device, depicted in Figure 3.14 (a), was used for optical characterization of the opal PMMA and silica based inverse opal photonic crystal coatings. Reflectance percentages of photonic crystals were measured and transferred graphics in the wavelength range of 325-725 nm. The optical microscope is used in order to support reflectance measurements. Nikon Eclipse ME600 model optical microscope, illustrated in Figure 3.14 (b), was used to show structural colors of the coatings (Dalmis et al., 2019b).

(a) (b)

Figure 3.14 (a) Thermo Scientific Evolation 600 UV–VIS spectrophotometer device and (b) Nikon Eclipse ME600 model optical microscope (Personal archive, 2019)

CHAPTER FOUR
RESULTS AND DISCUSSIONS

4.1 Opal Photonic Crystal Coatings

Opal structure consists of regularly arranged colloidal spheres. Opal PC materials are used in sensors, lenses, structural color, display devices and photonic paper applications. The most important point of obtaining a functional opal structure is sufficiently regular arranging colloidal spheres. Especially as the colloidal spheres decrease in size, it becomes more difficult to arrange them regularly. Generally sedimentation, spin coating, centrifugation, vertical deposition and Langmuir-Blodgett assembly methods have been used in the regular arrangement of PMMA, PS and silica based colloidal spheres. One of the simplest of these methods is the sedimentation method. However, obtaining regular arrange by sedimentation method takes as long as approximately 1-2 months. Therefore, the aim of this study was to increase the efficiency of the sedimentation method by shortening its duration. In addition, it was aimed to reveal the effect of PMMA sphere production parameters on opal PC coatings.

4.1.1 Effects of Sedimentation Process Parameters on Opal PC Coatings

Due to the low-cost and simple way for fabricating three-dimensional photonic band gap (PBG) crystals in large area, sedimentation methods have been widely preferred. Generally, the sedimentation process start with the production of monodispersed colloidal particles are obtained. Then, self-assembling of the colloidal particles is carried out and finally if it is necessary, heat treatment is performed (Almeida & Portal, 2003).

Nevertheless, high quality ordered colloidal photonic crystal production by the sedimentation method takes a long time (Liau & Huang, 2008). There are some studies concentrated on the many powerful factors of opal photonic crystal film formation by self-assembly sedimentation in the literature (Chung et al., 2005; Gu et al., 2005; Kuai

et al., 2004; Landon & Glosser, 2004; Zhang et al., 2005). Temperature, relative humidity, the concentration of the suspension particle, particle size, surface tension on the quality of the crystal are some parameters that were discussed (Gu et al., 2005; Kuai et al., 2004; Landon & Glosser, 2004; Zhang et al., 2005). Yet, it could not found a study investigates both drying temperature and medium entire the sedimentation process. Therefore, one of the objective of this thesis is to examine the quality of the opal structures in terms of drying temperatures such as 30, 40 and 50 °C and drying media such as furnace and oil bath. Two distinct sedimentation experimental setup were established to determine the order of the PMMA spheres (produced at 85 °C with a 0.70 mM initiator) assembled in furnace or oil bath media.

Surface SEM images of the PMMA opal photonic crystal coatings captured at low (2500x)) and high (30000x) magnifications are depicted in Figure 4.1. It can be observed that the coatings assembled in the furnace medium do not have a regular arrangement; they have many randomly oriented domains according to the SEM images in Figure 4.1 (a-f). It can be pointed out that the airflow in the oven might cause an increase at the drying rate of PMMA colloidal suspension. This case does not give enough time for the regular arrangement of the PMMA colloidal spheres. However, it can be seen that the coating samples assembled in the oil bath medium have a regular arranged PMMA colloidal crystal morphology according to the SEM images in Figure 4.1 (g-k). When detailed surface images are observed at high magnification (30000x) in Figure 4.1 (h), (i), and (l) it can be obviously expressed that all coating samples obtained in the oil bath have a good colloidal arrangement. Nonetheless, according to the general view of the coating surface images taken at 2500x magnification (Figure 4.1 (g), (h) and (k)), it can be clearly seen that there are differences at the arrangements of the PMMA crystals depending on the sedimentation temperature. It can be concluded that the best performance in terms of PMMA order in large areas is obtained at the O-30 sample, which is obtained by the sedimentation performed at 30 °C in the oil bath.

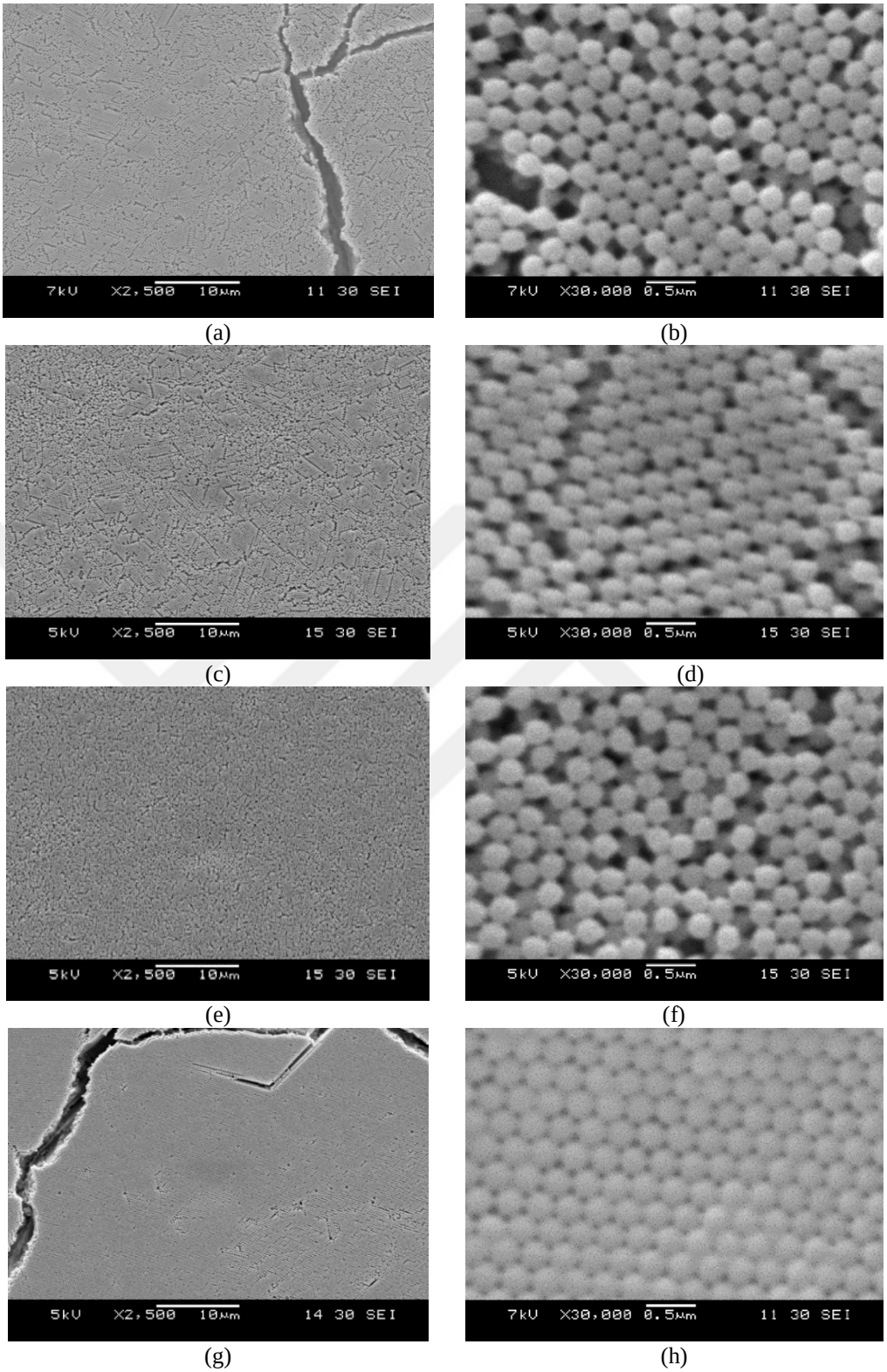

Figure 4.1 SEM images of the (a-b) F-30, (c-d) F-40, (e-f) F-50, (g-h) O-30, (i-j) O-40 and (k-l) O-50 PMMA opal coatings at 2500x and 30000x magnifications, respectively

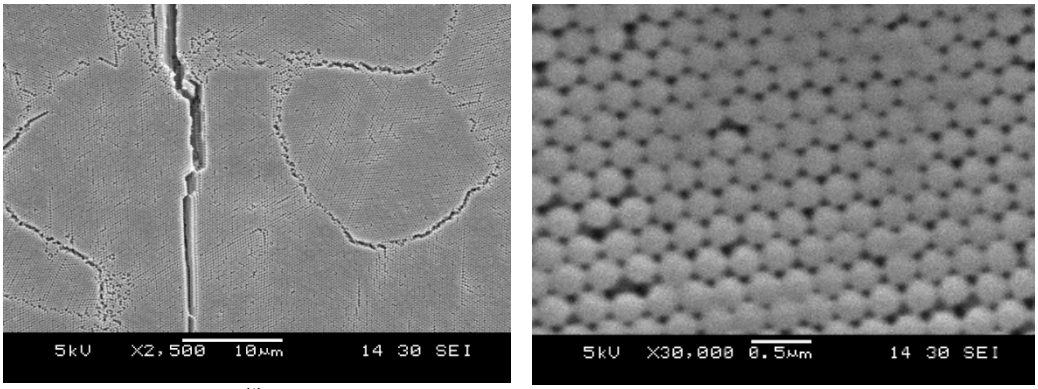

(i) (j)

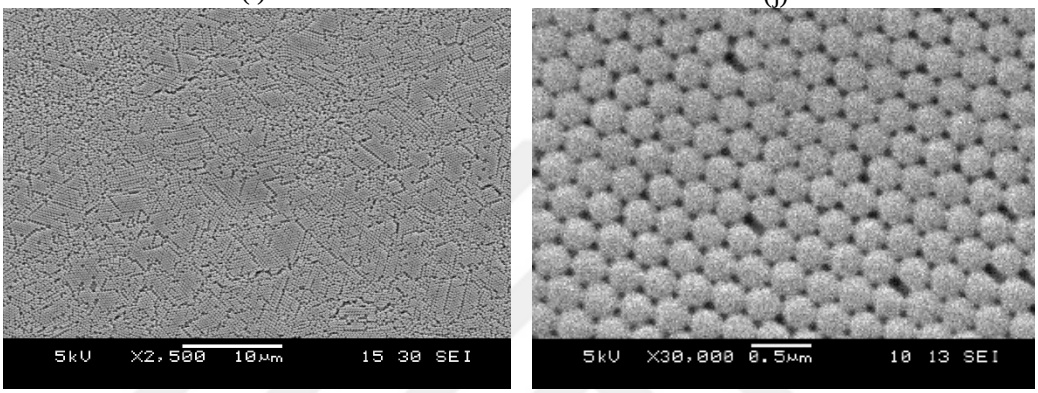

(k) (l)

Figure 4.1 continues

The PMMA colloids move randomly named Brownian motion in the suspension medium (Gugliotti et al., 2004). The Marangoni effect is mainly concerned with the motion of the liquids by the help of a surface tension gradient. The Marangoni motion leads to flow away the liquid from low surface tension areas (Gugliotti et al., 2004). Note that the variations in the composition and temperature may cause the generation of surface tension. Fluid moves to the convection motion direction (thermo-capillary flow) by the surface tension, which is obtained by heating the fluid surface (Dalmis et al., 2019a). As mentioned beforehand the best opal coating quality was obtained at the O-30 sample (assembled at 30 ^{o}C in the oil bath) according to the SEM results. The quality of the opal coating has deteriorated at the samples assembled at higher deposition temperatures such as 40 ^{o}C and 50 ^{o}C. On account of the increased surface tension of the fluid with increased temperature, an increase in both Brownian motions of the particles and the fluid is observed (Gmachowski, 2019; Gugliotti et al., 2004). It is thought that this phenomenon could be the reason for the deterioration of the

quality of the opal coating, as it will extend the time required for the alignment of the PMMA colloids.

Even though the sedimentation method is very simple, it takes a long process time such as weeks or months depending on the size of the spheres (Okubo, 2008; Sawada et al., 2001). It is fair to emphasize here that an important result highly ordered opal PC structure could be obtained in 24 h with the fast-sedimentation system at 30 °C in an oil bath according to the SEM results given in Figure 4.1. In this way, it was succeeded to shorten the time required for the sedimentation process about 20-30 times.

4.1.2 Effect of the Synthesis Parameters on Opal PMMA PC Coatings

4.1.2.1 Results of Particle Size

The quality of the opal PC coatings is investigated with respect to PMMA synthesis parameters such as the initiator (potassium persulfate-$K_2S_2O_8$) amount (0.35 mM, 0.70 mM and 1.05 mM) and synthesis temperatures (75°C, 80°C, 85°C, 90°C). The particle size results of the PMMA samples taken by both zeta sizer and SEM given in Table 4.1. The highest PMMA particle size was obtained from PMMA 6 samples while the smallest particle size was at PMMA 1 sample according to the particle size measurement results. It is important to highlight that PMMA sphere size was increased from 264 nm to 284 nm by the increase in reaction initiator (potassium persulfate-$K_2S_2O_8$) amount. The results of the reaction temperature effect exhibited similar behavior. Keeping in mind that the particle size of the PMMA colloids increased from 264 nm to 296 nm, with the increasing reaction temperature to 90 ^oC.

Table 4.1 Particle size and polydispersity results of the PMMA samples

Sample Code	PSD Sphere Size (nm)	SEM mean particle Size (nm)	Polydispersity Index	Polydispersity (%)
PMMA1	264	208 ±3.2	0.023	15.16
PMMA2	281	231 ±4.4	0.036	18.97
PMMA3	283	264 ±4.3	0.026	16.12
PMMA4	272	236 ±3.9	0.027	16.43
PMMA5	290	277 ±4.2	0.026	16.12
PMMA6	296	283 ±5.1	0.032	17.88

According to Table 4.1, it can be seen that there is a variation between particle size results obtained by the SEM and PSD (particle size distribution). The measuring environments could cause these differences ranging from 15 to 56 nm because SEM measurements were performed in a vacuum medium while PSD analyses were carried out in a liquid medium. In other words, dimension changes are observed due to the shrinkage phenomenon at the PMMA spheres during the drying process many examples could be given about the shrinkage after drying process of PMMA, PS or latex colloids (Dalmis et al. 2019a; Joannopoulos et al., 1997; Li et al., 2018; Mazur et al., 2016; Meng et al., 2015). For instance, Waterhouse et. al. mentioned that the sizes of PMMA spheres shrink up to 20-22% after the drying process (Waterhouse & Waterland, 2007). Furthermore, Huang et. al. mentioned that stress production resulted in shrinkage of latex (polymer) particles. Notwithstanding PMMA being water-insoluble, water could penetrate into the capillaries of the spheres due to synthesis in the liquid medium. So that, it is no surprise that the spheres in the hydrous medium are bigger than in the dried medium. Similarly, it is believed that water and monomers removed during the drying process, induce shrinkage of up to 5% (Joannopoulos et al., 1997). It can be concluded that the grain sizes and shrinkage amounts are inversely proportional when the shrinkage amounts are examined in the Table 4.1. As a result, it can be said that PMMA spheres with low particle size have higher shrinkage amounts while PMMA spheres with high particle size have low amounts of shrinkage.

The polydispersity (PD) results of the PMMA colloids are also given in Table 4.1. Polydispersity ratios are ranged between 15.16% and 18.97% whilst Polydispersity index (PDI) values are ranged between 0.023 and 0.036 according to the image analysis program results. If the PDI values lower than 0.04 or similarly PD is lower than 20% the related material can be called a monodispersed material according to the literature (Waterhouse & Waterland, 2007). Therefore, owing to the lower results than the limit values, PMMA spheres are monodisperse.

4.1.2.2 FTIR Results

FTIR spectra belong to the assembled PMMA colloidal crystal coatings are presented in Figure 4.2. The ester group has the most striking peak which is located about 1728 cm^{-1} states the C=O carbonyl stretching band (Rajendran & Uma, 2000a, 2000b; Ramesh et al., 2007). The evident absorption bands located between 1145 cm^{-1} to 1239 cm^{-1} refer to the C-O-C stretching vibrations (Dalmis et al., 2019a). The observed peaks that are located about 1436 cm^{-1} and 750 cm^{-1} are related to the vibrations of the methyl group. By the way, the characteristic band of PMMA polymer

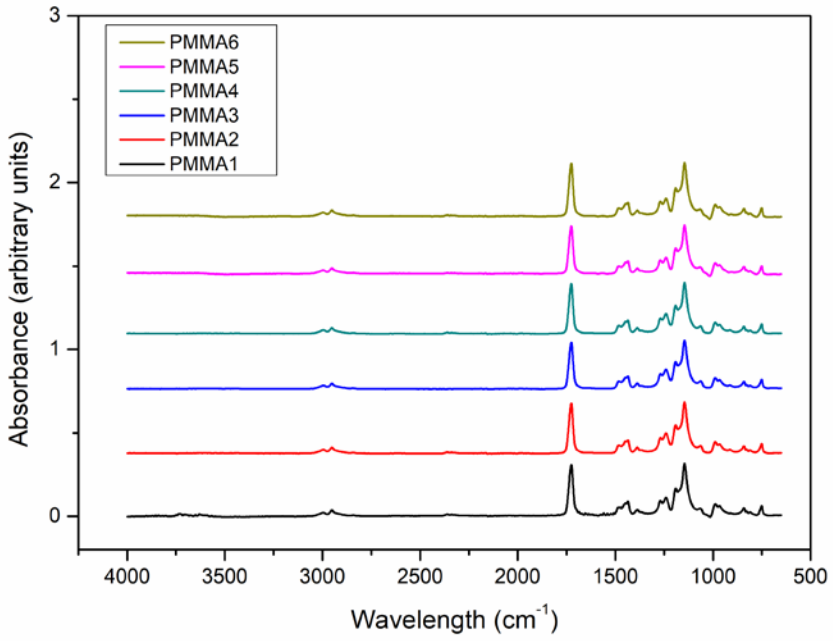

Figure 4.2 FTIR spectra of PMMA photonic crystal coatings

is located at 987 cm^{-1} (Ramesh et al., 2007). Besides, the weak 2952 cm^{-1} and 2997 cm^{-1} peaks could be connected to the stretching vibrations of the C-H bond, which belongs to the CH_2 and CH_3 groups respectively (Rajendran & Uma, 2000a, 2000b; Ramesh et al., 2007). Herewith, it can be concluded that all colloidal opal photonic crystal coatings have the PMMA due to fact that there is no obvious residual MMA peak as the literature supports (Rajendran & Uma, 2000a).

4.1.2.3 Morphological Characterization

Figure 4.3 shows SEM images of the colloidal crystal films obtained by sedimentation method of PMMA spheres at 30 °C for 24 hours in an oil bath. It is general knowledge that general arrangements of the spheres are face-centered cubic lattice or hexagonal close-packed planes (Velev & Lenhoff, 2000; Waterhouse & Waterland, 2007). PMMA spheres were arranged in a hexagonal close-packed (ABABAB...) order by the production of the fast-sedimentation method as can be seen from Figure 4.3. Firstly, in order to observe the effect of the initiator amounts of PMMA on the opal PC assembling, SEM images of the coating samples which were produced with different amounts of (0.35 mM, 0.70 mM, and 1.05 mM) initiators presented in Figure 4.3 (a)-(f). It can be seen from these SEM images, PMMA 1 sample (Figure 4.3 (a-b)) has a disordered arrangement compared to other samples (Figure 4.3 (c-f)). Additionally, the surface and the shape of the PMMA spheres seem distorted. This situation can be attributed to the high surface energy caused by very low PMMA particle size. High surface energy could be inhibited assembling in such a short time (Vollath, Fischer, & Holec, 2018). The order of the PMMA sphere arrangement improves with increasing the initiator amount used in the PMMA synthesis. When the initiator amounts are compared, it can be seen that the PMMA3 sample with 1.05 mM initiator amount has the best order amongst other samples like PMMA1 and PMMA2.

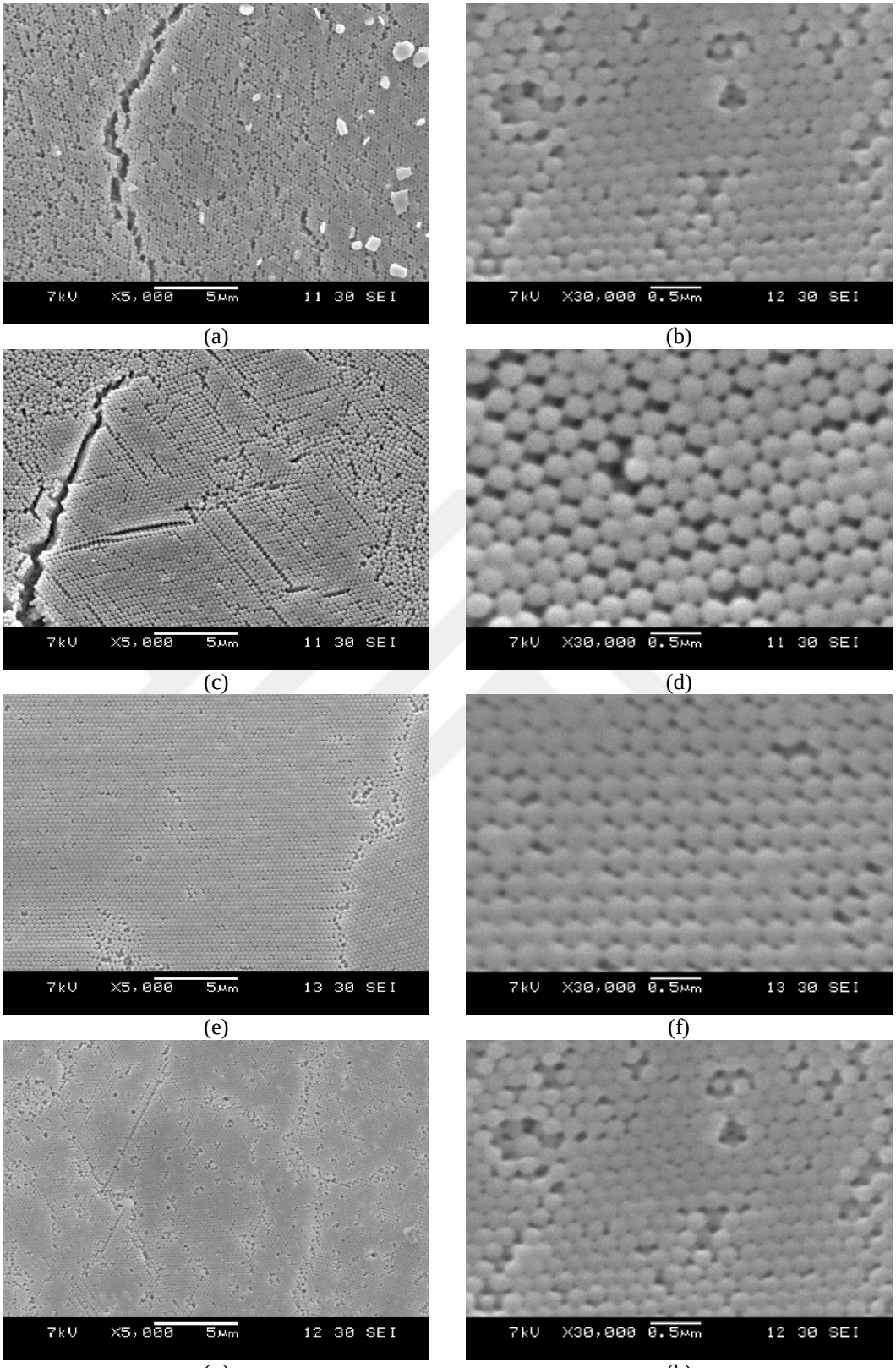

Figure 4.3 SEM surface morphologies of the (a-b) PMMA1, (c-d) PMMA2, (e-f) PMMA3 (g-h) PMMA4, (i-j) PMMA5 and (k-l) PMMA6 opal PC coating samples

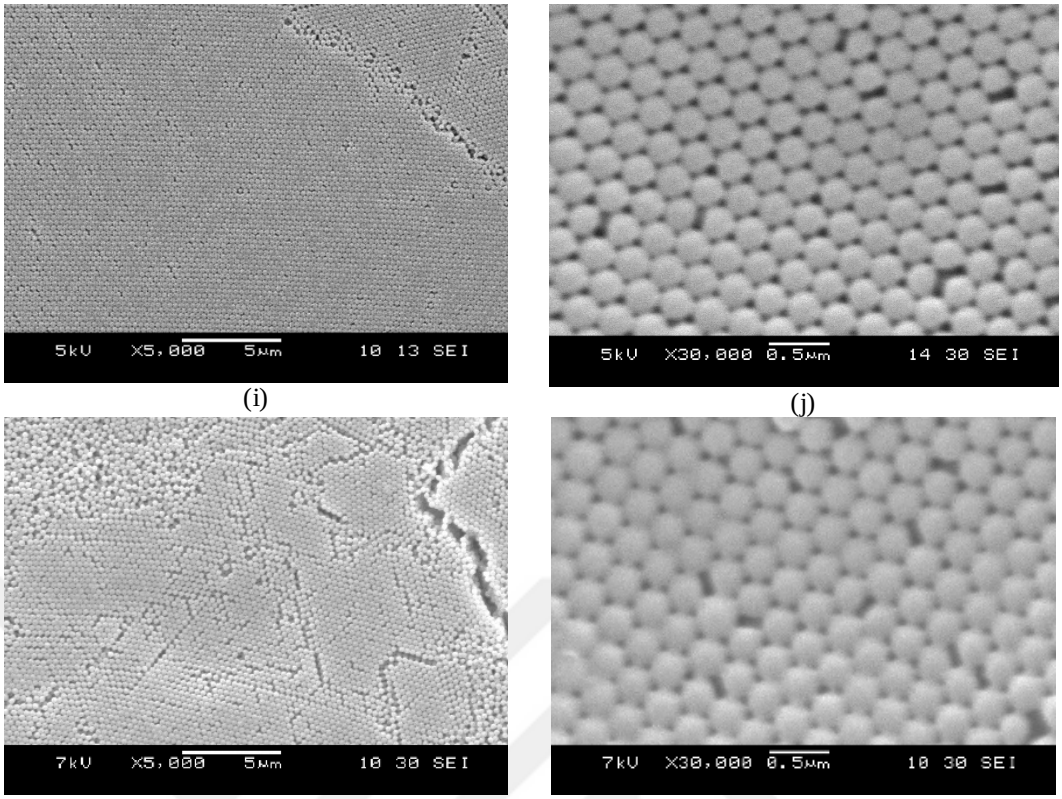

(i) (j)

(k) (l)

Figure 4.3 continues

If the order of the PMMA opal PCs is analyzed considering the temperature variations, it is observed that the PMMA5 sample synthesized at 85 ºC has the optimum order. Due to the fact that the deposition conditions are stable, the PMMA particle size values are common results that could easily be affected by the temperature and the reaction initiator amount variations. From Table 4.1, it is clear that PMMA3 and PMMA5 have very similar particle sizes such as 264 ±4.3 nm and 277±4.2 nm. Thus, the reason for the PMMA3 and PMM5 samples have more regular morphology than other coating samples might be attributed to the PMMA particle size values. Consequently, PMMA3 and PMMA5 samples have optimum sphere sizes for the regular alignment created by the Marangoni effect, Brownian motion, and the gravity force according to the SEM morphologies and particle size results (Dalmis et al., 2019a; Li et al., 2010).

4.1.2.4 Optical Characterization

The reflectance spectra of the PMMA opal PC coatings are presented in the Figure 4.4. In order to verify the interpretations of these UV-Vis reflectance measurements, microstructural images taken by the optical microscope are also shown in Figure 4.5. The reflectance rates of all PMMA samples fall into the visible region from the ultraviolet region by a decrease from high reflectance rates according to the UV-Vis spectra in Figure 4.4. In addition, almost all samples exhibit a peak in the visible region. The wavelength values of these peaks are corresponding to the opal PC coating colors. Generally, opal PMMA PC coatings have peaks in the red wavelength region. As can be observed in Figure 4.4, especially PMMA2, PMMA3 and PMMA5 samples show peaks about 640-670 nm and so they display a red color (Figure 4.5). Inasmuch as the PMMA 6 sample have a peak of about 700 nm, the structural color of the sample shifted from the red color to the near-infrared region. The brightness of the red color tone of the PMMA6 PC sample is diminished as can be observed from Figure 4.5 (f), due to the peak observed in the infrared region.

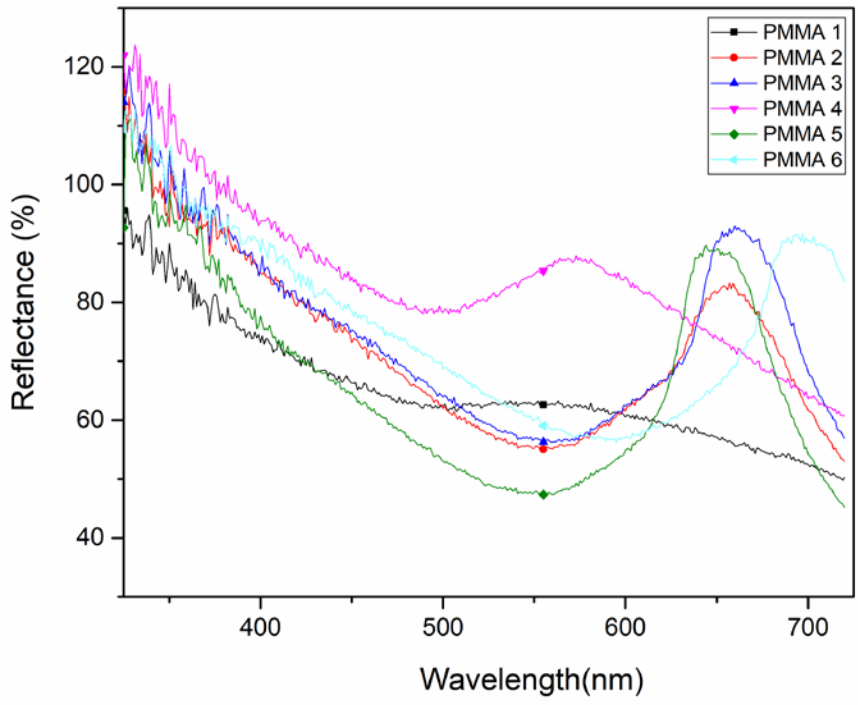

Figure 4.4 Reflectance spectra of the PMMA opal photonic crystal coatings

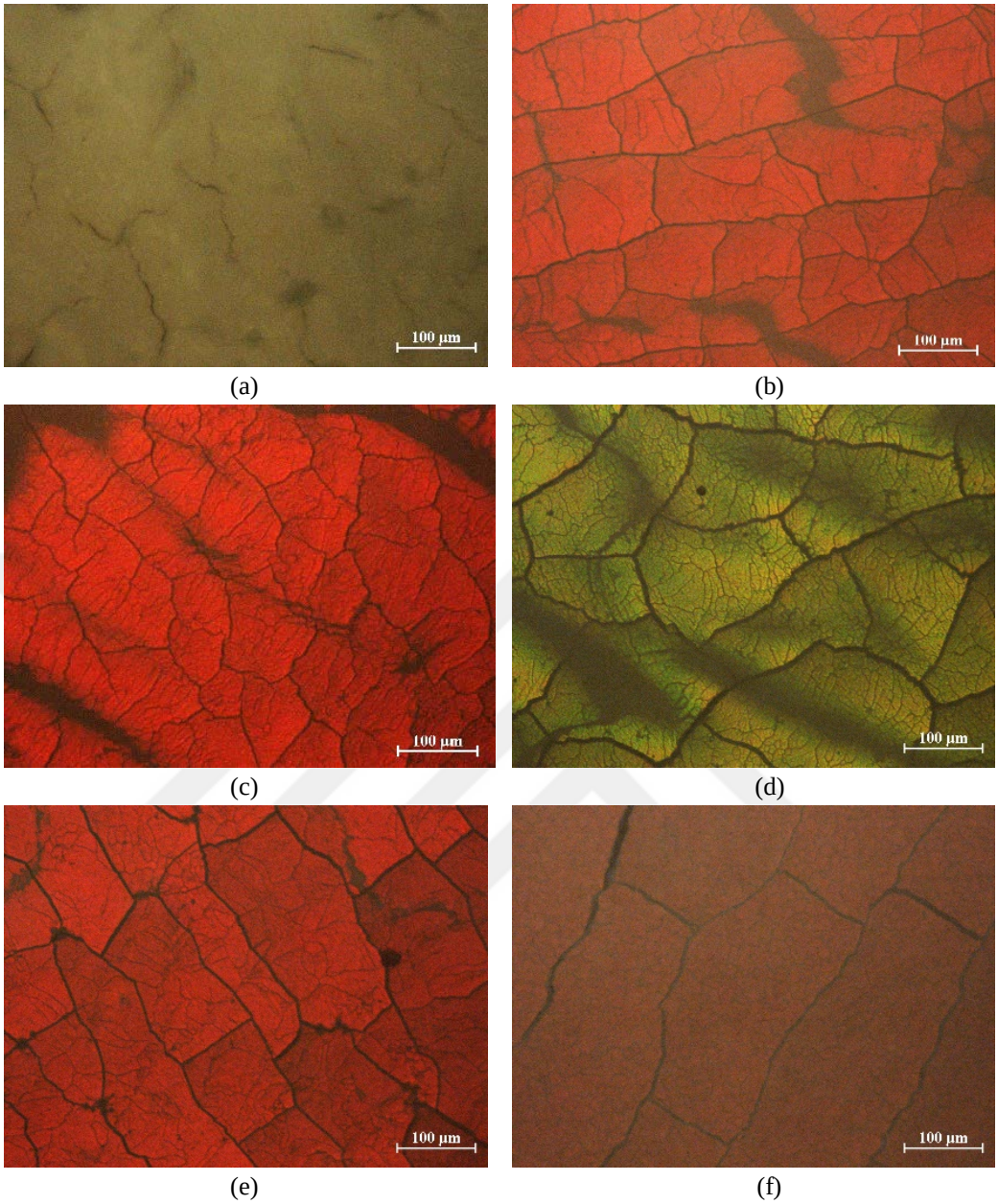

(a) (b)

(c) (d)

(e) (f)

Figure 4.5 Surface images of the (a) PMMA1, (b) PMMA2, (c) PMMA3, (d) PMMA4, (e) PMMA5, (f) PMMA6 opal PC coatings taken from optical microscope

PMMA1 and PMMA4 samples show a color mix of yellow and green flourish attract a great amount of attention when optical microscope images are interpreted in general. If we look at the UV-Vis reflectance spectra of these samples (Figure 4.4), the PMMA1 sample has a weak reflectance about 560 nm while the PMMA4 sample exhibits a powerful reflectance in the same wavelength region. Firstly, the question of why the PMMA1 sample exhibits a very light and wide peak should be answered. Morphology and regular arrangement problems of PMMA1 colloids could be seen as

the main reason, as discussed in the previous part. The color changes between opal PC coatings attributed to the variations at the dimensions of PMMA colloids. Though PMMA1 surface has small disrupted PMMA arrangement areas, this did not really changed the observed color. But yet, it can be concluded that the more uniformly ordered structures show the more clear peaks according to the reflectance measurements along with the formation of evident color formation. As a conclusion, yellow and red colors observed from PMMA opal PCs and have the sphere dimensions of 250-275 nm and 275-290 nm, respectively.

It can be stated that decreasing PMMA sphere size caused at the material color to a shift to lower wavelengths called blue shift while increased sphere size caused shifting to higher wavelengths called redshift. As an example, Yoo et. al. stated that as the particle size of the polystyrene colloids increased, the reflectance peak was red-shifted refer that the PBG was reduced as the colloidal particle size increased. They also achieved red and yellow colors from PS colloids have 280 nm and 250 nm, respectively (Yoo et al., 2016). All these color changes are based on the change at the distance between the spheres with the change in the colloid size related to the Bragg-Snell law (4.1) which was explained in Chapter 2 (Aguirre et al., 2010; Ge & Yin, 2011).

$$\lambda_{max} = 2d_{xxx}\sqrt{n_{eff}^2 - sin^2\theta}_0 \tag{4.1}$$

where λ_{max} is the wavelength of the reflectance peak maximum representing the photonic band gap position for PC systems, d_{xxx} is the space between planes, n_{eff} is the average refractive index of the PC structure consisting of PMMA particles and ambient air and θ is the incident angle between the normal axis of the material. The average center-to-center distance between spheres on the (11 1) planes is presented by the D, Eq. (4.1) simplifies to (4.2) give first-order Bragg diffraction from FCC (111) planes;

$$\lambda_{max} = 1.633D\sqrt{n_{eff}^2 - sin^2\theta}_0 \tag{4.2}$$

Because the D express center distances between building spheres, it decreases with decreasing PMMA sphere size while increasing with increased PMMA colloid size. That way, the wavelength of the PBG wavelength range shifts to the red color zone by the increasing colloid particle size, while the decreasing colloid particle size shifts it to blue. Thus, the reflectance and optical microscope results were given in Figures 4.4 and 4.5 seems to be logical. The obtained results proved that the opal PC coating colors can be controlled by the PMMA particle size.

4.2 Effect of Ce or Eu dopants on properties of SiO_2 Inverse Opal Photonic Crystal Coatings

4.2.1 Thermal and Structural Characterizations

In order to scrutinize thermal properties of the dried SiO_2 based gel samples, thermogravimetric and differential thermal analysis were particularly performed. The relevant analyses were carried out with heating rate of 5 °C /min. in the temperature range of 25-900 °C under atmosphere conditions. The obtained results were processed and the DTA-TGA diagrams were drawn and presented in Figure 4.6. According to DTA results of the un-doped and Ce doped samples, it is observed that all Ce doped samples show an endothermic peak at around 100 °C and exothermic peak at almost 380 °C according to Figure 4.6 (a). It can be noted that the peak at around 100 °C is an endothermic peak and corresponding to the elimination of physically adsorbed water from the body (Skorodumova, Semchenko, Goncharenko, & Tolstoi, 2001). The exothermic peaks of the PC-SiO_2, PC-C25, PC-C50, PC-C100 and PC-C200 samples are respectively placed at 343.56, 379.98, 391.63, 397.15 and 389.79 °C, which reflect combustion temperatures.

This exothermic reaction in the temperature range of 350 and 450 °C is related to the removal of chemically adsorbed water and the thermal dissociation of the organic groups such as CH_3 (indirectly oxidation), as explained in details in Refs. (Bhosale et al., 2009; Skorodumova et al., 2001). It is significant issue that Ce dopant strongly affects the exothermic peaks. According to the general view, increasing Ce dopant

amount gave slightly rise to shifting of exothermic peak to higher temperatures. The reason for this phenomenon should be the increase of organic structures arise from the chemical precursors used for Ce doping. Upon examining TGA curves from Figure 4.6 (b), it can be determined that a weight loss of the un-doped PC-SiO_2 sample is 23.88%, while Ce doped samples have about 26%. In other words, the Ce doping caused an increase in the weight loss. It is a significant issue that a major part of their weight losses is observed at temperatures between 350 and 450 °C on account of combustion of C coming from organic precursors, solvent and chelating agent.

It can be seen from Figure 4.7 (a) that Eu doping causes more remarkable changes in DTA results than the Ce doping. The first observed phenomena is the endothermic peak, in which the physical water moves away, shifts to higher temperatures proportionally with the Eu dopant ratio. The observed exothermic peak, about the 300-400 °C temperature range, belongs to the un-doped PC-SiO_2 sample, shifted to 350-550 °C temperature range and enlarged by the Eu doping corresponding to increased oxidation. Moreover, two exothermic peaks are observed at 367.69 and 485.00 °C, corresponding to the 0.25% Eu doped PC-E25 sample. These variations are related to the organic structures of Eu precursor similar to Ce doping. These changes at the thermal properties are very remarkable, though the doping ratio is very low such as 0.5-2%. When TGA results of the Eu doped samples were analyzed (Figure 4.7 (b)), Eu doping did not cause a change such as a weight loss increase in contrast to Ce doping. Nevertheless, the weight change completion that is normally about 400 °C was shifted to 500 °C by Eu doping with expanding the exothermic reaction zone. The phenomena occurred in the temperature range of 450 and 600^{o}C belongs to chemical oxidation process.

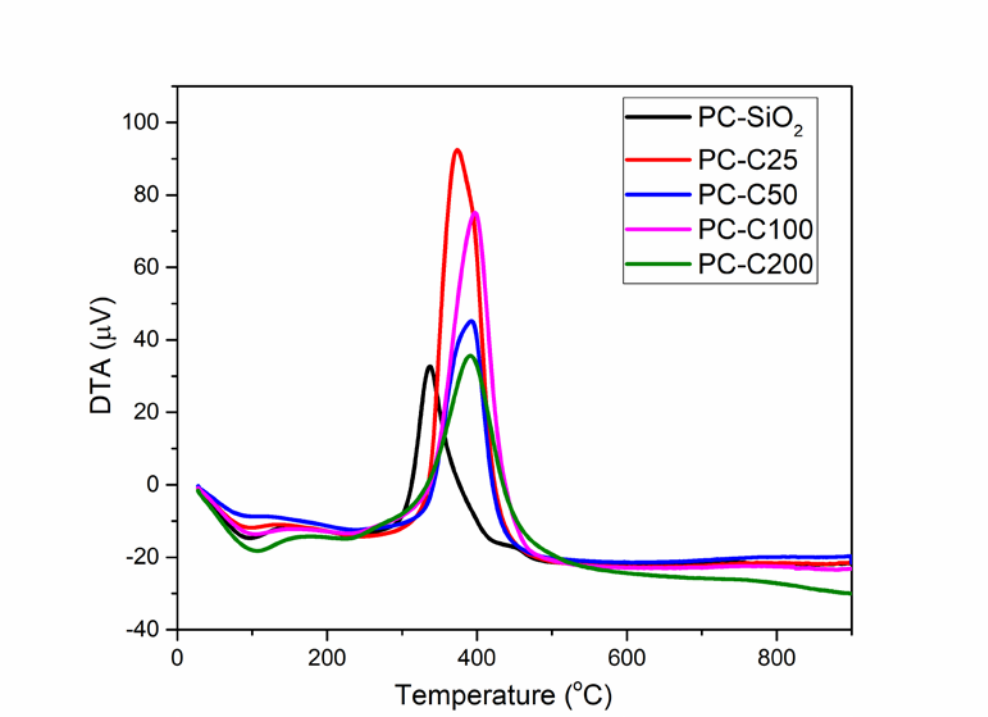

(a)

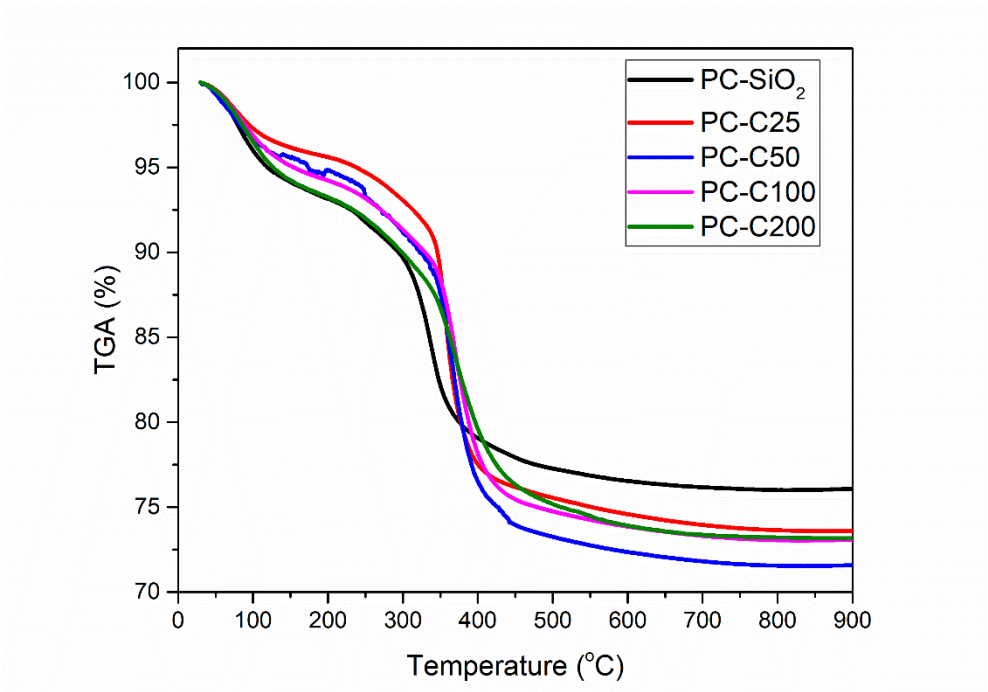

(b)

Figure 4.6 (a) DTA and (b) TGA diagrams of the un-doped and Ce doped silica inverse opal PC coatings, respectively

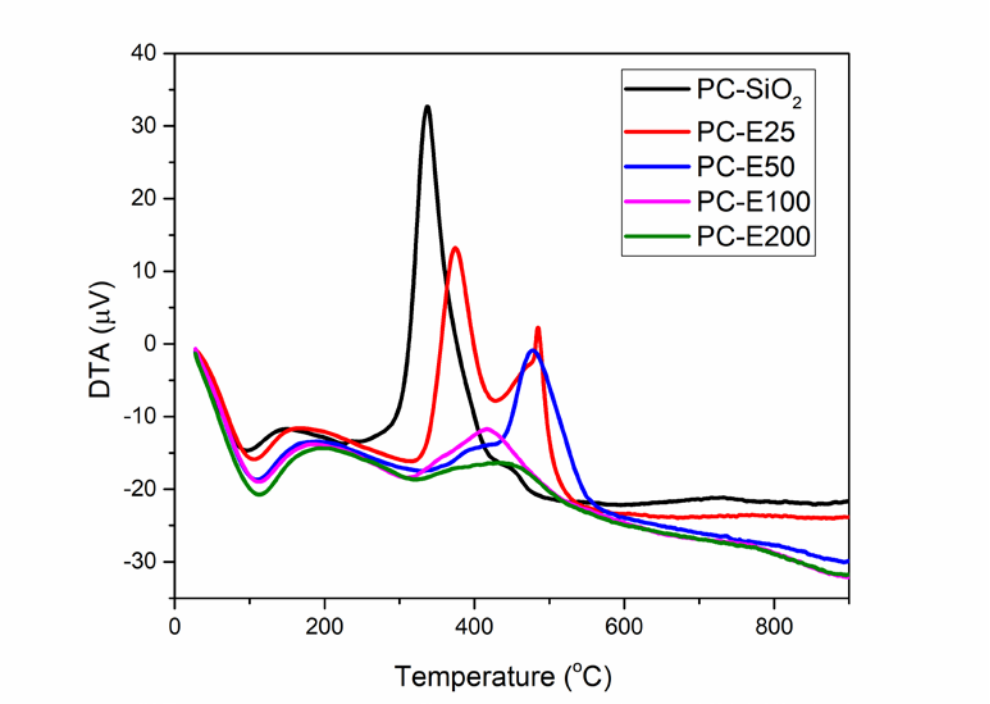

(a)

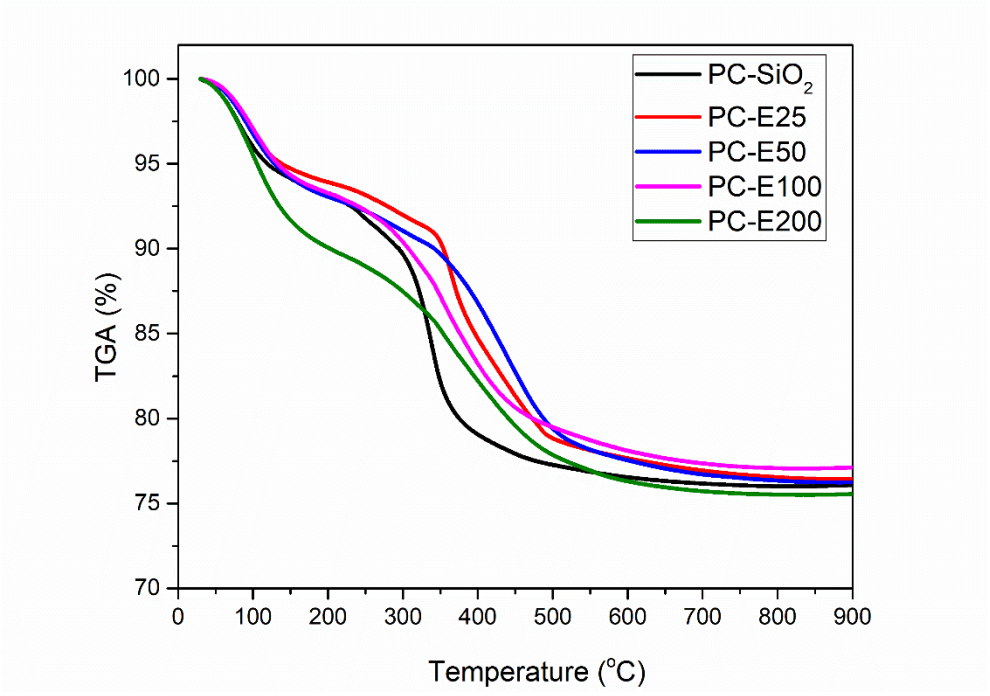

(b)

Figure 4.7 (a) DTA and (b) TGA diagrams corresponding to un-doped and Eu doped silica inverse opal PC coatings, respectively

Temperature regimes of drying and heat treatments were determined as a combination of DTA-TGA results. We simulated the results to determine temperature regimes of drying and heat treatment. The samples were gradually dried at 100°C for 60 min and 300°C for 60 min and subsequently heat-treated at 550 °C for 60 min in air (Figure 3.6). The samples were stored in a dry atmosphere in order to further analyze for their characteristic structure and special properties.

XRD patterns of the PC-SiO_2, PC-C100, PC-C200, PC-E100, and PC-E200 inverse opal PC coatings are presented in Figure 4.8. It is obvious that SiO_2 based all PC coatings have the amorphous phase. Crystallization of SiO_2 structure could be obtained at a high calcination temperature such as about 1100 °C at the sol-gel production method (Skorodumova et al., 2001). Because of the mentioned literature (Skorodumova et al., 2001) and DTA-TGA results, the calcination/heat-treatment step was carried out at a quite low temperature such as 600 °C due to the fact that high calcination temperature could lead to deterioration of the regularity of the inverse opal PC structure. That is way; the structure becomes the amorphous phase with randomly arranged Oxygen (O) and Silicon (Si) atoms. It can be mentioned that Ce and Eu doping processes caused some variations on XRD patterns. The sharper hump belongs to the un-doped PC-SiO_2 inverse opal PC coating gets widen as can be individually seen from Figure 4.8 by both Ce and Eu dopants. According to these results, it is important to express here that this widening observed at the hump means the crystal structure gets more amorphous. It is observed that the doping of Ce provides the SiO_2 structure more amorphous than the Eu doping. A possible explanation for this effect could be the difference between atomic or ionic diameters of the matrix and dopant elements. In this way, the regular arrangement of Si and O atoms in SiO_2 lattice becomes harder. Consequently, it can be put forward that increasing Ce and Eu dopant ratios make the amorphous peak more widen and increases the irregularity.

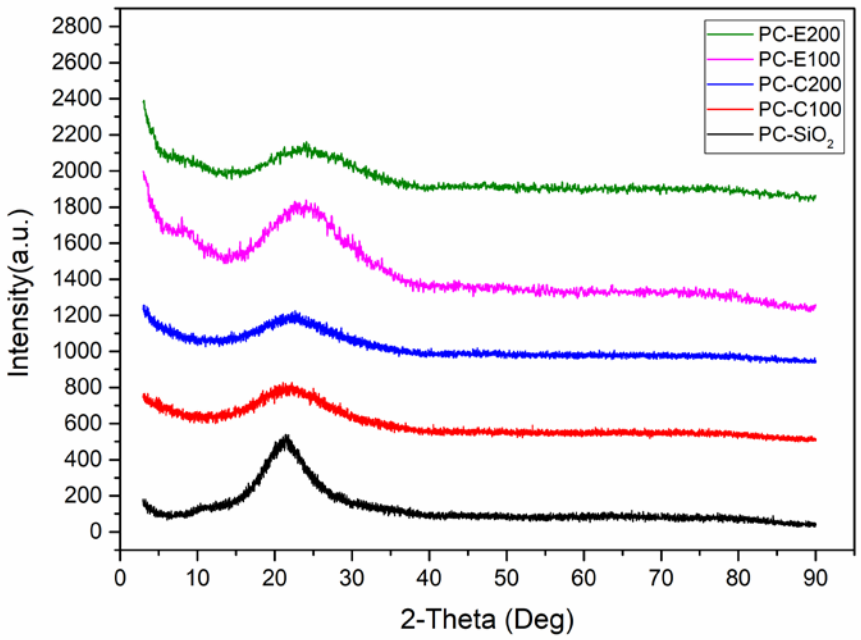

Figure 4.8 XRD patterns of the un-doped and Ce or Eu doped inverse opal SiO_2 PC coatings

The elemental species, as well as their oxidation states, were characterized by the X-ray photoelectron spectroscopy (XPS) evaluation. The detailed XPS analysis results are gathered and presented in Figure 4.9. Si, O and C elements seem to be mutual for all samples, as can be seen from Figure 4.9 (a) where general XPS surveys of the inverse opal PC coatings are presented. In order to characterize Ce and Eu dopants, high-resolution XPS scans of PC-C200 and PC-E200 samples containing maximum amounts of related dopants were analyzed. Samples have a small carbon peak that can be observed from Figure 4.9 (a), is likely corresponding to the carbon residue not burned off entirely after the calcination process or existence of atmospheric carbon (Bhosale et al., 2009). This carbon peak was used for calibrating the peak positions of XPS spectra (Bhosale et al., 2009). The observed Si and O elements except the carbon element are related to the SiO_2 structure, which was aimed to produce. The determination of the oxidation states of the components was carried out by the electron binding energy (BE) values (Radnik et al., 2003).

High-resolution XPS scans belong to the Ce and Eu doped inverse opal PC samples over Si and O are given in Figure 4.9 (b-c) and (d-e) respectively. As can be seen from

Fig. 4.9 (b-c), the main Si peaks of the Ce and Eu doped inverse opal PC samples are located between the binding energy (BE) values of 102.44 eV-108.23 eV and 103 eV-105 eV respectively. The oxidation state of the Si is found as Si^{4+} according to these BE values (Bhupinder Singh, 2016; Sublemontier et al., 2014). This means the material has the O-Si-O bonds and is fully oxidized in the SiO_2 structure (Y. Jiang et al., 2017). According to Figure 4.9 (d-e) the binding energy peaks of the Ce and Eu doped inverse opal PC coatings placed around 531-534 eV and 531 eV, respectively, that approves the existence of O^{2-} ion in the SiO_2 structure (Yildirim et al., 2019).

Some minor variations at the Si 2p and O 1s peaks can be noticed for doped inverse opal samples. For instance, Ce doping in a small amount such as 0.5 and 1% caused shifting to higher BE values at the Si 2p and O 1s peaks while shifting to lower BE values (about 2 eV) is observed for 2% Ce doped sample. However, the doping of Eu did not lead a change as much as Ce did. Eu doping caused a shifting to lower BE values (approximately 1 eV) at the O 1s peak while it did not bring along any change at the Si 2p peak. The XPS peak shift, known as the chemical shift is basically related to the oxidation state variation of the concerned element. Higher binding energy values express higher oxidation states (Radnik et al., 2003). When BE values shifted to lower

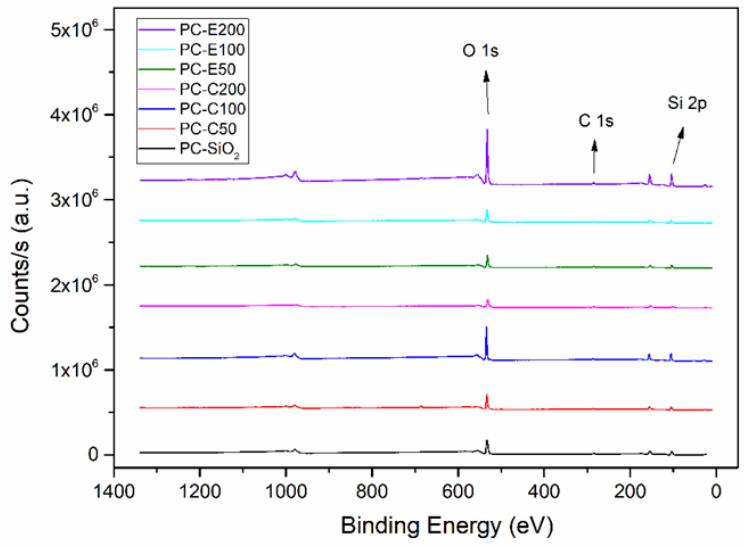

(a)

Figure 4.9 (a) General XPS results of the inverse opal PC coatings. High-resolution XPS scans of Ce or Eu doped PC coatings over (b-c) Si 2p and (d-e) O 1s. XPS scans over (f) Ce 3d and (g) Eu 3d dopant peaks of PC-C200 and PC-E200 samples

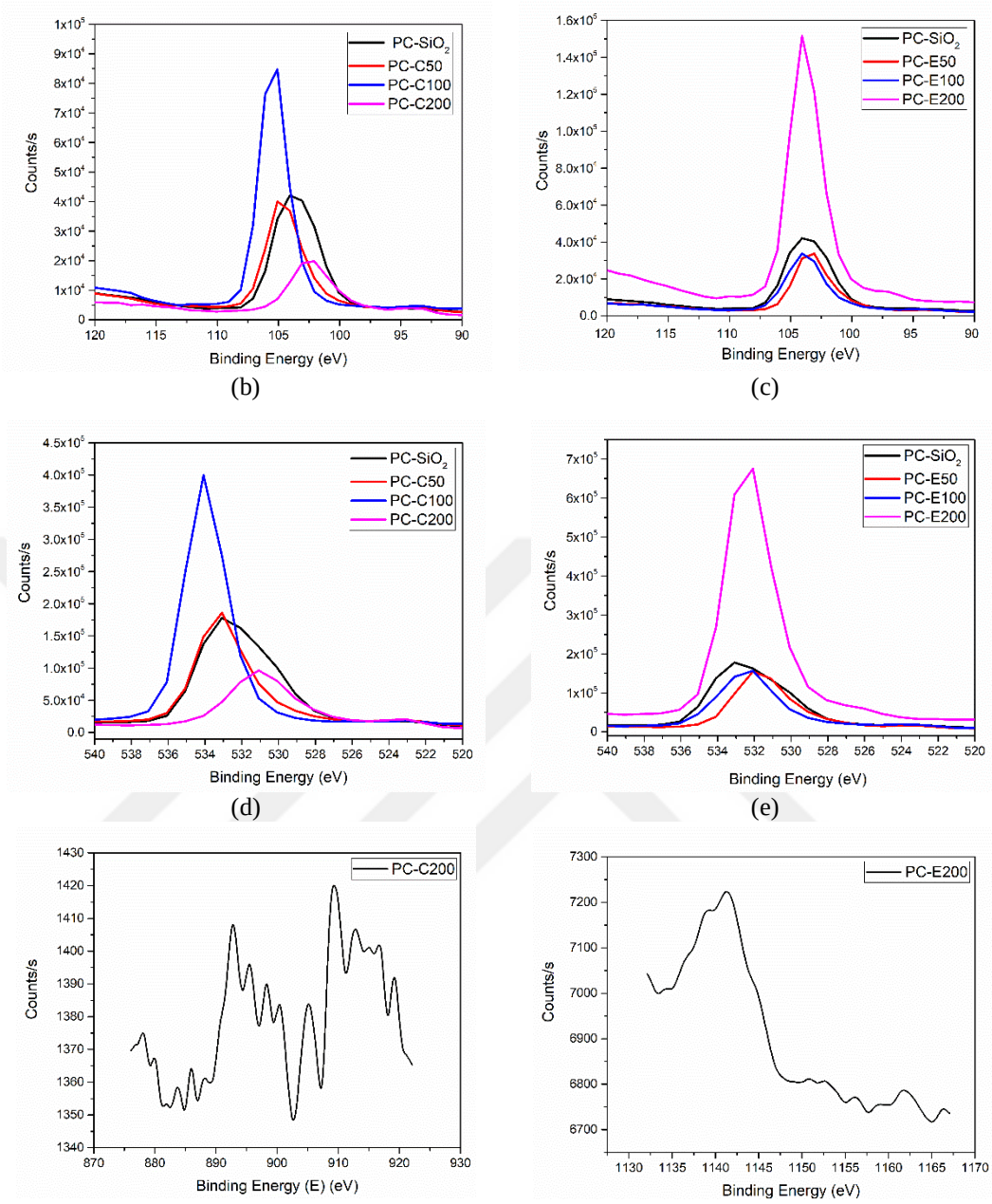

Figure 4.9 continues

values for Si^{+4} ions means that electrons bound to the oxygen and silicon species migrate to the oxygen vacancies and provide later serving as electron traps. Moreover, the shifting at the O 1s should be concerned to the electron transfer into the oxygen vacancies (Papageorgiou et al., 2010; Yew et al., 2019).

Detailed XPS spectra of the PC-C200 and PC-E200 coating samples are given in Figure 4.9 (f) and (g) respectively, to determine oxidation states of the Ce and Eu dopants. Samples with maximum dopant were taken into account because elements with low dopant ratios cannot be detected by XPS analysis. Ce 3d doublet peaks of PC-C200 inverse opal sample located around 893 eV and 908 eV are attributed to Ce^{3+} and Ce^{4+} oxidation states (Hernandez et al., 2018; Mekki, 2005b; Wang et al., 2016). When the detailed XPS scan over Eu 3d of the PC-E200 sample is examined from Figure 4.9 (g), it is seen that Eu dopant exists in SiO_2 structure as Eu^{3+} ion, consistent with the literature peaks about 1141 eV and 1162 eV (Calderon-Olvera et al., 2018; Korake et al., 2014; Yang et al., 2011).

4.2.2 Morphological Characterization

In order to examine morphologies of the samples, SEM images of un-doped, Ce or Eu doped SiO_2-based PC coating samples in the form of thin film (TF) and PC form are depicted in Figure 4.10. Thin-film coating samples have surfaces with many cracks according to Figure 4.10. Upon interpreting the visible results of SEM, it is significant issue to bear in mind that these cracks demonstrate changes depending on the amount of the dopants. Broadly speaking, it is observed that surface morphology of TF coatings are smoother and have fewer cracks at low dopant ratios of 0.25% and 0.50% for Ce dopant while at high dopant ratios of 1% and 2% for Eu dopant.

It can be said that all inverse opal PC coatings have honeycomb like surface morphology. The ordered structure also presents in the lower layers as can be seen from the pore cavities of inverse opal structure on the surfaces. It is proved that the remaining silica based walls are obtained successfully by removing opal PMMA spheres from the structure and extends through the whole three-dimensional network. The thickness of the silica-based walls could be measured about 20-30 nm while the size of the pores is about 200 nm. Due to the three-dimensional structure of the walls in these dimensions picks out an extremely increased surface area. Hereby, these inverse opal materials can be used in many areas to increase efficiencies with the high surface area (Yang et al., 2017; Yu et al., 2018)

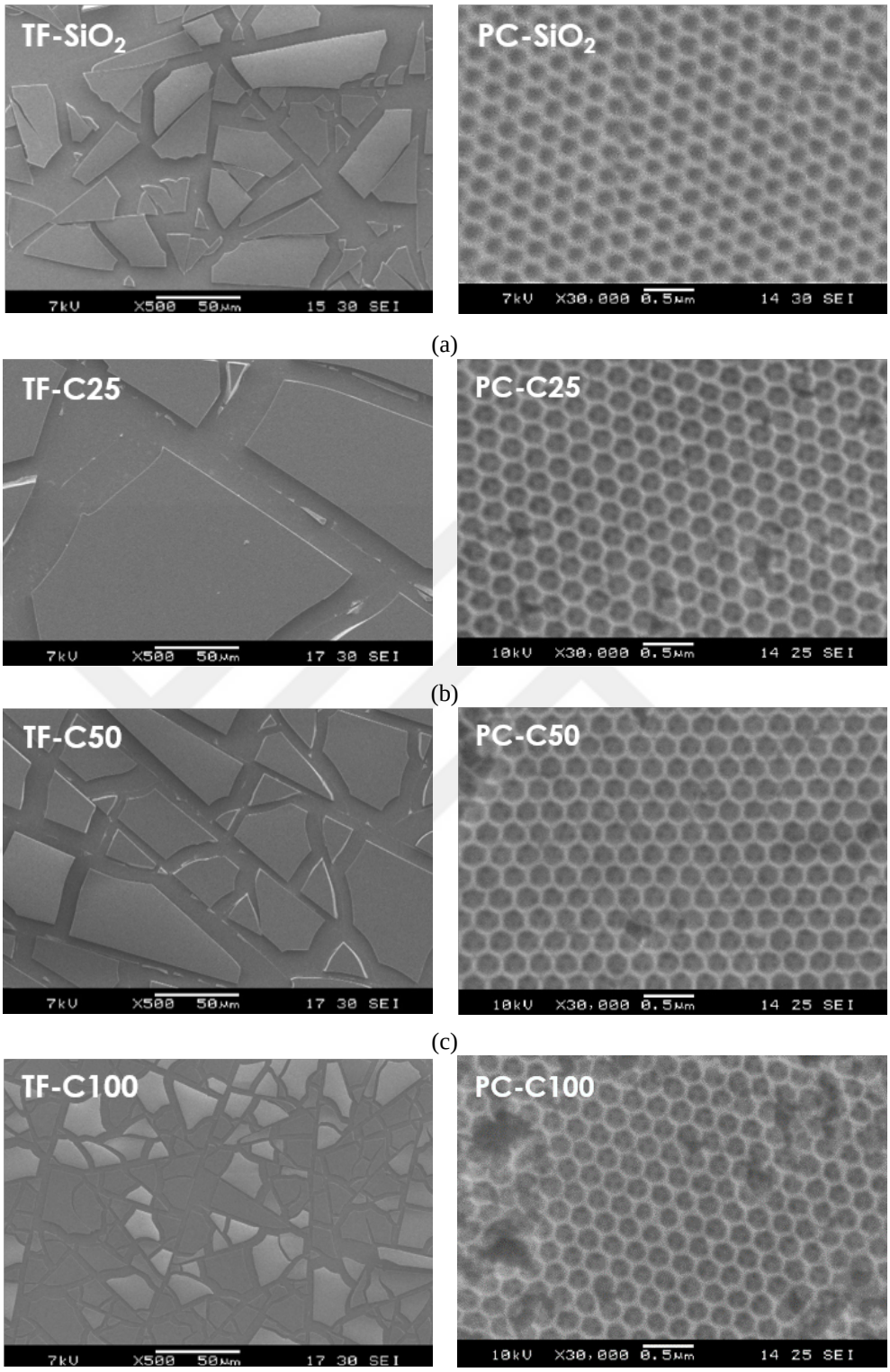

Figure 4.10 SEM images of the (a) un-doped, (b) 0.25%, (c) 0.50 %, (d) 1%, (e) 2% Ce doped; (f) 0.25%, (g) 0.50 %, (h) 1% and (i) 2% Eu doped SiO_2 based coating samples in the thin film (TF) and PC forms

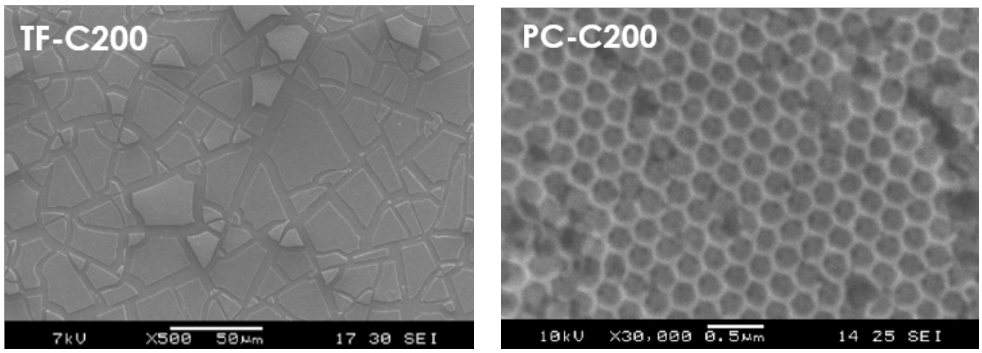

(e)

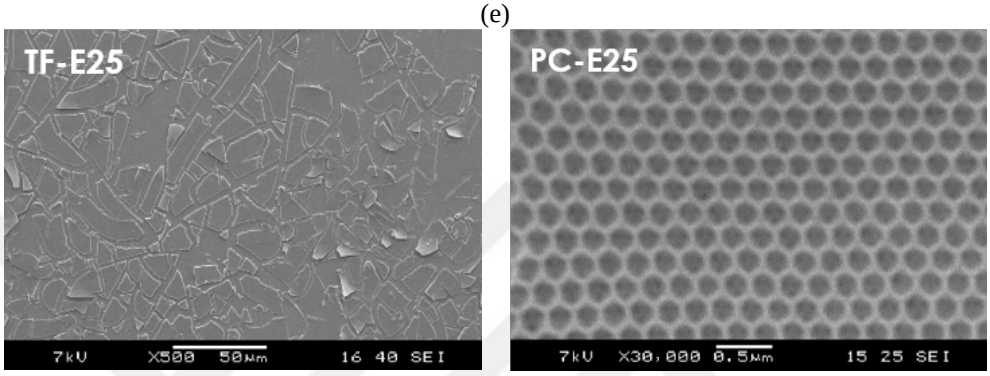

(f)

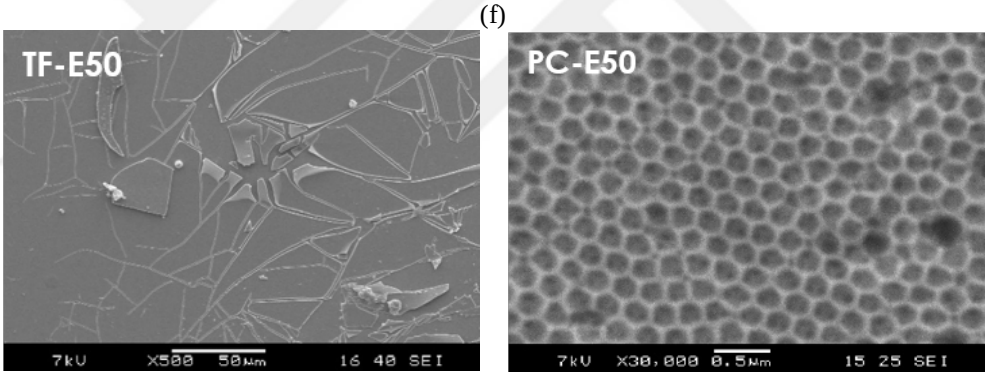

(g)

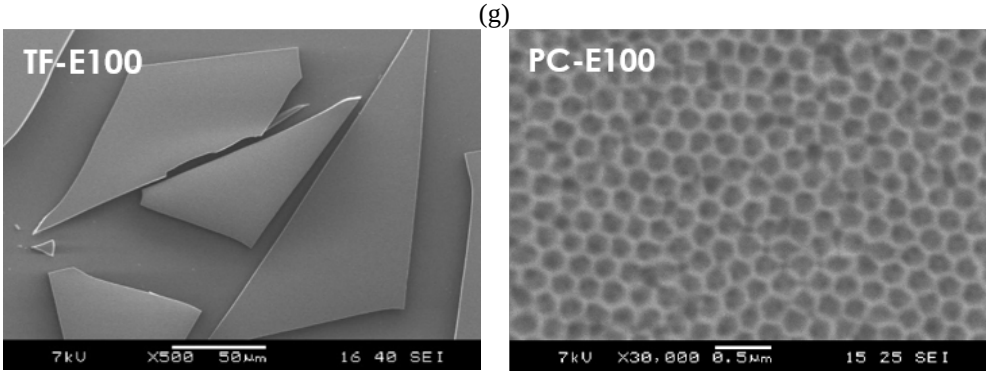

(h)

Figure 4.10 continues

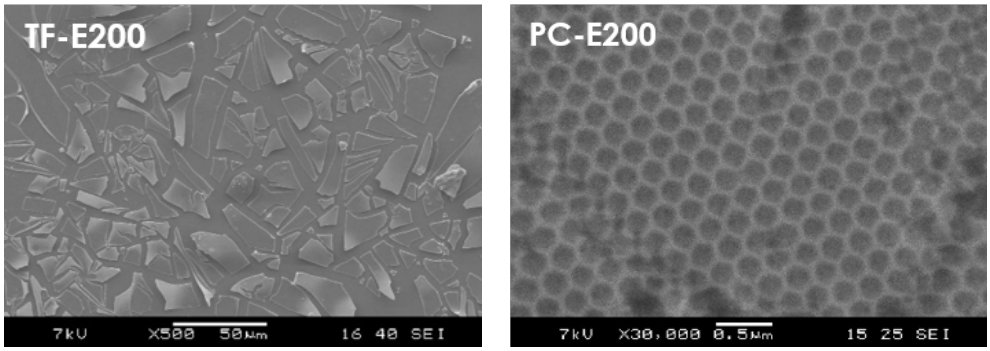

(i)

Figure 4.10 continues

If the PC SEM images in Figure 4.10 are examined, the first thing draws attention about the inverse opal photonic crystal coatings is that some degradations are observed at the Ce or Eu doped coating surfaces. It can be seen that there is no significant problem with the regular arrangement on the surface of the Ce doped inverse opal PC coating samples (Figure 4.10 (b)-(e)), while there are some deteriorations such as crack at the SiO_2 walls in small regions. However, it can be seen that the ordered porous structure is disrupted for Eu doped inverse opal PC samples (Figure 4.10 (f)-(i)), notably the PC-E50 and PC-E100 samples. Relatedly, it can be noticed that the best morphologies for both Ce and Eu doped inverse opal PC samples are obtained at the samples with the lowest dopant ratios. Moreover, it can be observed that there is a correlation between thin film and inverse opal PC surface morphologies. It can be concluded that the best thin-film quality and regular surface morphology are obtained for 0.25% Eu doped coatings samples such as TF-E25 and PC-E25.

4.2.3 Optical Characterizations

The UV-Vis reflectance graphics of the Ce or Eu doped SiO_2 based thin film and PC coatings are given in Figure 4.11. The continuous curves express photonic crystal coatings while dashed lines represent thin films in Figure 4.11. Optical microscope images were taken from these coating sample surfaces in order to support reflectance results. Optical microscope images of the all coatings are presented in Figure 4.12. The optical images of the thin films are placed left side of Figure 4.12 while inverse opal

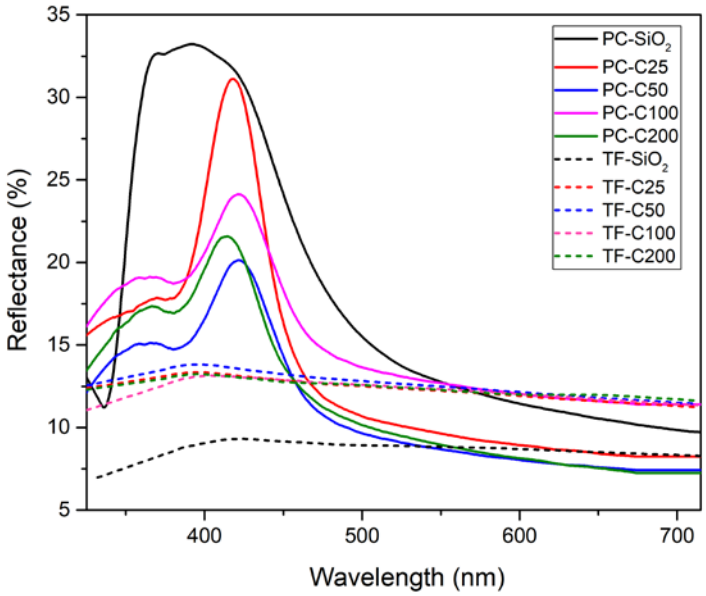

(a)

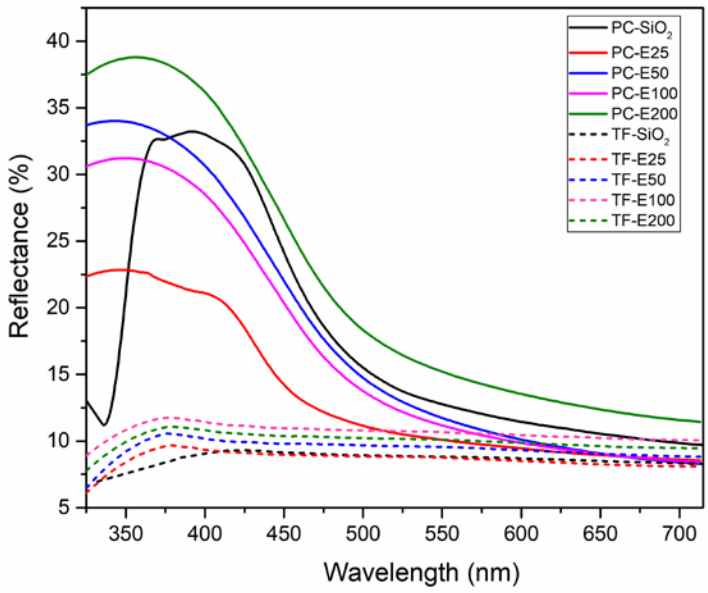

(b)

Figure 4.11 UV-Vis reflectance spectra of the (a) Ce and (b) Eu doped thin film and PC coatings

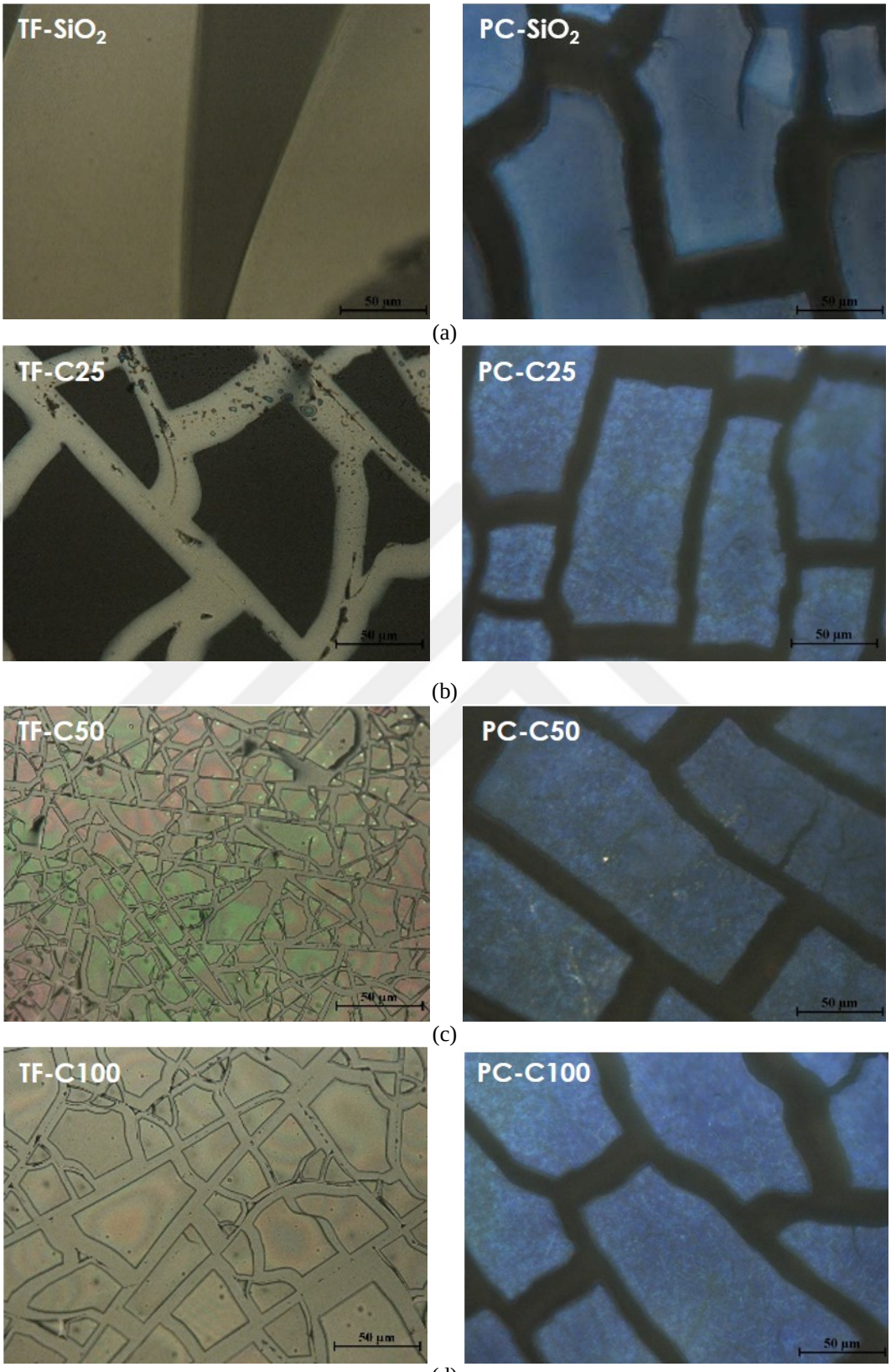

Figure 4.12 Optical images of the (a) un-doped, (b) 0.25%, (c) 0.50 %, (d) 1%, (e) 2% Ce doped; (f) 0.25%, (g) 0.50 %, (h) 1% and (i) 2% Eu doped SiO_2 based coating samples in the thin film and PC forms

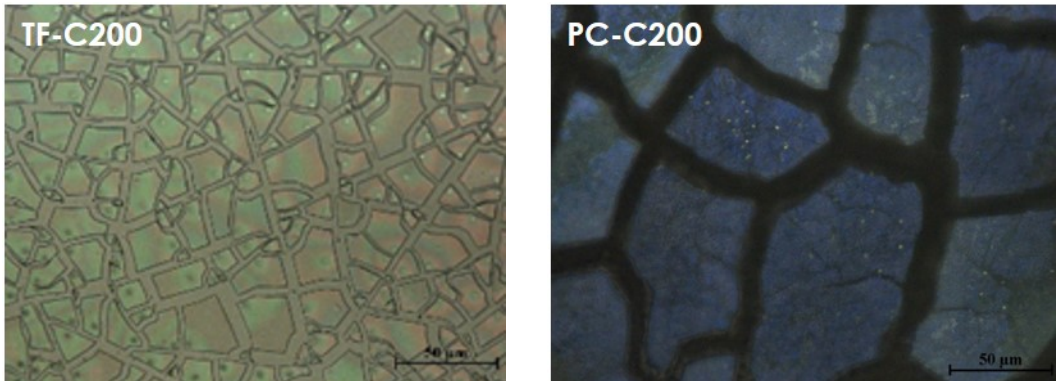

(e)

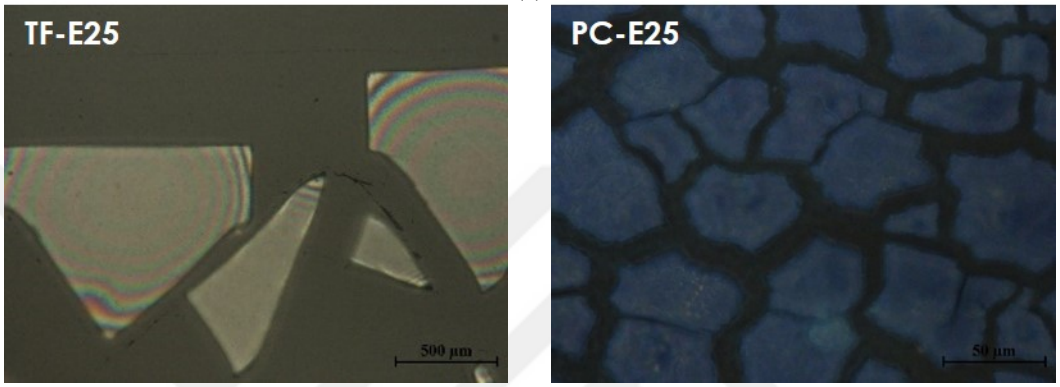

(f)

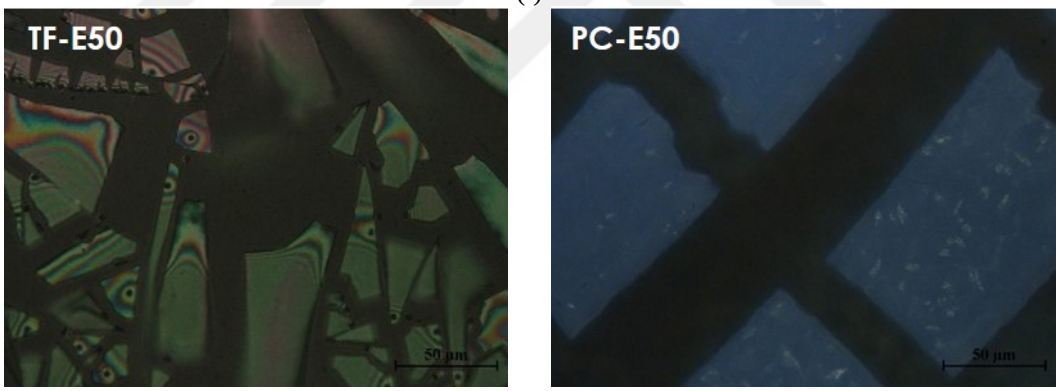

(g)

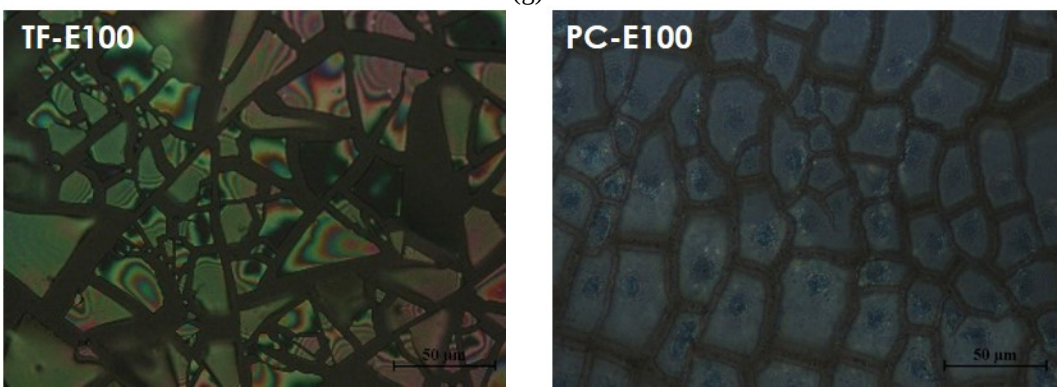

(h)

Figure 4.12 continues

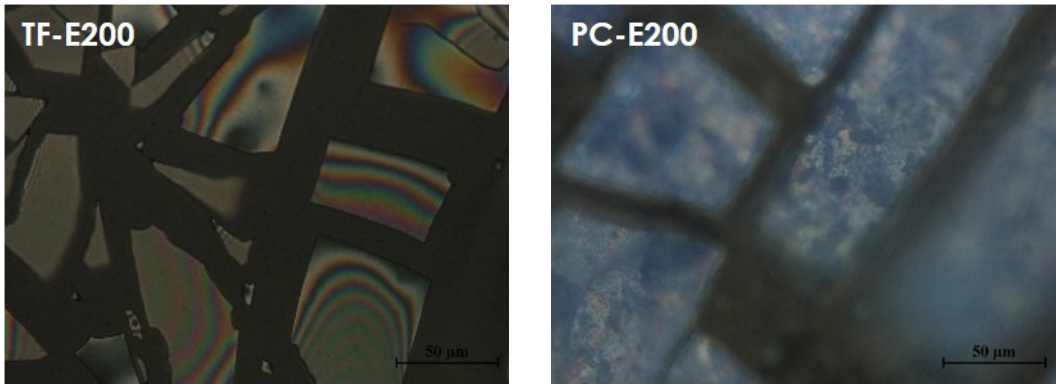

(i)

Figure 4.12 continues

PC coatings are located the right part to determine the effect of PC structure. The results of the UV-Vis reflectance and optical microscope images would be discussed coherently according to Figures 4.11 and 4.12. Firstly, the un-doped inverse opal PC SiO_2 coating has a broad peak of about 400 nm and has a wide range between 350 and 450 nm as can be observed from Figure 4.11. It should be noted that such a characteristic peak do not have a 100% reflectance ratio, could be called as pseudo photonic bandgap (pPBG) (Aguirre et al., 2010; Waterhouse & Waterland, 2007; Dalmis et al., 2020). The PC-SiO_2 coating exhibits blue and purple colors as can be observed from Figure 4.12 (a), due to fact that this pPBG located in the purple color region and prolonged to the blue color region.

It can be seen that pPBG peak is affected by the Ce and Eu dopants according to the Figure 4.11. The pPBG peak of the PC coatings shifted towards the higher wavelength values by Ce doping according to Figure 4.11. Nevertheless, it cannot be overlooked that the reflectance ratio is decreased by Ce doping. Also, the wide reflectance peak of the un-doped PC SiO_2 coating turn out a narrower peak by Ce doping. Thus, the observed color seems more clear and vivid due to the increased resolution. It can be proved with the optical image in Figure 4.12 (b-c) that the purple color becomes clearer by the narrowing peak in the purple color range by Ce doping. Additionally, pink and green colors can be observed from Ce doped thin films especially at PC-C50 and PC-C200 in some regions of the structure. The lack of the related violet-blue colors on the thin films proves that the violet-blue colors obtained by the inverse opal PC structure. That kind of pigment-free color formation is called

structural color (Dalmis et al., 2019b; Dalmis et al.,2019c; Kim et al., 2018). There is a big difference between reflectance graphs of Eu and Ce doped inverse opal coatings is observed in Figure 4.11. Eu doping caused slight changes at the reflectance rates according to Figure 4.11 (b). As can be observed from Figure 4.11 (b), the reflectance ratios of the 0.25%, 0.50%, and 1% Eu doped inverse opal PC coatings were reduced, while the ratio of the 2% Eu doped inverse opal PC-E200 coating sample was increased. Besides, dissimilar to Ce doping Eu doping caused a blue shift at the reflectance peak of the inverse opal PC coatings. Due to the blue shift, the reflectance peak-end of the inverse opal PC samples moves from the blue the color region to the violet color. In this way, the violet color becomes more dominant as can be observed with the Eu doped PC coatings except for PC-E200 in Figure 4.12 (f-h). Yet, it can be seen that the blue color is more predominant on the surface of the PC-E200 coating (Figure 4.12 (f-i)). Eu doping affects the surface color of the thin film surfaces as some color formations such as pink, yellow, and green are observed from their surface (Figure 4.12 (f-i)). Apart from these dopant effects, another thing that may cause color change could be to the small size variations at the porosity and SiO_2 wall sizes (Zhao et al., 2017).

4.3 Results of the Sm or Tb doped SiO_2 Inverse Opal Photonic Crystal Coatings

4.3.1 Thermal and Structural Characterizations

Thermal analysis of the dried sol-gel samples were performed by DTA and TGA analysis. The DTA-TGA curves of Sm or Tb doped SiO_2 based samples are presented in Figures 4.13 and 4.14, respectively. According to the DTA results of the Sm doped samples (Figure 4.13 (a)), it can be understood that the un-doped SiO_2 sample displays an endothermic and exothermic peak about 99.61 °C and 343 °C respectively whilst Sm doped samples have an endothermic peak about 110 °C, and three exothermic peaks approximately 200, 360 and 470 °C. Keeping in mind that the endothermic peak that is mutual for all samples at about 100-115°C is corresponding to the removal of the physically adsorbed water from the body (Hu & Liu, 2013).

Note that the exothermic peak located approximately 360 °C is related to the thermal decomposition of the organic compounds (CH_3) and desorption of the chemically adsorbed water. It should be noted that, as a result of this investigation, the Sm doping process strongly affects the exothermic peaks. This influence is so high that new peak formations could be observed at the DTA graphs in Figure 4.13 (a). Additional new peaks created by the Sm doping were observed about 200 °C and 470 °C. The peak located 470°C is related to the oxidation phenomenon. Generally speaking, increased dopant amounts caused shifting at all DTA peaks towards higher temperature values. It can be stated out that all these changes in thermal properties can be attributed to the addition of the Sm precursor (Samarium (III) oxide) used for Sm doping.

The peak located about 200 °C concerned about the removal of chemical water comes from the Sm precursor while the peak about 470 °C refers to the disposal of organic structures come from the precursor again. All Sm doped samples have a weight loss of about 24% except PC-S200 sample according to the TGA curves given in Figure 4.13 (b). The PC-S200 sample, out of this generalization, has a weight loss of 27.98%. It is an important point major part of the weight loss takes place about 400 °C where the main exothermic reaction takes place.

It is observed that Tb doping process gives rise to similar changes with the Sm doping according to the DTA results of the Tb doped Silica samples (Figure 4.14 (a)). The endothermic peak located about 110 °C, in which the physical water disappears, shifts towards higher temperature values proportional to the Tb dopant amounts according to Figure 4.14 (a). Thermal decomposition of the organic groups comes from Si precursor (TEOS) is related to the exothermic peak located at 360 °C while the additional new peaks around 200 °C and 470 °C, are related to the removal of chemical water and organic groups basically from the Tb precursor (Terbium (III) nitrate hydrate). It can be observed that the PC-T200 sample does not have an exothermic peak at 360 °C while instead presents a single exothermic peak about 467 °C. Normally there are two peaks like other samples, although the other high-intensity peaks appear to be single peaks in the spectrum.

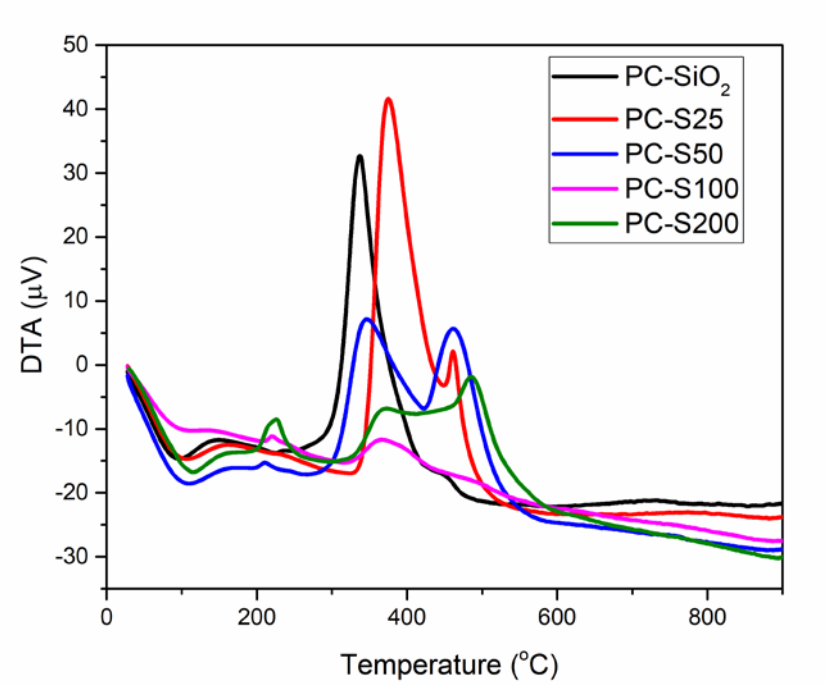

(a)

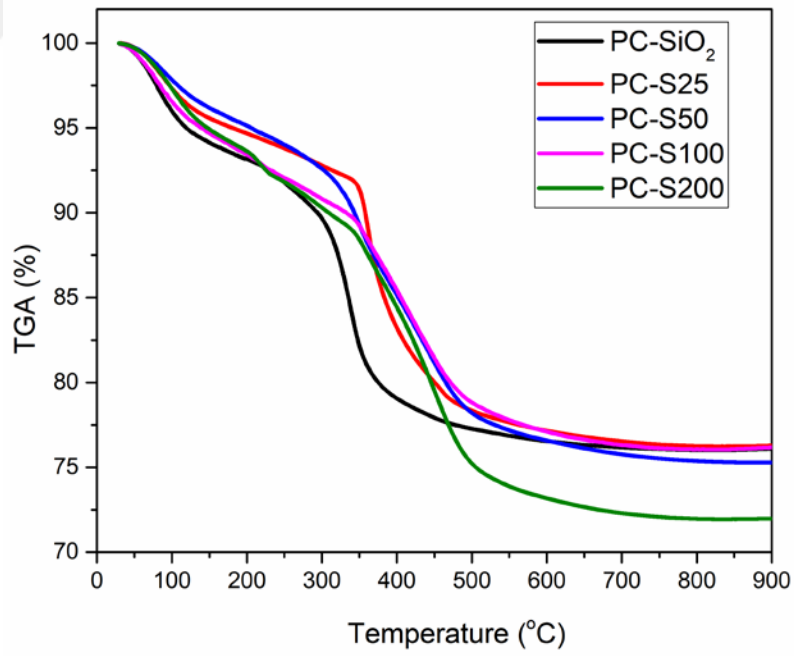

(b)

Figure 4.13 (a) DTA and (b) TGA diagrams of the un-doped and Sm doped silica inverse opal PC coatings

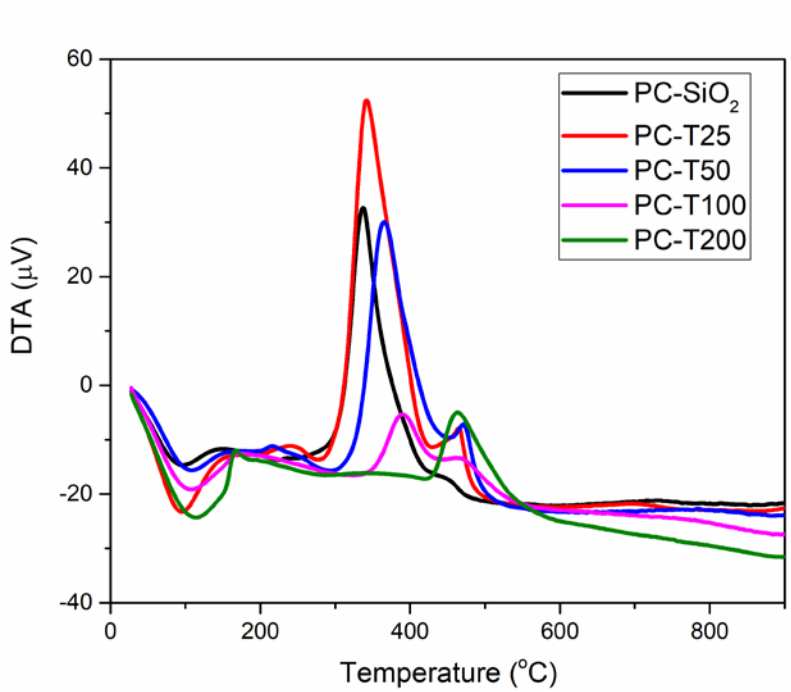

(a)

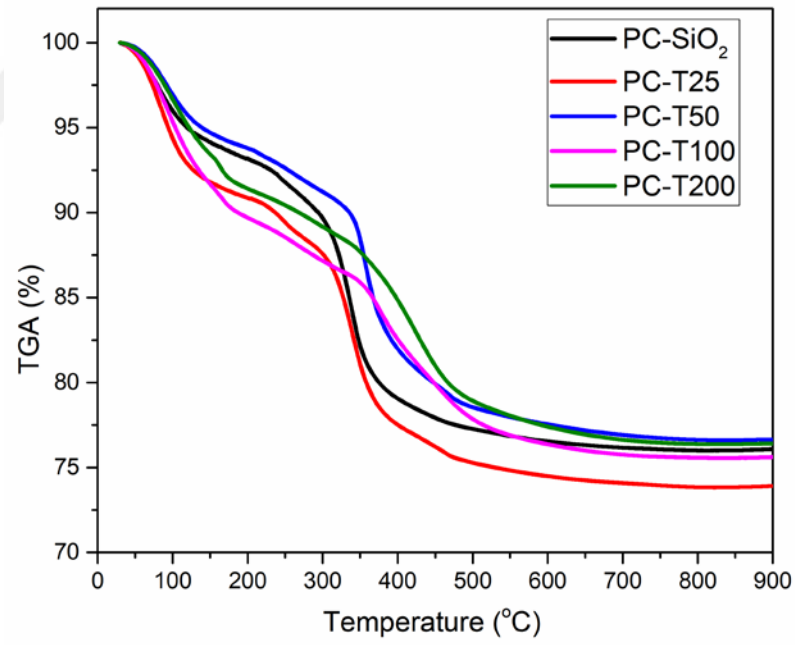

(b)

Figure 4.14 (a) DTA and (b) TGA diagrams of the un-doped and Tb doped silica inverse opal PC coatings

It can be seen that Tb doping did not cause an important weight loss chance except PC-T25 sample. If the un-doped SiO_2 and the PC-T25 samples are compared, it can be concluded the mass loss increased from 23.38 to 26.07% with 2% Tb doping. Another result is that the finishing temperatures of the mass losses were shifted to higher temperatures for both doping processes. Finally, even though the doping ratios are very low such as 0.5-2%, these thermal property variations are very important results about thermal characteristics.

XRD patterns of the some un-doped, Sm or Tb doped SiO_2 based inverse opal PC coatings are presented in Figure 4.15. All silica-based inverse opal PC coatings have the amorphous phase according to XRD patterns in Figure 4.15. It is well-known that in order to crystallize SiO_2 structure in the sol-gel production method high calcination temperatures such as 1000-1200 °C are required (Skorodumova et al., 2001). However, the high calcination temperature may cause degradation at the ordered inverse opal PC morphology. Calcination process performed at 600 °C has caused the formation of an amorphous phase consists of randomly arranged Si and O atoms.

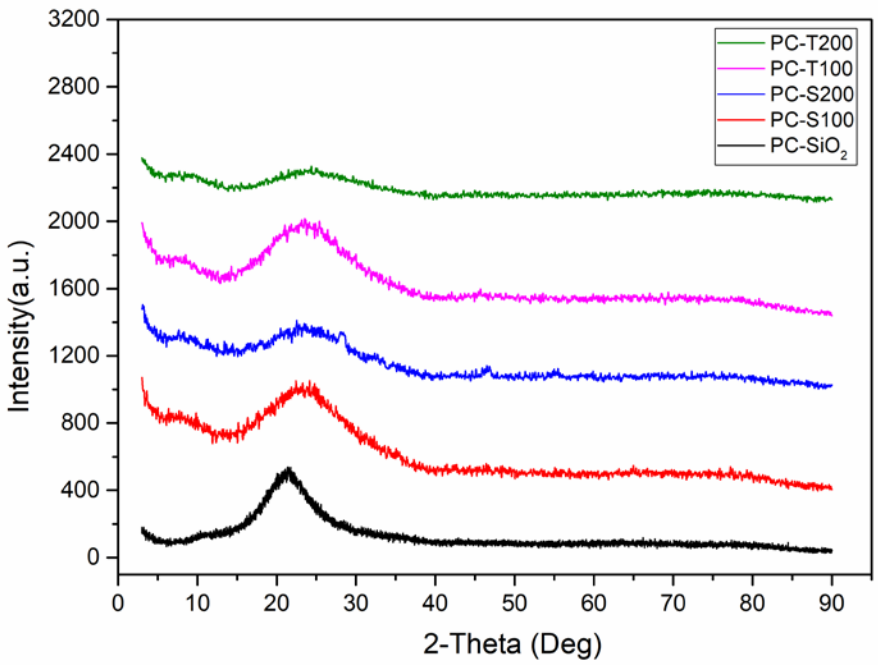

Figure 4.15 XRD patterns of the un-doped, Sm or Tb doped SiO_2 based inverse opal PC coatings

It can be found that Sm or Tb doping into this amorphous structure influences the structure of the body. As for Figure 4.15, the sharpness of the XRD peaks decreases with doping both Sm and Tb atoms and the peak was widened while the un-doped SiO_2 sample has the sharpest peak. The amorphous structure becomes even more irregular and is away from the crystallinity. It can be interpreted that the difference between atomic or ionic diameters of the matrix and the dopant elements cause disruption and incompatibility in the lattice. As a result, the XRD results exhibited that the amorphous peak was expanded and the irregularity increased with the increasing Sm and Tb dopants.

X-ray photoelectron spectroscopic (XPS) evaluation was performed in order to find out oxidation states of elements. All XPS results related to the inverse opal PC samples are given in Figure 4.16. It is found that all PC coatings have Si, O and C elements according to the general XPS surveys in Figure 4.16 (a). Sm and Tb dopants are determined by the help of the PC-S200 and PC-T200 samples (Figure 4.16 (f) and (g)) containing highest amounts of concerned dopants. The small carbon peak that can be seen in Figure 4.16 (a) is related to the carbon, can be the atmospheric carbon or residue, which not burned off entirely after the calcination step (Radnik et al., 2003). This carbon peak, as often done in the literature, used for calibration of the XPS spectra peak positions (Radnik et al., 2003). Si and O elements apart from the carbon are belong to the aimed SiO_2 structure.

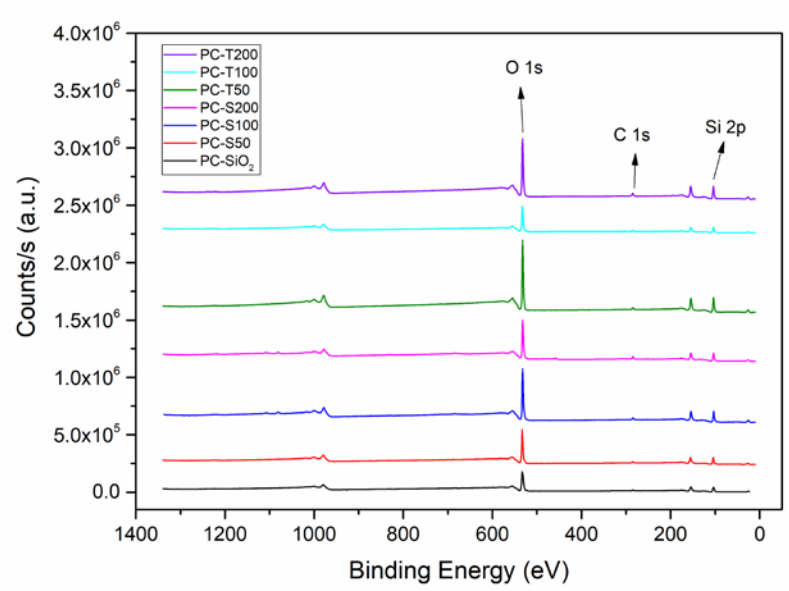

(a)

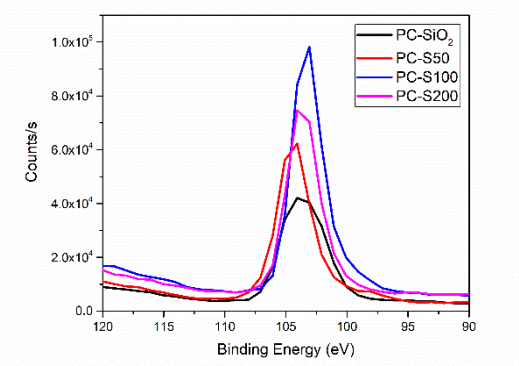

(b)

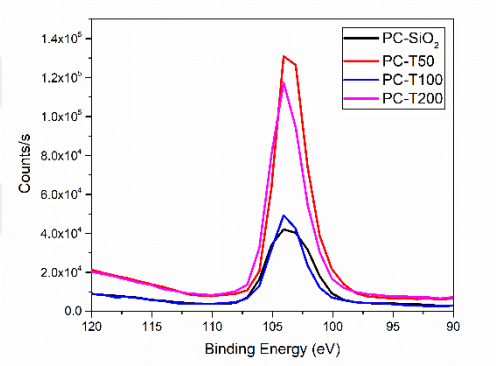

(c)

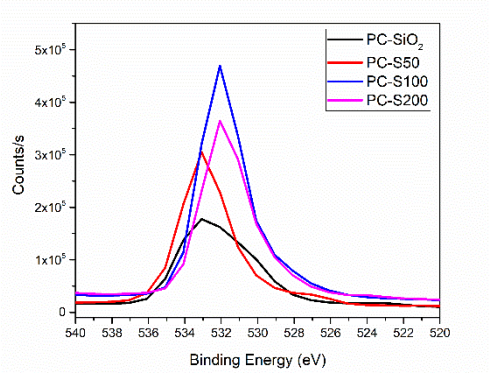

(d)

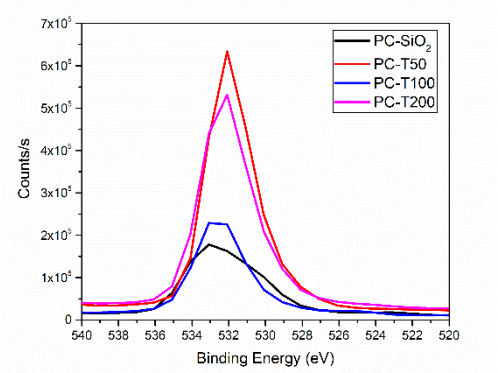

(e)

Figure 4.16 (a) General XPS results of the inverse opal PC coatings. High-resolution XPS scans of Sm or Tb doped PC coatings over (b-c) Si 2p and (d-e) O 1s respectively. XPS scans over (f) Sm 3d and (g) Tb 4d peaks of PC-S200 and PC-T200 PC coating samples, respectively

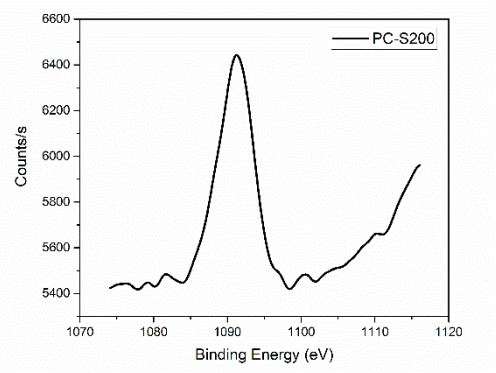

(f)

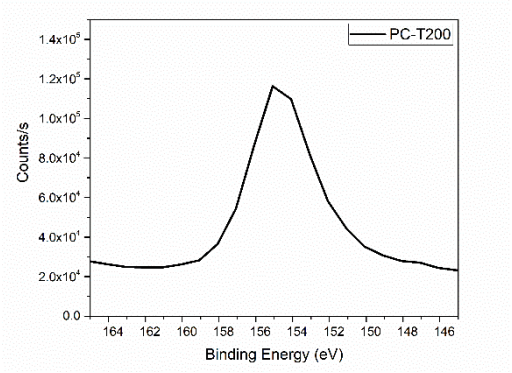

(g)

Figure 4.16 continues

The electron binding energy (BE) values are used for determining the oxidation states of the elements (Radnik et al., 2003). High-resolution XPS graphs of the Sm or Tb doped inverse opal PC coatings on Si 2p and O 1s peaks are given in Figure 4.16 (b-c) and (d-e) respectively. The Si 2p peaks of both Sm and Tb doped inverse opal PC samples are placed around 104 eV according to Figure 4.16 (b-c). According to this BE value, the oxidation state of Si is found as Si^{4+} (Bhupinder Singh, 2016; Sublemontier et al., 2014) and that means the Si is fully oxidized and has the O-Si-O bonds (Y. Jiang et al., 2017). As can be seen from Figure 4.16 (d-e), the binding energy peaks of the Sm and Tb doped inverse opal PC samples are located approximately 532-533 eV. In this way, the existence of O^{2-} ion in the SiO_2 body is approved (Beyza Yildirim, 2019). It can be determined that there are some small modifications at the Si 2p and O 1s peaks after the doping processes. For instance, the Si 2p and O 1s peaks shifted to lower BE values (approximately 1 eV) by Sm doping. However, Tb doping did not affect as much as Sm did. Even Tb doping did not cause any change at the Si 2p peak while it leads shifting to lower BE value (about 1 eV) at the O 1s peak. The XPS peak shift (chemical shift) is based on the change at the oxidation state of the concerned ion (Radnik et al., 2003). More specifically, the observed peak position shift of Si 2p to lower BE values is related to electrons bonding to the oxygen and diffusing silicon into the oxygen vacancies. This phenomenon provides serving as electron traps afterward (Yew et al., 2019). Even, the O 1s shift should be related to the electron transformation into the oxygen vacancies (Papageorgiou et al., 2010; Yew et al., 2019).

In order to determine oxidation states of the Sm and Tb elements detailed XPS spectra of the PC-S200 and PC-T200 samples are presented in Figure 4.16 (f) and (g), respectively. PC samples with the highest dopant contents were taken into account owing to difficulty at detecting at low dopant levels by XPS. It is especially indicated that Sm 3d peak of the PC-S200 sample is located at around 1081 eV (and a small peak about 110 eV) related to the Sm^{3+} ions present in the SiO_2 structure (Kumar et al., 2018; Rajoriya et al., 2019). Similarly, the Tb 4d peak of the PC-T200 sample is placed at BE value of 155 eV related to the Tb^{3+} oxidation state proves the existence of terbium in SiO_2 structure as a dopant ion (Hastir et al., 2016).

4.3.2 Morphological Characterization

Morphologies of the un-doped, Sm or Tb doped coatings in the form of thin-film and inverse opal PC characterized using SEM images presented in Figure 4.17. SEM images of the thin film coatings are located the left side of Figure 4.17 to compare morphologies of the samples in the thin film and PC forms. As can be observed from Figure 4.17, thin film coatings have a morphology with many cracks. Some variations can be observed at these cracks based on the dopant amounts. Some differences in surface morphology of thin films based on dopant type can be seen, but not much change with dopant amounts. The cracks of the Sm doped thin-film coatings have in larger islets (Figure 4.17 (a-e)); while the cracks of the Tb doped thin-film coatings are homogeneously distributed in smaller dimensions (Figure 4.17 (f-i)).

Surface morphologies of un-doped, Sm or Tb doped inverse opal PCs show that all inverse opal PC coatings have honeycomb like structure. The ordered structure also exists in the lower layers as can be observed from the pore cavities. As a result, it is proved that three-dimensional network covers the whole remaining silica-based walls. The pore sizes are about 200 nm, while the wall thicknesses are around 20-30 nm. The three-dimensional wall structure in these dimensions provide excessively increased surface area. Therefore, this inverse opal PC materials have wide range application area for increasing system efficiencies (Yang et al., 2017; Yu et al., 2018).

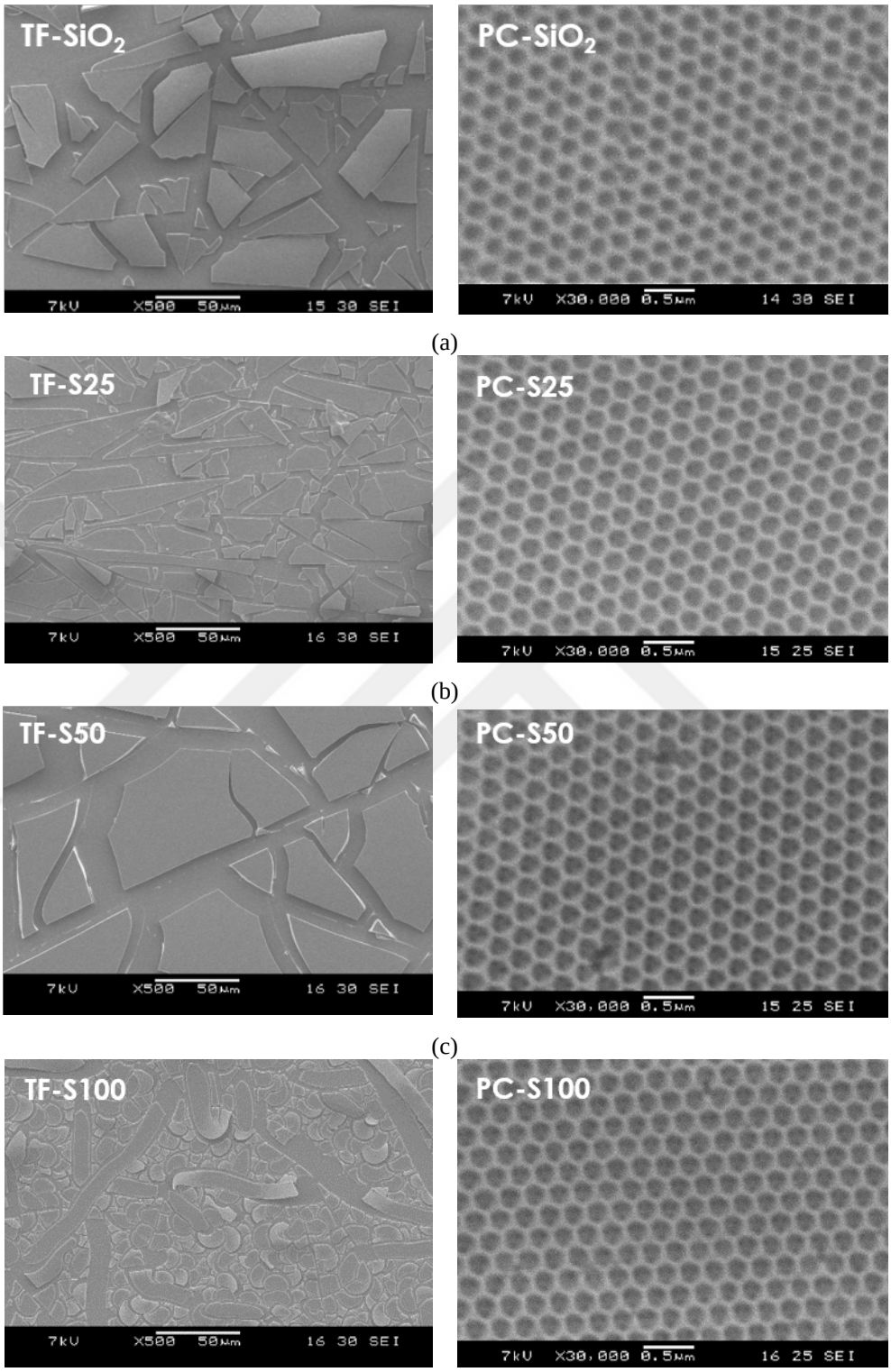

Figure 4.17 SEM images of the (a) un-doped, (b) 0.25%, (c) 0.50 %, (d) 1%, (e) 2% Sm doped; (f) 0.25%, (g) 0.50 %, (h) 1% and (i) 2% Tb doped SiO_2 based samples in the thin film and PC forms

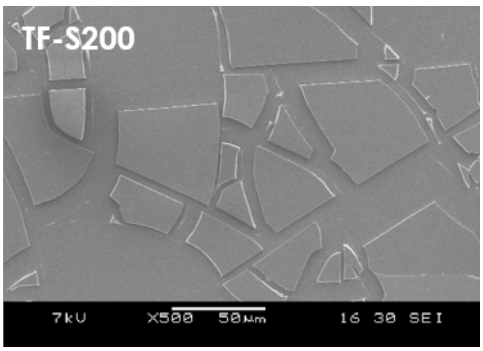

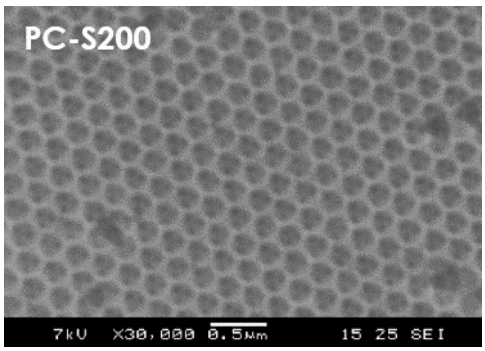

(e)

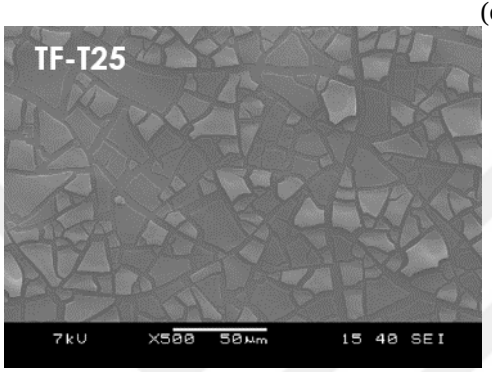

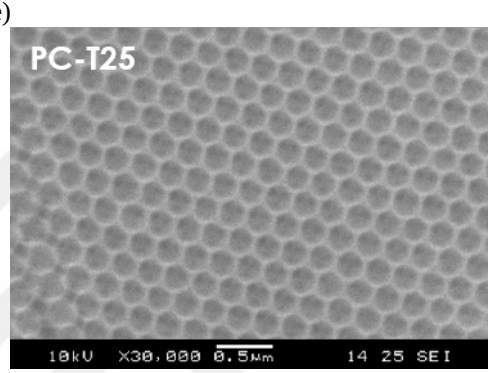

(f)

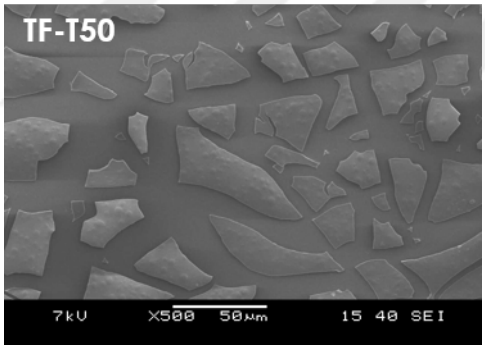

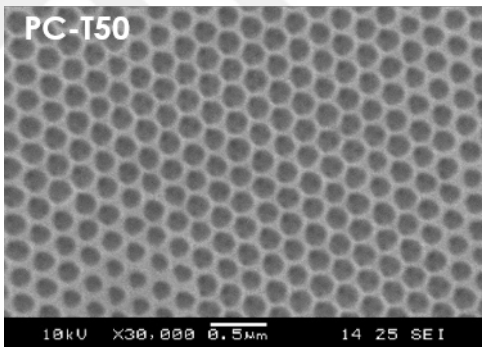

(g)

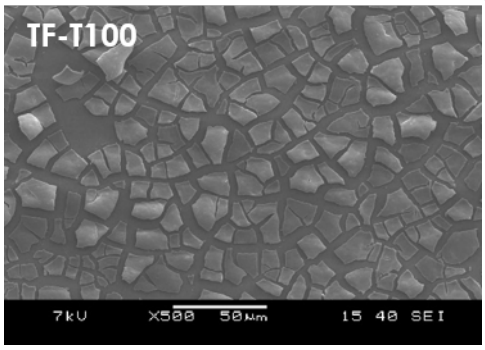

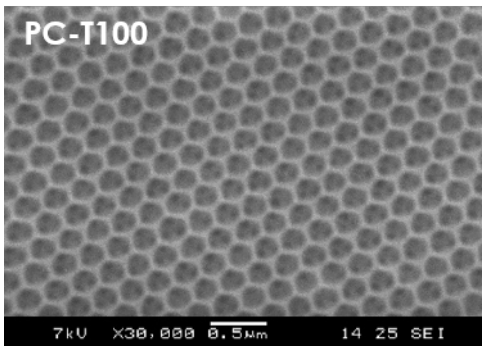

(h)

Figure 4.17 continues

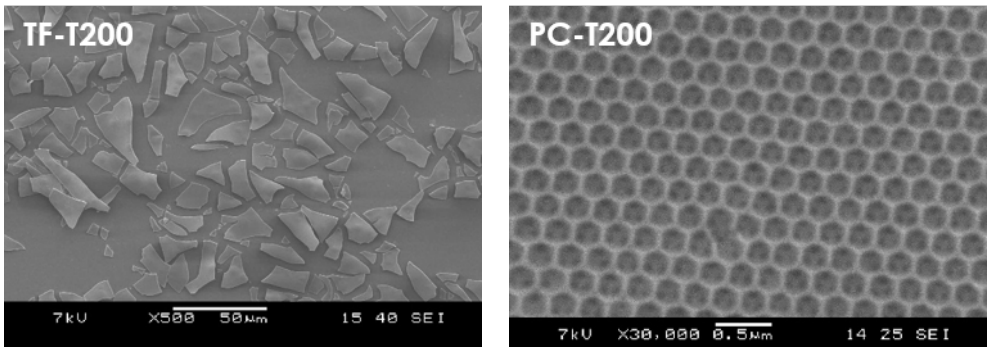

(i)

Figure 4.17 continues

It can be observed that the un-doped inverse opal PC-SiO_2 sample has smaller porosity and wider wall length than Sm or Tb doped PC samples when doping effects are examined. It is possible to say that the regular inverse opal structure is basically preserved but there are regional defects on the surfaces of PC-S50 and PC-S200 samples according to SEM images of the Sm doped coatings in Figure 4.17 (b)-(e). Similarly, there are small defects on the PC-T200 inverse opal PC sample surface (Figure 4.17 (g)) through Tb doped samples (Figure 4.17 (f)-(i)). Nonetheless, it can be concluded that the surface morphology qualities of the inverse opal PC coatings produced by Tb doping are better than that produced by Sm doping.

4.3.3 Optical Characterizations

The UV-Vis reflectance ratios of Sm or Tb doped inverse opal PC and thin films are given in Figure 4.18 (a) and (b) respectively. The reflectance curves of coatings in inverse opal photonic crystal form were represented with continuous curves, while the reflectance spectra of thin films were presented with dashed lines. Optical microscope images were taken in order to interpret the reflectance results more accurately in the visible wavelength range. Optical microscope images taken from thin film and inverse opal PC coating surfaces are given in Figure 4.19. The optical images of thin films are placed to the left side of the Figure 4.19. The UV-Vis reflectance results (Figure 4.18) have been interpreted together with the optical microscope images given in Figure 4.19.

The UV-Vis reflectance spectra of the Sm doped coatings presented in Figure 4.18 together with the un-doped PC-SiO_2. The first thing about the un-doped SiO_2 coating that it has a wide peak in the range of 350 to 450 nm, peaking about 400 nm. It was mentioned before, this characteristic peak which has not 100% reflectance ratio is called pseudo photonic bandgap ($_p$PBG) (Aguirre et al., 2011; Waterhouse & Waterland, 2007). The inverse opal PC-SiO_2 coating has purple and blue colors, due to this pPBG centered in the purple color region and extending to the blue color region as can be observed from Figure 4.19 (a).

It is very clear that $_p$PBG peak effected by Sm and Tb doping according to Figure 4.18. As can be seen from Figure 4.18 (a) increasing Sm dopant amounts caused shifting towards higher wavelength values (redshift) at the $_p$PBG peak. Yet, the reflectance ratios decreased by Sm doping. Moreover, the $_p$PBG peak, which was observed as a wide peak for un-doped, has been turned into a narrower peak by Sm doping. In this way, the observed color appears more vivid and clear with increased resolution by increasing Sm dopants.

When the optical images of the Sm doped PC coatings are examined from Figure 4.19 (b-e), it can be said that the purple color formation on the surface becomes clearer owing to the narrowing reflectance peak in the purple color range. It is hard to speak about any color generation on the surfaces of thin films. Just small green and red colored small regions can be seen at the thin film samples. The lack of concerned blue-violet color on the thin films proves that the blue-violet structural color obtained by the inverse opal PC form.

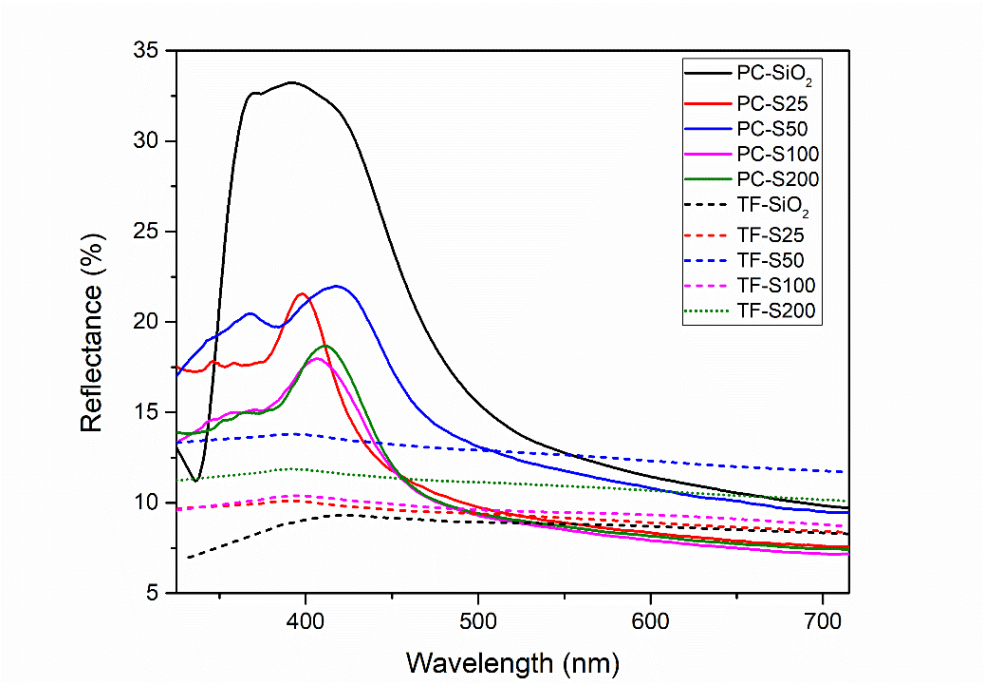

(a)

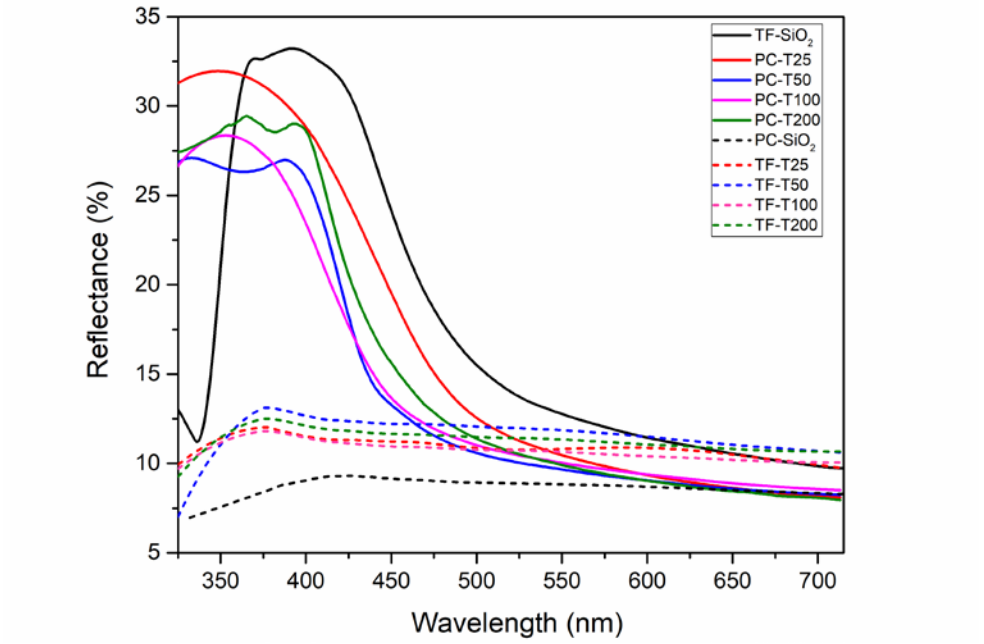

(b)

Figure 4.18 UV-Vis reflectance spectra of the (a) Sm or (b) Tb doped coating samples

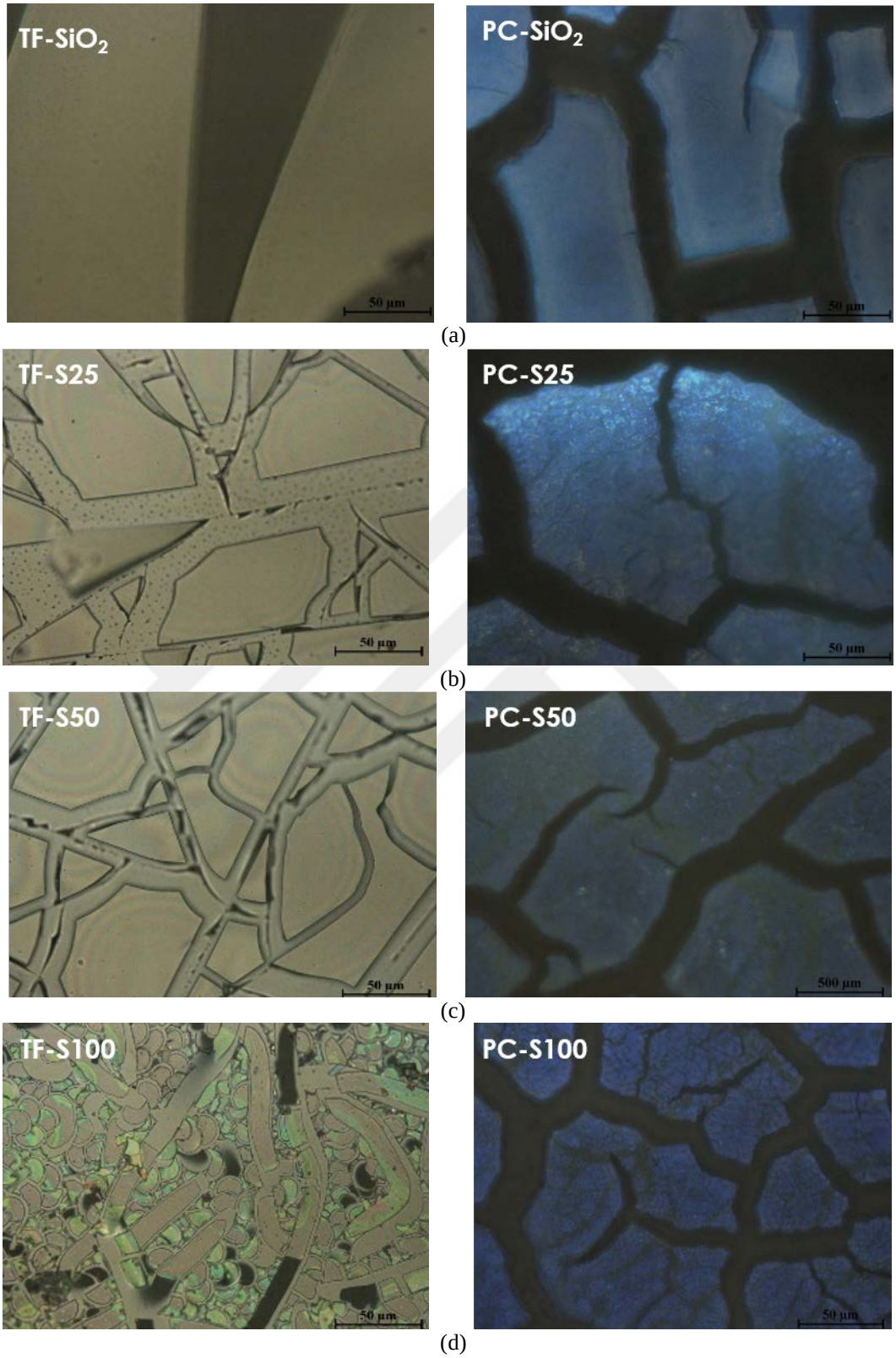

Figure 4.19 Optical images of the (a) un-doped, (b) 0.25%, (c) 0.50 %, (d) 1%, (e) 2% Sm doped; (f) 0.25%, (g) 0.50 %, (h) 1% and (i) 2% Tb doped SiO_2 based coating samples in the thin film and PC forms

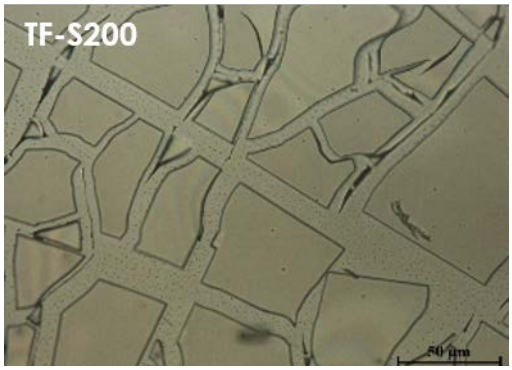

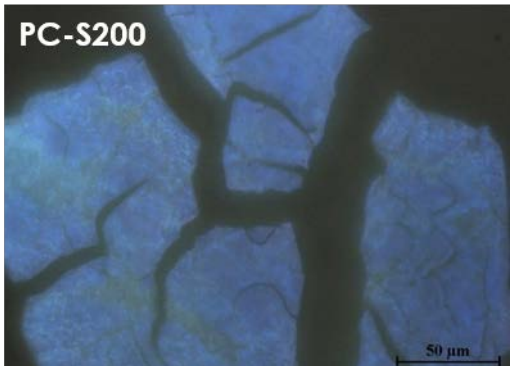

(e)

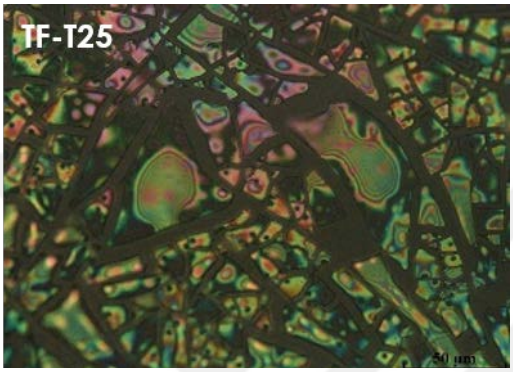

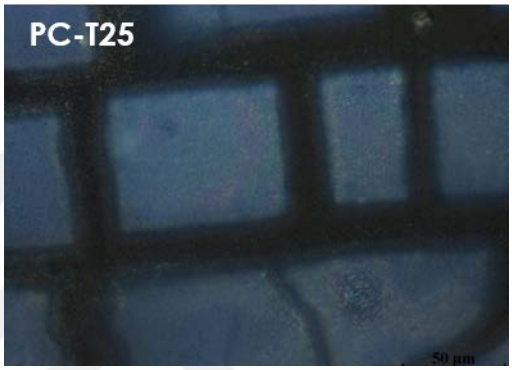

(f)

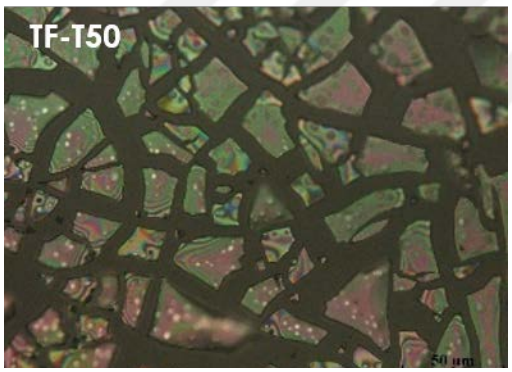

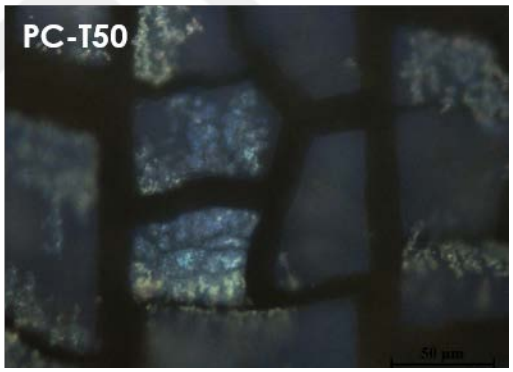

(g)

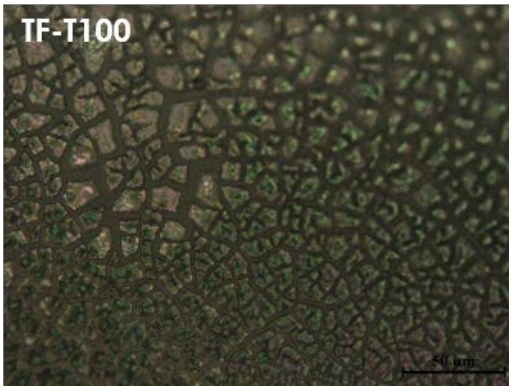

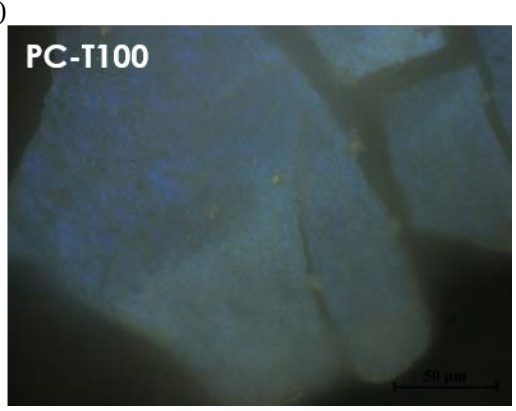

(h)

Figure 4.19 continues

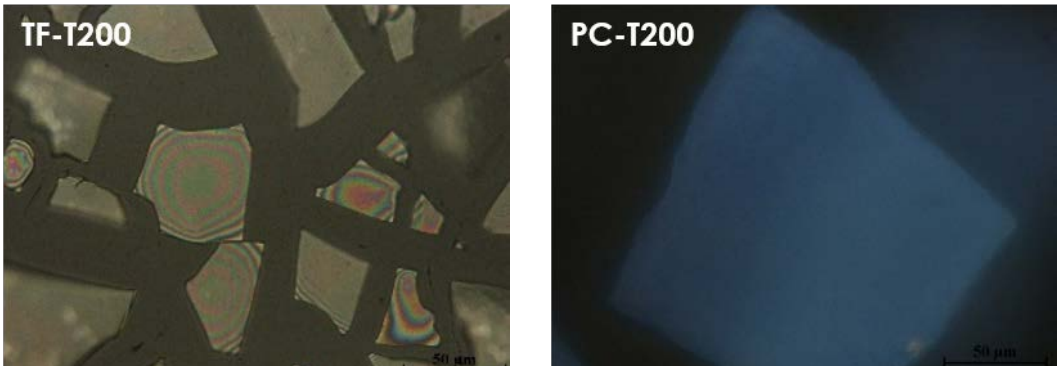

(i)

Figure 4.19 continues

Tb doping affects reflectance curves much differently than Sm doping as can be seen from Figure 4.18. Firstly, reflectance rates decrease slightly by the Tb doping process. The reflectance peaks of the PC coatings shifted to lower wavelengths (blue shift) by Tb doping, unlike Sm doping. It can find out that the Tb doping process widens the reflectance peak. As can be seen from Figure 4.18 (b), the peak-end values are shifted from the blue color region to the violet color region by Tb doping. In this way, the effectiveness of the blue color is reduced. The purple color becomes more dominant on the surfaces of Tb doped inverse opal PC coatings as can be observed from Figure 4.19 (f-i). Color formations such as green-yellow-pink on the Tb doped thin films proves that these changes in reflectance and color could be caused by Tb doping. Another reason for color variations would be the porosity and wall size variations of the inverse opal morphology (Qi et al., 2014).

CHAPTER FIVE
CONCLUSIONS

Opal and inverse opal PC coatings produced successfully by the fast sedimentation and sol-gel infiltration methods. Silica based inverse opal PC coatings doped by rare earth elements such as Ce, Eu, Sm and Tb at the 0.25%, 0.50%, 1% and 2% molar ratio. Obtained results are summarized as follows;

1. PMMA colloids were synthesized successfully by the free radical induced polymerization of methyl methacrylate.

2. PMMA sphere diameters were increased with increasing reaction temperature and initiator amount of the PMMA. PMMA particle sizes were decreased after drying, due to the shrinkage of the polymer body. Results show that PMMA colloids were obtained for all synthesis parameters according to the FTIR results.

3. Fast-sedimentation method was developed to prepare opal PC coatings with regular arrayed PMMA spheres in large areas.

4. When compared to the drying in the furnace condition, drying in an oil bath condition has an appropriate method in order to obtain ordered PMMA opal PCs. The optimum opal PC coatings were obtained in the conditions of 0.70 mM initiator mass, 24 h sedimentation time in the oil bath.

5. It could be seen that the PMMA opal PC coatings show structural colors. Increased sphere size caused redshift while decreased sphere size caused blue shift at the reflectance peaks and they are proved with the optical images. It can be concluded that the peak sharpness increase at the UV-Vis reflectance spectrum is attributed to the clarity of coloration.

6. Synthesis of Ce, Sm, Eu or Tb doped SiO_2 based inverse opal PC coatings were carried out successfully by combination of fast sedimentation and sol-gel infiltration methods.

7. All inverse opal PC coatings have amorphous SiO_2 phase according to the XRD results.

8. It has been observed that the irregularity of the atoms, i.e. the unregulated level, increases and the amorphous peak expands by doping the rare earth elements.

9. All inverse opal PC coatings honeycomb-like morphology. The ordered porous structure surrounds the completely 3-D structure according to the SEM images.

10. It can be said that best inverse opal morphologies are obtained at Tb doped inverse opal PC coatings.

11. Some cracks are observed on the thin film surfaces. It can be said that there is a correlation between thin-film and inverse opal PC surface morphologies.

12. SiO_2 based inverse opal PC coatings have blue and purple colors, as $_P$PBG located in the purple color region and prolonged to the blue color region. The absence of blue-violet color on the thin films proves the blue-violet structural colorization with the PC form.

13. Structural colors of the inverse opal PC coatings can be adjusted by rare earth dopants.

14. It is concluded that, the $_{p}$PBG was red shifted by Ce and Sm doping while blue shifted by Eu and Tb doping. Therefore, Ce or Sm doping makes an inverse opal PC coating bluer while Eu or Tb doping makes more purple.

15. Moreover, Ce and Sm doping made the observed color more vivid and clear by turning $_{p}$PBG to the narrower peak.

PMMA and silica based opal and inverse opal PC coatings are obtained with structural colors, respectively. It is showed that obtained structural colors of the opal PC could be modified by colloid sizes while structural colors of the inverse opal PC could be modified by rare earth dopants. In order to attract more attention, some absorber materials such as graphite can be inserted into the body. Thus, it is believed that the use of photonic crystals with structural color can be applied to daily life. Structurally colored industrial products can be developed by applying photonic crystal technology to paints and textile materials. In addition, studies on the photoluminescence applications of these obtained PC materials have been planning.

REFERENCES

Aguirre, C. I., Reguera, E., & Stein, A. (2010). Tunable colors in opals and inverse opal photonic crystals. *Advanced Functional Materials, 20*(16), 2565-2578.

Aguirre, C. I., Reguera, E., & Stein, A. (2011). Tunable colors in opals and inverse opal photonic crystals. *Advanced Functional Materials, 21*(2), 210-210.

Alexeev, V. L., Das, S., Finegold, D. N., & Asher, S. A. (2004). Photonic crystal glucose-sensing material for noninvasive monitoring of glucose in tear fluid. *Clinical Chemistry, 50*(12), 2353-2360.

Almeida, R. M., & Portal, S. (2003). Photonic band gap structures by sol-gel processing. *Current Opinion in Solid State & Materials Science, 7*(2), 151-157.

Armstrong, E., & O'Dwyer, C. (2015). Artificial opal photonic crystals and inverse opal structures-fundamentals and applications from optics to energy storage. *Journal of Materials Chemistry C, 3*(24), 6109-6143.

Arsenault, A. C., Puzzo, D. P., Manners, I., & Ozin, G. A. (2007). Photonic crystal full-colour displays. *Nature Photonics, 1*(8), 468-472.

Aryal, D. P. (2007). *Theoriy and modelling of functional photonic opals.* PhD Thesis, University of Surrey, United Kingdom.

Astratov, V. N., Bogomolov, V. N., Kaplyanskii, A. A., Prokofiev, A. V., Samoilovich, L. A., Samoilovich, S. M., & Vlasov, Y. A. (1995). Optical spectroscopy of opal matrices with cds embedded in its pores: quantum confinement and photonic band gap effects. *Nuovo Cimento Della Societa Italiana Di Fisica D-Condensed Matter Atomic Molecular and Chemical Physics Fluids Plasmas Biophysics*, *17*(11-12), 1349-1354.

Bhosale, A. K., Tarwal, N. L., Shinde, P. S., Kadam, P. M., Patil, R. S., Barman, S. R., & Patil, P. S. (2009). Effective utilization of spray pyrolyzed CeO_2 as optically passive counter electrode for enhancing optical modulation of WO_3. *Solid State Ionics, 180*(23-25), 1324-1331.

Birlik, I. (2011). *Synthesis of superconducting films and improvement of their flux pinning properties with $BaZrO_3$ nanoparticles using chemical solution deposition method.* PhD Thesis, Dokuz Eylul University, İzmir.

Blanco, A., Chomski, E., Grabtchak, S., Ibisate, M., John, S., Leonard, S. W., van Driel, H. M. (2000). Large-scale synthesis of a silicon photonic crystal with a complete three-dimensional bandgap near 1.5 micrometres. *Nature, 405*(6785), 437-440.

Blanco, A., Miguez, H., Meseguer, F., Lopez, C., Lopez-Tejeira, F., & Sanchez-Dehesa, J. (2001). Photonic band gap properties of CdS-in-opal systems. *Applied Physics Letters, 78*(21), 3181-3183.

Braun, P. V., & Wiltzius, P. (1999). Microporous materials - electrochemically grown photonic crystals. *Nature, 402*(6762), 603-604.

Busch, K., & John, S. (1998). Photonic band gap formation in certain self-organizing systems. *Physical Review E, 58*(3), 3896-3908.

Cademartiri, L., Sutti, A., Calestani, G., Dionigi, C., Nozar, P., & Mighori, A. (2003). Flux-assisted self-assembly of monodisperse colloids. *Langmuir, 19*(19), 7944-7947.

Calderon-Olvera, R. M., Albanes-Ojeda, E. A., Garcia-Hipolito, M., Hernandez-Alcantara, J. M., Alvarez-Perez, M. A., Falcony, C., & Alvarez-Fregoso, O. (2018). Characterization of luminescent $SrAl_2O_4$ films doped with terbium and europium

ions deposited by ultrasonic spray pyrolysis technique. *Ceramics International, 44*(7), 7917-7925.

Cassagneau, T., & Caruso, F. (2002). Semiconducting polymer inverse opals prepared by electropolymerization. *Advanced Materials, 14*(1), 34-38.

Chai, Z. Z., Yang, Z. W., Qiu, J. B., Zhu, J. L., & Song, Z. G. (2018). Embedding Ag or Au nanoparticles within the nano-sized wall of $YbPO_4:Er^{3+}$ inverse opals and resulting enhanced upconversion luminescence. *Ceramics International*, *44*(12), 13757-13764.

Chelnokov, A., Wang, K., Rowson, S., Garoche, P., & Lourtioz, J. M. (2000). Near-infrared Yablonovite-like photonic crystals by focused-ion-beam etching of macroporous silicon. *Applied Physics Letters, 77*(19), 2943-2945.

Chen, J. I. L., von Freymann, G., Choi, S. Y., Kitaev, V., & Ozin, G. A. (2008). Slow photons in the fast lane in chemistry. *Journal of Materials Chemistry, 18*(4), 369-373.

Cherdhirankorn, T., Retsch, M., Jonas, U., Butt, H. J., & Koynov, K. (2010). Tracer diffusion in silica inverse opals. *Langmuir, 26*(12), 10141-10146.

Chung, Y. W., Leu, I. C., Lee, J. H., & Hon, M. H. (2005). Fabrication and characterization of photonic crystals from colloidal processes. *Journal of Crystal Growth, 275*(1-2), E2389-E2394.

Contu, P. (2011). *Band structure in photonic crystals.* PhD Thesis, Universita degli Studi di Cagliari, Cagliari.

Córcoles, J. C. (2010). *Design and modelling of photonic crystals with anisotropic components.* Doctoral dissertation, Universitat Rovira, Tarragona.

Cortalezzi, M. M., Colvin, V., & Wiesner, M. R. (2005). Controlling submicron-particle template morphology: effect of solvent chemistry. *Journal of Colloid and Interface Science, 283*(2), 366-372.

Couturier, J.-P. (2016). *New inverse opal hydrogels as platform for detecting macromolecules.* PhD Thesis, Universität Potsdam, Potsdam.

Dalmis, R., Birlik, I., Azem, N. F. A., & Çelik, E. (2019a). Modification of the sedimentation method for PMMA photonic crystal coatings. *Colloids and Surfaces A: Physicochemical and Engineering Aspects, 577*, 194-201.

Dalmis, R., Azem F. A., Birlik, Isil, Çelik E. (2019b). SiO_2/TiO_2 one-dimensional photonic crystals doped with Sm and Ce rare-earth elements for enhanced structural colors. *Applied Surface Science, 475*, 94-101.

Dalmis, R., Keskin, O. Y., Azem, N. F. A., & Birlik, I. (2019). A new one-dimensional photonic crystal combination of TiO_2/CuO for structural color applications. *Ceramics International, 45*(17), 21333-21340.

Dalmis, R., Birlik, I., Azem, N. F. A., & Celik, E. (2020). Structurally colored silica photonic crystal coatings modified by ce or eu rare-earth dopants. *Colloids and Surfaces A: Physicochemical and Engineering Aspects*, 125138.

Deleuze, C., Sarrat, B., Ehrenfeld, F., Perquis, S., Derail, C., & Billon, L. (2011). Photonic properties of hybrid colloidal crystals fabricated by a rapid dip-coating process. *Physical Chemistry Chemical Physics, 13*(22), 10681-10689.

Denny, N. R., Han, S. E., Norris, D. J., & Stein, A. (2007). Effects of thermal processes on the structure of monolithic tungsten and tungsten alloy photonic crystals. *Chemistry of Materials, 19*(18), 4563-4569.

Dimitrov, A. S., & Nagayama, K. (1996). Continuous convective assembling of fine particles into two-dimensional arrays on solid surfaces. *Langmuir, 12*(5), 1303-1311.

Ding, T., Long, Y., Zhong, K., Song, K., Yang, G., & Tung, C. H. (2014). Modifying the symmetry of colloidal photonic crystals: a way towards complete photonic bandgap. *Journal of Materials Chemistry C, 2*(21), 4100-4111.

Dinsmore, A. D., Hsu, M. F., Nikolaides, M. G., Marquez, M., Bausch, A. R., & Weitz, D. A. (2002). Colloidosomes: selectively permeable capsules composed of colloidal particles. *Science, 298*(5595), 1006-1009.

Doherty, C. M., Caruso, R. A., Smarsly, B. M., & Drummond, C. J. (2009). Colloidal crystal templating to produce hierarchically porous $LiFePO_4$ electrode materials for high power lithium ion batteries. *Chemistry of Materials, 21*(13), 2895-2903.

Dommelen, R. v., Fanzio, P., & Sasso, L. (2018). Surface self-assembly of colloidal crystals formicro- and nano-patterning. *Advances in Colloid and Interface Science, 251*, 97–114.

Ebeoglugil, M. F. (2011). *Processing, characterization and development of rare earth doped lead magnesium niobate ferroelectric ceramic capacitors by sol-gel technique.* PhD Thesis, Dokuz Eylul University, İzmir.

Egen, M., & Zentel, R. (2004). Surfactant-free emulsion polymerization of various methacrylates: towards monodisperse colloids for polymer opals. *Macromolecular Chemistry and Physics, 205*(11), 1479-1488.

Erol, M. (2013). *Production and industrial applications of heat releasing electronic nanocomposite material for heating systems.* PhD Thesis, Dokuz Eylul University, İzmir.

Espinha, A. (2015). *Fabrication of photonic media for controlling emission and transport of light.* PhD Thesis, Instituto de Ciencia de Materiales de Madrid, Madrid.

Fernandez, P. D. G. (2008). *From photonic crystals to photonic glasses through disorder.* PhD Thesis, Universidad Autonoma de Madrid, Madrid.

Fewster, P. F. (2016). The basics of crystallography and diffraction, International Union of Crystallography Diffraction, 4th edition. *Crystallography Reviews, 22*(2), 146-147.

Fortes, L. M., Goncalves, M. C., & Almeida, R. M. (2011). Flexible photonic crystals for strain sensing. *Optical Materials, 33*(3), 408-412.

Garcia, M. L. (2011). *Self assembled photonic-plasmonic crystals for light control at the nanoscale.* PhD Thesis, University of Santiago de Compostela, A Coruña.

Gates, B., Yin, Y. D., & Xia, Y. N. (1999). Fabrication and characterization of porous membranes with highly ordered three-dimensional periodic structures. *Chemistry of Materials, 11*(10), 2827-2836.

Ge, J. P., & Yin, Y. D. (2011). Responsive photonic crystals. *Angewandte Chemie-International Edition, 50*(7), 1492-1522.

Gmachowski, L. (2019). Biomolecule displacement by brownian step. *Colloids and Surfaces a-Physicochemical and Engineering Aspects, 568*, 99-104.

Gu, Z. Z., Yu, Y. H., Zhang, H., Chen, H., Lu, Z., Fujishima, A., & Sato, O. (2005). Self-assembly of monodisperse spheres on substrates with different wettability. *Applied Physics a-Materials Science & Processing, 81*(1), 47-49.

Gugliotti, M., Baptista, M. S., & Politi, M. J. (2004). Surface tension gradients induced by temperature: the thermal Marangoni effect. *Journal of Chemical Education, 81*(6), 824-826.

Guldin, S., Huttner, S., Kolle, M., Welland, M. E., Muller-Buschbaum, P., Friend, R. H., Tetreault, N. (2010). Dye-sensitized solar cell based on a three-dimensional photonic crystal. *Nano Letters, 10*(7), 2303-2309.

Hall, D. B., Underhill, P., & Torkelson, J. M. (1998). Spin coating of thin and ultrathin polymer films. *Polymer Engineering and Science, 38*(12), 2039-2045.

Hartlen, K. D., Athanasopoulos, A. P. T., & Kitaev, V. (2008). Facile preparation of highly monodisperse small silica spheres (15 to > 200 nm) suitable for colloidal templating and formation of ordered arrays. *Langmuir, 24*(5), 1714-1720.

Hastir, A., Kohli, N., & Singh, R. C. (2016). Temperature dependent selective and sensitive terbium doped ZnO nanostructures. *Sensors and Actuators B-Chemical, 231*, 110-119.

Hench, L. L., & West, J. K. (1990). The sol-gel process. *Chemical Reviews, 90*(1), 33-72.

Hernández, S., Gionco, C., Husak, T., Castellino, M., Muñoz-Tabares, J. A., Tolod, K. R., ... & Russo, N. (2018). Insights into the sunlight-driven water oxidation by Ce and Er-doped ZrO_2. *Frontiers in Chemistry, 6*, 368.

Hong, L., Anthony, S. M., & Granick, S. (2006). Rotation in suspension of a rod-shaped colloid. *Langmuir, 22*(17), 7128-7131.

Horsch, M. A., Zhang, Z., & Glotzer, S. C. (2006). Self-assembly of laterally-tethered nanorods. *Nano Letters, 6*(11), 2406-2413.

Hosein, I. D., & Liddell, C. M. (2007). Convectively assembled nonspherical mushroom cap-based colloidal crystals. *Langmuir, 23*(17), 8810-8814.

Hou, J., Li, M. Z., & Song, Y. L. (2018). Recent advances in colloidal photonic crystal sensors: materials, structures and analysis methods. *Nano Today, 22*, 132-144.

Hu, C. X., & Liu, P. (2013). Preparation and microwave dielectric properties of SiO_2 ceramics by aqueous sol-gel technique. *Journal of Alloys and Compounds, 559*, 129-133.

Jiang, P., Bertone, J. F., Hwang, K. S., & Colvin, V. L. (1999). Single-crystal colloidal multilayers of controlled thickness. *Chemistry of Materials, 11*(8), 2132-2140.

Jiang, Y., Jin, Z., Chen, C., Duan, W. B., Liu, B., Chen, X. D., Guo, J. P. (2017). Cerium-doped mesoporous-assembled SiO_2/P25 nanocomposites with innovative visible-light sensitivity for the photocatalytic degradation of organic dyes. *Rsc Advances, 7*(21), 12856-12870.

Jin, L., Huang, X. P., Zeng, G. B., Wu, H., & Morbidelli, M. (2016). Conductive framework of inverse opal structure for sulfur cathode in lithium-sulfur batteries. *Scientific Reports, 6*, 32800.

Joannopoulos, J. D., Villeneuve, P. R., & Fan, S. H. (1997). Photonic crystals: putting a new twist on light (vol 386, pg 143, 1997). *Nature, 387*(6635), 830-830.

John, S. (1987). Strong localization of photons in certain disordered dielectric superlattices. *Physical Review Letters, 58*(23), 2486-2489.

Johnson, S. A., Ollivier, P. J., & Mallouk, T. E. (1999). Ordered mesoporous polymers of tunable pore size from colloidal silica templates. *Science, 283*(5404), 963-965.

Johnson, S. G., Mekis, A., Fan, S. H., & Joannopoulos, J. D. (2001). Molding the flow of light. *Computing in Science & Engineering, 3*(6), 38-47.

Juárez, B. H., Garcia, P. D., Golmayo, D., Blanco, A., & Lopez, C. (2005). ZnO inverse opals by chemical vapor deposition. *Advanced Materials, 17*(22), 2761-2765.

Khanh, N. N., & Yoon, K. B. (2009). Facile organization of colloidal particles into large, perfect one- and two-dimensional arrays by dry manual assembly on patterned substrates. *Journal of the American Chemical Society, 131*(40), 14228.

Kim, O. H., Cho, Y. H., Kang, S. H., Park, H. Y., Kim, M., Lim, J. W., ... & Sung, Y. E. (2013). Ordered macroporous platinum electrode and enhanced mass transfer in fuel cells using inverse opal structure. *Nature Communications*, *4*(1), 1-9.

Kim, S. U., Lee, S. H., Lee, I. H., Lee, B. Y., Na, J. H., & Lee, S. D. (2018). Generation of intensity-tunable structural color from helical photonic crystals for full color reflective-type display. *Optics Express, 26*(10), 13561-13572.

Kim, T. W. (2011). *The applications for 3D inverse opal microstructures.* MSc Thesis, University of Illinois, Urbana.

King, J. S., Heineman, D., Graugnard, E., & Summers, C. J. (2005). Atomic layer deposition in porous structures: 3D photonic crystals. *Applied Surface Science, 244*(1-4), 511-516.

Kinoshita, S., Yoshioka, S., & Miyazaki, J. (2008). Physics of structural colors. *Reports on Progress in Physics*, *71*(7), 076401.

Korake, P. V., Kadam, A. N., & Garadkar, K. M. (2014). Photocatalytic activity of Eu^{3+}-doped ZnO nanorods synthesized via microwave assisted technique. *Journal of Rare Earths, 32*(4), 306-313.

Koyama, F. (2006). Recent advances of VCSEL photonics. *Journal of Lightwave Technology, 24*(12), 4502-4513.

Kuai, S. L., Hu, X. F., Hache, A., & Truong, V. V. (2004). High-quality colloidal photonic crystals obtained by optimizing growth parameters in a vertical deposition technique. *Journal of Crystal Growth, 267*(1-2), 317-324.

Kumar, D. R., Ranjith, K. S., & Kumar, R. T. R. (2018). Structural, optical, photocurrent and solar driven photocatalytic properties of vertically aligned samarium doped ZnO nanorod arrays. *Optik, 154*, 115-125.

Kurt, H. (2006). *Photonic crystals: analysis, design and biochemical sensing applications.* PhD Thesis, Georgia Institute of Technology, Georgia.

Landon, P. B., & Glosser, R. (2004). Self-assembly of spherical colloidal silica along the [100] direction of the FCC lattice and geometric control of crystallite formation. *Journal of Colloid and Interface Science, 276*(1), 92-96.

Lebrun, D. M. (2014). *Fabrication of inverse opal oxide structures for efficient light harvesting.* PhD Thesis, Uppsala University, Uppsala.

Lee, K. T., Lytle, J. C., Ergang, N. S., Oh, S. M., & Stein, A. (2005). Synthesis and rate performance of monolithic macroporous carbon electrodes for lithium-ion secondary batteries. *Advanced Functional Materials, 15*(4), 547-556.

Leunissen, M. E., Sullivan, M. T., Chaikin, P. M., & van Blaaderen, A. (2008). Concentrating colloids with electric field gradients. I. Particle transport and growth mechanism of hard-sphere-like crystals in an electric bottle. *Journal of Chemical Physics, 128*(16), 164508.

Li, T. C., Kheifets, S., Medellin, D., & Raizen, M. G. (2010). Measurement of the instantaneous velocity of a brownian particle. *Science, 328*(5986), 1673-1675.

Li, Y. C., Zhou, L., Liu, G. J., Chai, L. Q., Fan, Q. G., & Shao, J. Z. (2018). Study on the fabrication of composite photonic crystals with high structural stability by co-sedimentation self-assembly on fabric substrates. *Applied Surface Science, 444*, 145-153.

Li, Z. Y., El-Kady, I., Ho, K. M., Lin, S. Y., & Fleming, J. G. (2003). Photonic band gap effect in layer-by-layer metallic photonic crystals. *Journal of Applied Physics, 93*(1), 38-42.

Liau, L. C. K., & Huang, Y. K. (2008). Process optimization of sedimentation self-assembly of opal photonic crystals under relative humidity-controlled environments. *Expert Systems with Applications, 35*(3), 887-893.

López, C. (2003). Materials aspects of photonic crystals. *Advanced Materials, 15*(20), 1679-1704.

López, J. F. G. (2005). *An optical study of opal based photonic crystals.* PhD Thesis, Universidad Autónoma de Madrid, Madrid.

Ma, C., Jiang, Y. N., Yang, X. D., Wang, C. X., Li, H., Dong, F. X., Lin, Q. (2013). Centrifugation-induced water-tunable photonic colloidal crystals with narrow diffraction bandwidth and highly sensitive detection of SCN-. *Acs Applied Materials & Interfaces, 5*(6), 1990-1996.

Malaquin, L., Kraus, T., Schmid, H., Delamarche, E., & Wolf, H. (2007). Controlled particle placement through convective and capillary assembly. *Langmuir, 23*(23), 11513-11521.

Mayoral, R., Requena, J., Moya, J. S., Lopez, C., Cintas, A., Miguez, H., Blanco, A. (1997). 3D long-range ordering in an SiO_2 submicrometer-sphere sintered superstructure. *Advanced Materials, 9*(3), 257.

Mazur, M., Wojcieszak, D., Kaczmarek, D., Domaradzki, J., Song, S., Gibson, D., Poniedzialek, A. (2016). Functional photocatalytically active and scratch resistant antireflective coating based on TiO_2 and SiO_2. *Applied Surface Science, 380*, 165-171.

Mekki, A. (2005). X-ray photoelectron spectroscopy of CeO_2-Na_2O-SiO_2 glasses. *Journal of Electron Spectroscopy and Related Phenomena, 142*(1), 75-81.

Meng, Y., Tang, B. T., Xiu, J. H., Zheng, X. X., Ma, W., Ju, B. Z., & Zhang, S. F. (2015). Simple fabrication of colloidal crystal structural color films with good mechanical stability and high hydrophobicity. *Dyes and Pigments, 123*, 420-426.

Nandiyanto, A. B. D., Ogi, T., Lskandar, F., & Okuyama, K. (2011). Highly ordered porous monolayer generation by dual-speed spin-coating with colloidal templates. *Chemical Engineering Journal, 167*(1), 409-415.

Nelson, E. C., Dias, N. L., Bassett, K. P., Dunham, S. N., Verma, V., Miyake, M., Braun, P. V. (2011). Epitaxial growth of three-dimensionally architectured optoelectronic devices. *Nature Materials, 10*(9), 676-681.

Ngo, T. T., Liddell, C. M., Ghebrebrhan, M., & Joannopoulos, J. D. (2006). Tetrastack: colloidal diamond-inspired structure with omnidirectional photonic band gap for low refractive index contrast. *Applied Physics Letters, 88*(24), 241920.

Niu, W. B., Su, L. T., Chen, R., Chen, H., Wang, Y., Palaniappan, A., Tok, A. L. Y. (2014). 3-Dimensional photonic crystal surface enhanced upconversion emission for improved near-infrared photoresponse. *Nanoscale, 6*(2), 817-824.

Norris, D. J., Arlinghaus, E. G., Meng, L. L., Heiny, R., & Scriven, L. E. (2004). Opaline photonic crystals: how does self-assembly work? *Advanced Materials, 16*(16), 1393-1399.

Notomi, M. (2000). Theory of light propagation in strongly modulated photonic crystals: refractionlike behavior in the vicinity of the photonic band gap. *Physical Review B, 62*(16), 10696-10705.

Okubo, T. (2008). Sedimentation and drying dissipative patterns of colloidal crystals of poly(methyl methacrylate) spheres in a glass dish. *Colloid and Polymer Science, 286*(13), 1527-1535.

Palacios-Lidon, E., Blanco, A., Ibisate, M., Meseguer, F., Lopez, C., & Sanchez-Dehesa, J. (2002). Optical study of the full photonic band gap in silicon inverse opals. *Applied Physics Letters, 81*(26), 4925-4927.

Papageorgiou, A. C., Beglitis, N. S., Pang, C. L., Teobaldi, G., Cabailh, G., Chen, Q., Thornton, G. (2010). Electron traps and their effect on the surface chemistry of TiO_2 (110). *Proceedings of the National Academy of Sciences of the United States of America, 107*(6), 2391-2396.

Park, S. H., & Xia, Y. (1998). Fabrication of three-dimensional macroporous membranes with assemblies of microspheres as templates. *Chemistry of materials, 10*(7), 1745-1747.

Phillips, K. R. (2016). *Sol-gel chemistry of inverse opals.* PhD Thesis, Harvard University, Cambridge, Massachusetts.

Phillips, K. R., England, G. T., Sunny, S., Shirman, E., Shirman, T., Vogel, N., & Aizenberg, J. (2016). A colloidoscope of colloid-based porous materials and their uses. *Chemical Society Reviews, 45*(2), 281-322.

Pierre, A. C. (2013). *Introduction to sol-gel processing*. Berlin: Pringer Science & Business Media.

Qi, D. Y., Lu, L. J., Wang, L. Z., & Zhang, J. L. (2014). Improved SERS sensitivity on plasmon-free TiO_2 photonic microarray by enhancing light-matter coupling. *Journal of the American Chemical Society, 136*(28), 9886-9889.

Raccis, R., Nikoubashman, A., Retsch, M., Jonas, U., Koynov, K., Butt, H. J., Fytas, G. (2011). Confined diffusion in periodic porous nanostructures. *Acs Nano, 5*(6), 4607-4616.

Radnik, R., Mohr, C., & Claus, P. (2003). On the origin of binding energy shifts of core levels of supported gold nanoparticles and dependence of pretreatment and material synthesis. *Physical Chemistry Chemical Physics, 5*(1), 172-177.

Rahman, M. G. A. (2017). *1D Photonic crystal nanocavities for optical sensing.* PhD Thesis, University of Glasgow, Glasgow.

Rajendran, S., & Uma, T. (2000a). Conductivity studies on PVC/PMMA polymer blend electrolyte. *Materials Letters, 44*(3-4), 242-247.

Rajendran, S., & Uma, T. (2000b). Lithium ion conduction in PVC-$LiBF_4$ electrolytes gelled with PMMA. *Journal of Power Sources, 88*(2), 282-285.

Rajoriya, S., Bargole, S., George, S., Saharan, V. K., Gogate, P. R., & Pandit, A. B. (2019). Synthesis and characterization of samarium and nitrogen doped TiO_2 photocatalysts for photo-degradation of 4-acetamidophenol in combination with hydrodynamic and acoustic cavitation. *Separation and Purification Technology, 212*, 344-346.

Ramesh, S., Leen, K. H., Kumutha, K., & Arof, A. K. (2007). FTIR studies of PVC/PMMA blend based polymer electrolytes. *Spectrochimica Acta Part a-Molecular and Biomolecular Spectroscopy, 66*(4-5), 1237-1242.

Rayleigh, L. (1887). XVII. On the maintenance of vibrations by forces of double frequency, and on the propagation of waves through a medium endowed with a periodic structure. *The London, Edinburgh, and Dublin Philosophical Magazine and Journal of Science, 24*(147), 145-159.

Reculusa, S., & Ravaine, S. (2003). Synthesis of colloidal crystals of controllable thickness through the Langmuir-Blodgett technique. *Chemistry of Materials, 15*(2), 598-605.

Sanders, J. V. (1985). Structure of opals. *Journal De Physique, 46*(C3), 1-8.

Santamaría, F. G. (2003). *Photonic crystals based on silica microspheres.* PhD Thesis, Universidad Autónoma de Madrid, Madrid.

Sawada, T., Suzuki, Y., Toyotama, A., & Iyi, N. (2001). Quick fabrication of gigantic single-crystalline colloidal crystals for photonic crystal applications. *Japanese Journal of Applied Physics Part 2-Letters, 40*(11b), L1226-L1228.

Schroden, R. C., Al-Daous, M., Blanford, C. F., & Stein, A. (2002). Optical properties of inverse opal photonic crystals. *Chemistry of Materials, 14*(8), 3305-3315.

Schwartz, R. W., Schneller, T., & Waser, R. (2004). Chemical solution deposition of electronic oxide films. *Comptes Rendus Chimie, 7*(5), 433-461.

Shereda, L. T., Larson, R. G., & Solomon, M. J. (2008). Local stress control of spatiotemporal ordering of colloidal crystals in complex flows. *Physical Review Letters, 101*(3), 038301.

Singh, B., Diwan, A., Jain, V., Herrera-Gomez, A., Terry, J., Linford, M. R.. (2016). Uniqueness plots: a simple graphical tool for identifying poor peakfits in X-ray photoelectron spectroscop. *Applied Surface Science, 11*(15), 1261-1265.

Skorodumova, O. B., Semchenko, G. D., Goncharenko, Y. N., & Tolstoi, V. S. (2001). Crystallization of SiO_2 from ethylsilicate-based gels. *Glass and Ceramics, 58*(1-2), 31-33.

Staude, I., Thiel, M., Essig, S., Wolff, C., Busch, K., von Freymann, G., & Wegener, M. (2010). Fabrication and characterization of silicon woodpile photonic crystals with a complete bandgap at telecom wavelengths. *Optics Letters, 35*(7), 1094-1096.

Sublemontier, O., Nicolas, C., Aureau, D., Patanen, M., Kintz, H., Liu, X. J., Miron, C. (2014). X-ray photoelectron spectroscopy of isolated nanoparticles. *Journal of Physical Chemistry Letters, 5*(19), 3399-3403.

Subramanian, G., Manoharan, V. N., Thorne, J. D., & Pine, D. J. (1999). Ordered macroporous materials by colloidal assembly: a possible route to photonic bandgap materials. *Advanced Materials, 11*(15), 1261-1265.

Sun, J., Li, Y. Y., Dong, H., Zhan, P., Tang, C. J., Zhu, M. W., & Wang, Z. L. (2008). Fabrication and light-transmission properties of monolayer square symmetric colloidal crystals via controlled convective self-assembly on 1D grooves. *Advanced Materials, 20*(1), 123-128..

Suslik, L., Pudis, D., Goraus, M., Nolte, R., Kovac, J., Durisova, J., Schaaf, P. (2017). Photonic crystal and photonic quasicrystal patterned in PDMS surfaces and their effect on LED radiation properties. *Applied Surface Science, 395*, 220-225.

Tauson, V. I., Abramovich, M. G., & Vinogradov, A. P. (1984). On the significance of the phase size effect for understanding the phenomena of polymorphism and polytypism in mineral crystals. *Acta Crystallographica Section A, 40*, C249-C249.

Teh, L. K., Tan, N. K., Wong, C. C., & Li, S. (2005). Growth imperfections in three-dimensional colloidal self-assembly. *Applied Physics a-Materials Science & Processing, 81*(7), 1399-1404.

Tredgold, R. H. (1991). An introduction to ultrathin organic films from langmuir-blodgett to self-assembly. *Nature, 354*(6349), 498-499.

Tseng, C. M., Lu, Y. Y., Elaasser, M. S., & Vanderhoff, J. W. (1986). Uniform polymer particles by dispersion polymerization in alcohol. *Journal of Polymer Science Part a-Polymer Chemistry, 24*(11), 2995-3007.

Turduev, M. (2015). *Photonic crystals engineering for light manipulation: low symmetry, graded index and parity time symmetry.* PhD Thesis, TOBB University of Economics and Technology, Ankara.

van Kats, C. M., Johnson, P. M., van den Meerakker, J. E. A. M., & van Blaaderen, A. (2004). Synthesis of monodisperse high-aspect-ratio colloidal silicon and silica rods. *Langmuir, 20*(25), 11201-11207.

van Blaaderen, A., Ruel, R., & Wiltzius, P. (1997). Template-directed colloidal crystallization. *Nature, 385*(6614), 321-324.

Velev, O. D., & Lenhoff, A. M. (2000). Colloidal crystals as templates for porous materials. *Current Opinion in Colloid & Interface Science, 5*(1-2), 56-63.

Velez, C. I. A. (2010). *Pigments based on colloidal photonic crystals.* PhD Thesis, Unidad Legaria, México City.

Vermolen, E. C. M., Kuijk, A., Filion, L. C., Hermes, M., Thijssen, J. H. J., Dijkstra, M., & van Blaaderen, A. (2009). Fabrication of large binary colloidal crystals with a NaCl structure. *Proceedings of the National Academy of Sciences of the United States of America, 106*(38), 16063-16067.

Viel, B., Ruhl, T., & Hellmann, G. P. (2007). Reversible deformation of opal elastomers. *Chemistry of Materials, 19*(23), 5673-5679.

Vlasov, Y. A., Bo, X. Z., Sturm, J. C., & Norris, D. J. (2001). On-chip natural assembly of silicon photonic bandgap crystals. *Nature, 414*(6861), 289-293.

Vollath, D., Fischer, F. D., & Holec, D. (2018). Surface energy of nanoparticles - influence of particle size and structure. *Beilstein Journal of Nanotechnology, 9*, 2265-2276.

von Freymann, G., Kitaev, V., Lotschz, B. V., & Ozin, G. A. (2013). Bottom-up assembly of photonic crystals. *Chemical Society Reviews, 42*(7), 2528-2554.

Wang, B., Qi, H. J., Han, H. T., Song, Z. H., Chen, J. Y., & Shao, J. D. (2016). Structural, luminescent properties and chemical state analysis of YAG:Ce nanoparticle-based films. *Optical Materials Express, 6*(1), 155-165.

Wang, D. Y., & Caruso, F. (2001). Fabrication of polyaniline inverse opals via templating ordered colloidal assemblies. *Advanced Materials, 13*(5), 350-353.

Wang, H., & Zhang, K. Q. (2013). Photonic crystal structures with tunable structure color as colorimetric sensors. *Sensors, 13*(4), 4192-4213.

Wang, Y., Cui, H., Zhao, Q., & Du, X. (2019). Chameleon-inspired structural-color actuators. *Matter, 1*, 1-13.

Waterhouse, G. I. N., & Waterland, M. R. (2007). Opal and inverse opal photonic crystals: Fabrication and characterization. *Polyhedron, 26*(2), 356-368.

Weisbuch, C., Benisty, H., Olivier, S., Rattier, M., Smith, C. J. M., & Krauss, T. F. (2000). Advances in photonic crystals. *Physica Status Solidi B-Basic Research, 221*(1), 93-99.

Whitworth, R. W. (1989). Basic solid-state chemistry - West,Ar. *Nature, 338*(6211), 175-176.

Wickham, S., Large, M. C. J., Poladian, L., & Jermiin, L. S. (2006). Exaggeration and suppression of iridescence: the evolution of two-dimensional butterfly structural colours. *Journal of the Royal Society Interface, 3*(6), 99-108.

Wijnhoven, J. E. G. J., & Vos, W. L. (1998). Preparation of photonic crystals made of air spheres in titania. *Science, 281*(5378), 802-804.

Wijnhoven, J. E. G. J., Zevenhuizen, S. J. M., Hendriks, M. A., Vanmaekelbergh, D., Kelly, J. J., & Vos, W. L. (2000). Electrochemical assembly of ordered macropores in gold. *Advanced Materials, 12*(12), 888-890.

Woodcock, L. V. (1997a). Entropy difference between crystal phases - Reply. *Nature, 388*(6639), 236-237.

Woodcock, L. V. (1997b). Entropy difference between the face-centred cubic and hexagonal close-packed crystal structures. *Nature, 385*(6612), 141-143.

Xu, L. (2004). *Fabrication of three-dimensionally ordered nanostructured materials through colloidal crystal templating.* PhD Thesis, University of New Orleans, New Orleans.

Xu, L. B., Tung, L. D., Spinu, L., Zakhidov, A. A., Baughman, R. H., & Wiley, J. B. (2003). Synthesis and magnetic behavior of periodic nickel sphere arrays. *Advanced Materials, 15*(18), 1562-1564.

Yablonovitch, E. (1987). Inhibited spontaneous emission in solid-state physics and electronics. *Physical Review Letters, 58*(20), 2059-2062.

Yablonovitch, E., Gmitter, T. J., & Leung, K. M. (1991). Photonic band-structure - the face-centered-cubic case employing nonspherical atoms. *Physical Review Letters, 67*(17), 2295-2298.

Yablonovitch, E., Gmitter, T. J., Meade, R. D., Rappe, A. M., Brommer, K. D., & Joannopoulos, J. D. (1991). Donor and acceptor modes in photonic band-structure. *Physical Review Letters, 67*(24), 3380-3383.

Yang, H. W., Pan, L., Han, Y. P., Ma, L. H., Li, Y., Xu, H. B., & Zhao, J. P. (2017). A visual water vapor photonic crystal sensor with PVA/SiO_2 opal structure. *Applied Surface Science, 423*, 421-425.

Yang, J. H., Li, X., Lang, J. H., Yang, L. L., Wei, M. B., Gao, M., Cao, J. (2011). Synthesis and optical properties of Eu-doped ZnO nanosheets by hydrothermal method. *Materials Science in Semiconductor Processing, 14*(3-4), 247-252.

Yang, Z. W., Wu, H. J., Liao, J. Y., Li, W. C., Song, Z. G., Yang, Y., Qiu, J. B. (2013). Infrared to visible upconversion luminescence in Er^{3+}/Yb^{3+} co-doped CeO_2 inverse opal. *Materials Science and Engineering B-Advanced Functional Solid-State Materials, 178*(15), 977-981.

Yew, R., Karuturi, S. K., Liu, J. Q., Tan, H. H., Wu, Y. C., & Jagadish, C. (2019). Exploiting defects in TiO_2 inverse opal for enhanced photoelectrochemical water splitting. *Optics Express, 27*(2), 761-773.

Yıldırım, S. (2017). *Production and development of implant dosimeters in radiotherapy*. PhD Thesis, Dokuz Eylul University, İzmir.

Yildirim, B., Ertekin, K., Demirci S., Gultekin, S. (2019). Boosting optical performance of polymer embedded phosphors using iodine-free and iodine-decorated sol-gel synthesized α-Fe2O3. *Optical Materials, 9*, 109238.

Yoo, J. H., Kwon, H. J., Paeng, D., Yeo, J., Elhadj, S., & Grigoropoulos, C. P. (2016). Facile fabrication of a superhydrophobic cage by laser direct writing for site-specific colloidal self-assembled photonic crystal. *Nanotechnology, 27*(14), 145604.

Yu, J., Lei, J. Y., Wang, L. Z., Zhang, J. L., & Liu, Y. D. (2018). TiO_2 inverse opal photonic crystals: synthesis, modification, and applications. *Journal of Alloys and Compounds, 769*, 740-757.

Zakhidov, A. A., Baughman, R. H., Iqbal, Z., Cui, C. X., Khayrullin, I., Dantas, S. O., Ralchenko, V. G. (1998). Carbon structures with three-dimensional periodicity at optical wavelengths. *Science, 282*(5390), 897-901.

Zhang, J. L., Xue, L. J., & Han, Y. C. (2005). Fabrication of gradient colloidal topography. *Langmuir*, *21*(13), 5667-5671.

Zhang, X. B., Guo, C. C., Li, Z. Z., Shen, G. L., & Yu, R. Q. (2002). An optical fiber chemical sensor for mercury ions based on a porphyrin dimer. *Analytical Chemistry*, *74*(4), 821-825.

Zhang, Y. Y., Wang, L. L., Ma, X. M., Ren, J. F., Sun, Q. X., Shi, Y. S., Shi, J. S. (2018). Up-conversion nanoparticles sensitized inverse opal photonic crystals enable efficient water purification under NIR irradiation. *Applied Surface Science, 435*, 799-808.

Zhao, W. D., Quan, M. H., Cao, Z. Q., Zhang, Y. X., Wen, J. H., Pan, D., He, W. L. (2018). Visual multi-triggered sensor based on inverse opal hydrogel. *Colloids and Surfaces a-Physicochemical and Engineering Aspects, 554*, 93-99.

Zhao, Y., Zhao, Y., Hu, S., Lv, J., Ying, Y., Gervinskas, G., & Si, G. (2017). Artificial structural color pixels: A review. *Materials*, *10*(8), 944.

Zhu, Y. S., Wang, Y. H., Xu, H. R., Xu, X. M., Huang, J. S., Qiu, D. F., Wang, J. W. (2018). Inhibited concentration quench effect in upconversion luminescence of In_2O_3:Yb^{3+}, Er^{3+} inverse opals. *Journal of Luminescence, 194*, 292-296.